3D Multi-Physics MRI-Based Human Right Ventricle Models for Patients with repaired Tetralogy of Fallot: Cardiac Mechanical Analysis and Surgical Outcome Prediction

A Dissertation

Submitted to the Faculty

of the

WORCESTER POLYTECHNIC INSTITUTE

in Partial Fulfillment of the Requirements of the

Degree of Doctor of Philosophy

by
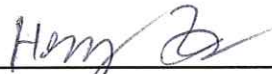
Heng Zuo
May 2017

Approved by

Professor Dalin Tang, Dissertation Advisor, Committee Chair
WPI Department of Mathematical Sciences

Professor Kristen L. Billiar, Committee Member
WPI Department of Biomedical Engineering

Professor Mayer Humi, Committee Member
WPI Department of Mathematical Sciences

Professor Roger Y. Lui, Committee Member
WPI Department of Mathematical Sciences
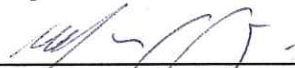
Professor Marcus Sarkis, Committee Member
WPI Department of Mathematical Sciences

Abstract

Introduction. Computational modelling has been used widely in biological and clinical applications, but relatively less in surgical design and optimization. Magnetic resonance image (MRI)-based right ventricle (RV) models were introduced for patients with repaired Tetralogy of Fallot (rTOF) to assess ventricle cardiac function, and to identify morphological and mechanical parameters which can be used to predict and optimize post-surgery cardiac outcome. Tetralogy of Fallot is a common congenital heart defect which includes a ventricular septal defect and severe right ventricular outflow obstruction, account for the majority of cases with late onset RV failure. The current surgical approach for the patients with repaired ToF including pulmonary valve replacement/insertion (PVR) has yielded mixed results. It is of great interest to identify parameters which may be used to predict surgical cardiac function outcome after PVR.

Data, Model, and Methods. Cardiac Magnetic Resonance (CMR) data from 20 healthy volunteers (11 males, mean year : 22.8) and 56 TOF patients (37 males, mean year : 25.3) were provided by Children's Hospital – Boston, Harvard Medical School from our NIH-funded project (R01 HL089269). RV wall thickness (WT), circumferential and longitudinal curvature (C-cur and L-cur), surface area (SA) and surface to volume ratio (SVR) were obtained based on CMR data for morphological analysis. 6 healthy volunteers and 16 TOF patients were chosen to construct 3D computational models for mechanical analysis. The 3D CMR-based RV/LV/Patch combination models included a) isotropic and anisotropic material properties, b) myocardial fiber orientation, c) active contraction with two zero-load geometries, and d) fluid-structure interactions. The models were used to obtain the assessment for RV mechanical conditions, which might be helpful for PVR surgical outcome prediction. All the computational models were built and solved in a commercial finite element software ADINA. Statistical methods including Linear Mixed-effort

Method and Logistical regression were used in the morphological and mechanical analysis to find out potential indicators for predicting PVR outcome from the morphological and mechanical parameters.

Results. In morphological analysis, statistically significant differences were found in RV SA and SVR between better-outcome patient group (BPG) and worse-outcome patient group (WPG). At begin of ejection, mean RV SA of BPG was 13.6% lower than that from WPG (241.1 cm^2 v.s. 279.0 cm^2, p =0.0161). Mean RV SVR of BPG was 13.1% lower than that from WPG (1.26 cm^2/ml v.s. 1.45 cm^2/ml, p =0.0271). Similar results were also found in RV SA and SVR at begin of filling. Furthermore, RV EF change from pre- to post-PVR were found negatively correlated with RV SA and SVR. In mechanical analysis, 22 structure-only models with one zero-load geometry (1G) were constructed to obtain stress/strain distributions. Stress-P_1 from BPG was found to be closer to that from HG, compared to Stress-P_1 of WPG. At the beginning of ejection, mean Stress-P_1 of BPG was only 6.8% higher than that from healthy group (p =0.6889), while average Stress-P_1 of WPG was 84.1% higher than that of healthy group (p =0.0418). Similar results were also found at begin of filling. The results suggested that comparing patient's RV stress values with healthy RV stress values may help identify patients with possible better outcome. The models with two zero-load geometries (2G models) and FSI models were also constructed. Their numerical results indicated that 2G models can provide end-ejection and end-filling results which were not available in 1G models, and FSI models can provide flow velocity, pressure and shear stress information which lacked in structure-only models (1G and 2G models).

Conclusion. *In vivo* image-based 3D patient-specific computational models could lead to considerable potential gain not only in surgical design and outcome prediction, but also in understanding the mechanisms of RV failure for patients with repaired TOF.

Acknowledgements

I would like to express my deepest gratitude to Professor Dalin Tang, my advisor, for his constant help, encouragement, guidance, and thoughtful advice during my study at Worcester Polytechnic Institute. Without his help and support, this dissertation would never have been completed.

I sincerely thank the members of my dissertation committee: Professors Kristen L. Billiar, Marcus Sarkis, Mayer Humi, Roger Y. Lui, and Dalin Tang, for their valuable guidance and support.

My sincere appreciation is extended to my *ex*-advisor, Professor Chun Yang (Beijing Normal University, P.R. China), who is the first professor to introduce me to such an interesting and challenging field, for her professional and personal advice and help. I would like to thank Professor Tang's collaborators who provided data for this research. *In vivo* MRI data of human ventricles were provided by Professor Pedro del Nido and Tal Geva's group from Boston Children's Hospital, Harvard Medical School. Experimental data of heart tissues were provided by Professor Kristen L. Billiar (Worcester Polytechnic Institute). My appreciation also goes to many professors, staff, and my fellow graduate students in the Mathematical Sciences Department for their help and friendship.

Finally, I would like to give a special thank-you to my parents for their constant love, understanding and support.

Table of Contents

List of Figures

List of Tables

1. Problem Statement and Specific Aims

1.1. Problem Statement and Overall Objectives

Right ventricular (RV) dysfunction is a common cause of heart failure in patients with congenital heart defects and often leads to impaired functional capacity and premature death. Patients with repaired Tetralogy of Fallot (TOF), a congenital heart defect which includes a ventricular septal defect and severe right ventricular outflow obstruction, account for the majority of cases with late onset RV failure. Current surgical approaches for repaired TOF patients, which include traditional Pulmonary Valve Replacement (PVR) and PVR with RV remodelling, lead to mixed surgical outcomes with many of the patients seeing little improvement in RV function while others see a significant improvement. Therefore, we are looking for the evaluation and assessment methods that can help predict the surgical outcome based on pre-surgery patient's data.

During the past decades, combining with clinical surgical procedures (del Nido [7]) and non-invasive cardiac magnetic resonance imaging technology (Geva [34]), Tang's team has introduced some novel 3D cardiac magnetic resonance (CMR)-based patient-specific computational models (Tang) aiming to help analyse RV flow and structure, stress/strain distributions, and assess RV cardiac function for optimal surgery design.

The objectives of this dissertation are: a) to investigate the heart geometries of some TOF patients and healthy volunteers provided by doctors aiming to find the indicators for predicting surgery outcome and optimization of surgical design; b) to construct *in vivo* CMR-based patient-specific 3D computational models for human right and left ventricles; c) to analyse the mechanical results obtained from computational models to search indicators for predicting surgery outcome and optimization of surgical design, d) to introduce a new 3D CMR-based patient-specific

computational model by including two zero-load geometries in Tang's previous RV models, aiming to get a better simulation for the movement of ventricles.

1.2. Goals

Goal #1: Perform morphological analysis on RV geometries based on data from Cardiac MRI studies. Cardiac MRI studies have been performed by Dr. Tal Geva in a dedicated MRI suite to acquire patient-specific ventricular geometry for a patient needing RV remodelling and pulmonary valve replacement operations. Based on RV data of 56 TOF patients and 20 healthy volunteers, wall thickness and curvature (circumferential and longitudinal) will be calculated and statistically analyzed to identify possible associations between these morphological parameters and pulmonary valve replacement (PVR) surgery outcome and optimization of surgical designs.

Goal #2: Construct 3D MRI-based computational models to perform mechanical analysis and seek mechanical predictors for surgical outcome. Based on the surgery outcome, 56 TOF patients will be divided into two groups (better-outcome patient group vs. worse-outcome patient group), several patients will be chosen from different groups and their data will be used to construct the computational models. Statistical analysis will be performed on results from computational models to search possible predictors for surgery outcome and optimization of surgical design.

Goal #3: Develop novel 3D MRI-based computational models with two different zero-load geometries for more accurate active contraction modelling. Two different zero-load geometries will be introduced in the new computational models. Based on previous patient-specific CMR-based computational RV/LV/Patch models with two-layer RV/LV structure, anisotropic material properties, fiber orientation, two zero-load geometries will be introduced in the old models to develop some new computational models aiming to include the effects of active contraction.

1.3. Dissertation Outline

This dissertation consists of the following five parts:

Part I. Introduction. In Chapter 1, we describe the problem and state the objectives and specific goals. Chapter 2 give a review of the background of Tetralogy of Fallot (TOF) covering TOF pathology, current TOF repair surgery, mechanism of RV dysfunction in repaired TOF Patients and current surgical procedures for repaired TOF patients with failing RV. A literature review for cardiac computational modelling is also provided in Chapter 2.

Part II. Data Acquisition and 3D Geometry Reconstruction. Chapter 3 briefly introduces what data are wanted and how they are acquired in this project. Chapter 4 presents detailedly 3D geometry reconstruction and mesh generation process performed in ADINA computing environment. The geometry structure consists of points, lines, surfaces and volumes. The key here is to properly divide each physical object into many geometry-fitting volumes so that the finite element (FE) mesh can be generated properly. This step strongly influents the computational element shape and convergence of the model.

Part III. Computational Models, Solution Methods and Statistical Methods. In Chapter 5, we introduce the 3D FSI model for right and left ventricles, which includes the governing equations for solid and flow models, the fluid structure interactions, boundary conditions and initial conditions. Chapter 6 introduces briefly the numerical solution method used in ADINA software. In Chapter 7, the statistical methods used in this project are briefly introduced.

Part IV. Results. In Chapter 8, results of morphological analysis for right ventricle are presented. RV EF is used as the index for PVR outcome. Wall thickness, longitudinal and circumferential curvature, RV volume, surface area and surface-to-volume ratio are computed and analysed. In Chapter 9, results of mechanic analysis for right ventricle are presented. Mechanical stress and

strain are acquired and analysed from computational models with one zero-load geometry (1G models). In Chapter 10, the numerical results of models with two zero-load geometries (2G models) are presented and compared to those from 1G models. In Chapter 11, the numerical results of FSI models are presented and compared to the corresponding structure-only models.

Part V. Discussions and Conclusions. Discussions and conclusions are given in Chapters 12 and 13.

2. Background and Significance

2.1. Tetralogy of Fallot (TOF)

For patients with congenital heart defects, heart failure is commonly caused by Right Ventricular (RV) dysfunction which often leads to impaired functional capacity and premature death.

Tetralogy of Fallot (TOF) is one kind of congenital heart defect including a ventricular septal defect and severe right ventricular outflow obstruction (Figure 2.1). Specifically speaking, TOF is a combination of four cardiac anatomic characteristics including ventricular septal defect, right ventricular outflow tract obstruction, overriding aorta and hypertrophy of the right ventricle. In the United States, the prevalence of TOF is 3.9 per 10,000 live births and accounts for 7-10% of congenital heart diseases. [17]

TOF repair surgery will be implemented on the TOF patients in several months after the birth as the original repair. However, most of patients with repaired TOF are involved in cases with late onset RV failure in two decades after the original repair.
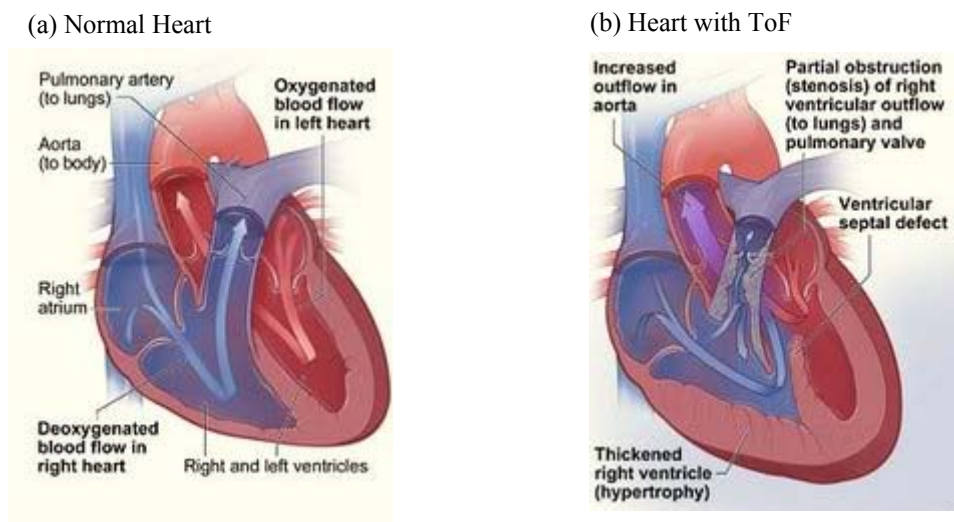
Figure 2.1. Heart structure between healthy people and TOF patients. (a) Normal Heart, (b) Heart with TOF.

2.2. Cardiac MRI Evaluation of PR and RV Mechanics after TOF Repair

Demonstrating and quantifying the effects of chronic pulmonary regurgitation on RV dimensions and function in patients with repaired TOF has been hampered by the lack of reliable tools to measure these variables. This deficiency also contributes to the uncertainty regarding the management of chronic PR and RV volume overload in these patients [7,27-28,32,59,64,71,87]. The development of cardiac magnetic resonance imaging (CMR) techniques to non-invasively quantify ventricular volumes, mass, function, degree of PR, and the extent of scar formation in the RV has been particularly helpful [46,48,93,96,106,124]. In contrast to 2-D echocardiography, angiocardiography, and radionuclide techniques, CMR does not rely on geometrical assumptions, is accurate regardless of the shape or orientation of the chamber, and most investigators now consider it the gold standard imaging modality for assessment of ventricular dimensions and function [55,64,77,91]. Several studies over the past decades have used quantitative CMR methods to investigate various aspects of the anatomic and hemodynamic consequences of TOF repair [1,24,30,33,47-48,82-83,93,95,99,104,124]. These studies have provided important insights into the natural history of repaired TOF and demonstrated its role in this group of patients before and after surgery to treat RV dysfunction [34].

2.3. Mechanism of RV Dysfunction in Repaired TOF Patients

After initial TOF repair, some residual anatomic defects were left in the vast majority of patients, which includes pulmonary regurgitation, and scarred myocardium from the ventriculotomy used to relieve RV outflow obstruction. Indeed, survival for repaired TOF patients diverges significantly from the general population after the first two decades of life (Figure 2.2) which doesn't exist in normal population [84].
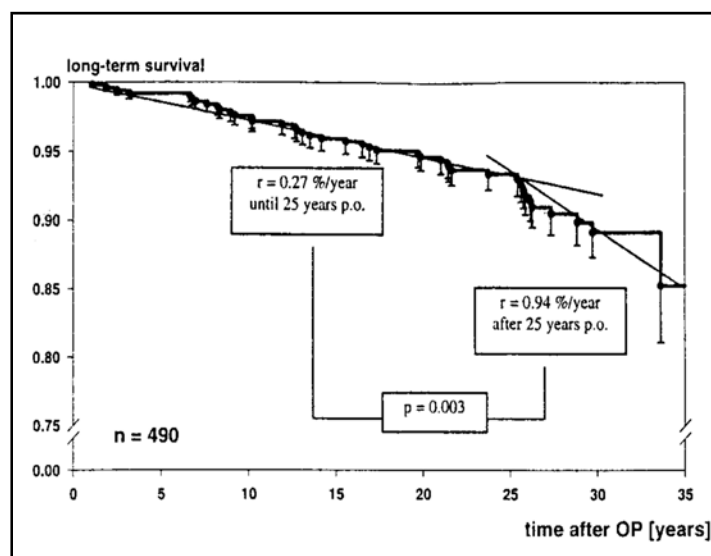
Figure 2.2. Long-term survival after TOF repair (excluding operative mortality [84].

With the improvement of initial TOF repair, survival of surgery for TOF in infancy increased a lot starting from the 80s. However, good results of the initial TOF repair can't guarantee good late results. According to the relevant researches, lots of patients with repaired TOF present severe RV dilation and dysfunction in their third and fourth decade after initial surgery. For these patients, clinical intervention is urgently required.

Three factors contributing to or associated with RV dysfunction are older age at time of original repair, anatomic features and physiologic factors. These conclusions have been identified by most investigators. Specifically speaking, anatomic features impacting RV function include: size of RV outflow patch at initial repair, aneurysm formation at the RV outflow, extent of myocardial scarring from epicardial coronary artery disruption at the time of RV ventriculotomy, and tricuspid valve regurgitation [15, 72]. Some of these anatomic features have been investigated separately and have been implicated in poor right ventricular function. Right ventricular outflow tract akynesia and/or aneurysm formation has been shown to be an independent predictor of poor RV function along with increased RV muscle mass [22]. Most clinical reports evaluating TOF

7

patients presenting with symptoms of RV failure requiring surgical intervention show a relatively high incidence of RV outflow akinesia/dyskinesia (up to 38% of pts. [22]) and significant tricuspid regurgitation (up to 30% of pts. [92]).

2.4. Current Management of Failing RV in TOF Patients

Traditional surgical procedure, namely pulmonary vale insertion (PVR), for patients with repaired TOF aims at eliminating the defects that directly impact on RV volume. In traditional procedures, main efforts are taken to eliminate pulmonary regurgitation by inserting a prosthetic valve and reduce the RV outflow patch (Figure 2.3).

(a) Heart with repaired ToF   (b) Traditional PVR   (c) PVR with RV remodeling
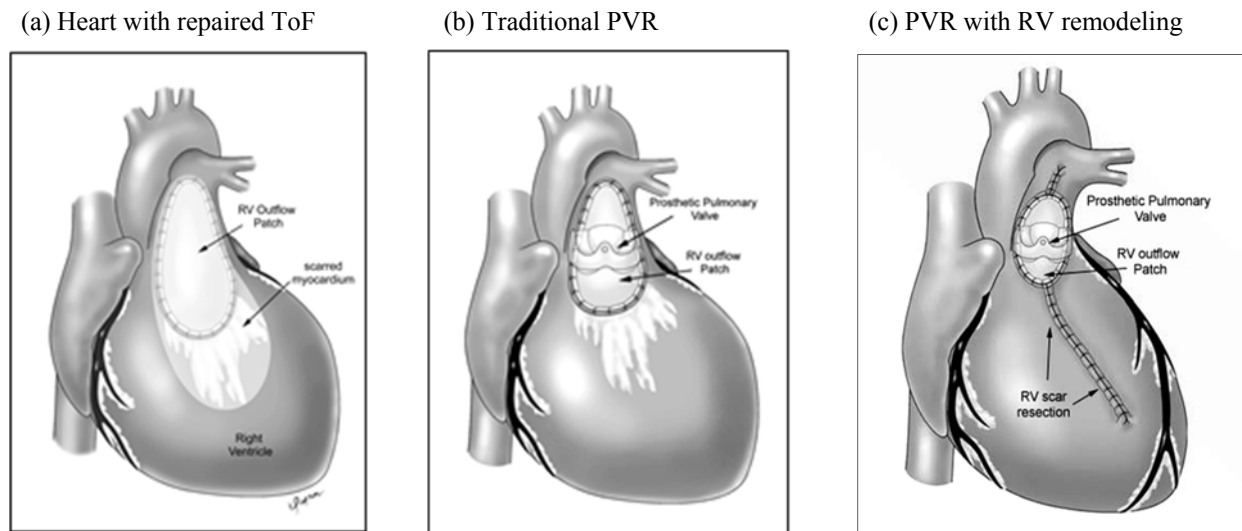
Figure 2.3. Current Surgeries of failing RV in repaired TOF patients: (a) Repaired Tetralogy of Fallot heart with RV outflow patch and scar on anterior RV wall, (b) After pulmonary vale insertion (PVR) and reduction of RV outflow patch, (c) RV after pulmonary valve insertion (PVR), reduction of RV outflow patch and removal of RV scar.

Studies evaluating the results of traditional PVR indicate that in most patients there is a significant decrease in RV end-diastolic volume [124], which is the index, used to assess volume load of the ventricle. However, more recent studies focusing on RV function after surgery have

found mixed results. While some clinical reports indicate that pulmonary valve insertion/replacement (PVR) and RV outflow patch reduction result in a decrease in RV volume and some improvement in RV function, other reports contradict these findings showing that in their study cohort, PVR and RV outflow patch reduction alone do not result in improved RV function after surgery [26]. In these researches, methodology changes with the time, such as MRI begin to be used in the latter studies. Methodology might be the reason for the mixed results in these findings. But the mixed results likely also indicate that there is significant heterogeneity in this patient population. The lack of predictable improvement in ejection fraction after PVR alone is of concern, and suggests that persistent RV dysfunction is a marker of adverse remodeling with scar formation and fibrosis, and that conventional procedures with PVR alone are not enough for many patients.

Scarring of the right ventricle even in areas remote from the RV outflow patch is a frequent finding late after repair of Tetralogy [7]. The reason for the scar formation is unclear. It might be a result of direct injury at the time of original repair while it might also be caused by the adverse effects of chronic pressure and volume overload. By using delayed enhancement CMR Geva et al [7] found that there is often evidence of fibrosis or scar in areas adjacent but not contiguous with the RV outflow patch is in patients late after tetralogy repair. This finding along with the knowledge derived from the extensive literature analyzing LV scarring and aneurysmal remodelling, has led Geva and del Nido [7] to develop a novel surgical technique, named "surgical RV remodelling". In the new procedure, the scarred myocardium from the RV outflow and adjacent anterior wall of the RV will be removed aiming to reduce the RV volume and remove the non- or poorly contracting tissue in the RV (Figure 2.3(c)).

2.5. Review of Cardiac Computational Modeling

Computational modeling and medical imaging technologies have made considerable advances in biological and clinical research in recent years [6,33,37,39-42,53,73-74,76,107-108,111-112]. Computer-assisted procedures become more and more common in the clinical applications, such as clinical decision making process and computer-aided surgery design.

2.5.1. 3D Models of Cardiac Anatomy

Computational reconstruction of cardiac anatomy is the first step in the development process of a 3D cardiac model. Most of old cardiac models only used some simple geometrical shapes to represent the shape of the ventricles roughly. For example, two concentric ellipsoids truncated at the base level are often used to approximate the shape of the LV. Nowadays, this approach is still in use for some researches where the anatomical realism is not crucial for the purpose of the model [57,103]. Later on, anatomical models were used to get a more realistic shape of the heart. In these models, the shape of the heart was generally constructed from histo-anatomical slices or from measurements taken on explanted hearts [81]. The rabbit model from McCulloch A.D. group [120] and the canine model from Hunter P.J. group [103] are the most representative ones for anatomical models, which are highly referenced and reused. With the improvement of medical imaging technology, it becomes possible to build realistic 3D cardiac models from either in-vivo or ex-vivo images. Medical image-based 3D cardiac models have proliferated over the last 20 years because of the advanced and consolidated techniques such as magnetic resonance imaging (MRI) and computed tomography (CT). Patient-specific models of the cardiac anatomy were constructed from the in-vivo images of specific human subjects, usually MRI [3,45,79] or CT [100,128].

2.5.2. Muscular Architecture of the Heart

Cardiac myocytes are elongated cells arranged in a laminar sheet organization to form the ventricular myocardium [2,67]. The direction of the longitudinal axis of cardiac myocytes is known as fiber orientation. Electrical activation pattern of myocardium and mechanical behavior of cardiac tissue are greatly influenced by fiber orientation [18]. Thus fiber orientation should be included in models to perform realistic computational simulations.

Streeter & Bassett described ventricular myocardium as a continuum in which myofiber orientation1 varied smoothly across the ventricular wall [109]. Their findings have been a crucial impact on most cardiac continuum models over the past 50 years [23,57,88,100]. Recently, more advanced technologies, including diffusion tensor imaging (DTI) or micro-CT, have been implemented to find more accurate descriptions of cardiac fiber orientations. DTI is a MRI modality capable of showing the diffusion of water molecules within the biological tissues. Some recent works shows that DTI-derived fiber orientation has a high similarity with Streeter's finding [8,14]. Micro-CT with iodine staining is another image modality recently used to assess the fiber orientation in certain critical regions of atrial tissue by structure tensor method [5]. However, in-vivo cardiac DTI is not able to provide the full patient-specific fiber orientation of the whole heart because of its high sensitivity to motions. For micro-CT, it is also not feasible due to the needed high dose of ionizing radiation. In conclusion, currently there is no in-vivo technique capable of providing the full patient-specific fiber orientation of the whole heart.

2.5.3. Material Properties and Mathematical Models for Myocardium

Passive Properties of Myocardium

Detailed information about the relationship between force and length is needed to characterize the material properties of myocardium. Biaxial tensile testing has been widely used

11

to characterize the material properties of noncontracting myocardial tissue using an approach first described by Demer & Yin [25]. Biaxial testing has been carried out on specimens from different sites in the LV free wall and septum of dog hearts [49,85,105,129]. The biaxial material properties of RV myocardium [102] and collagenous epicardium [49] have also been studied in this way. The myocardial specimens exhibited nonlinear, viscoelastic, anisotropic mechanical properties with greater stiffness in the fiber direction than transverse to it [85].

Generally, incompressible elastic solids are used to model biological soft tissues. In this kind of models, the derivatives of the strain energy function with respect to the Green strain components give the second Piola-Kirchhoff stress tensor [51]. Exponential strain energy functions of the form $W = \frac{1}{2}C(e^Q - 1)$ have been successfully used to model the material properties of passive myocardium [28-29,36,86,118].

Active Contraction of Myocardium

Unlike other soft tissue, there exists active contraction in cardiac muscle. Adding active fiber stress to passive stress is one way to model active contraction. Another way is to introduce the time-dependent material properties in modeling. About the idea of active stress, various active laws have been used in previous researches. The simplest method is to represent active state as a time-varying elastance [40]. The most complex way, such as an empirical "fading memory" model where realistic length and velocity dependence are introduced, is to model the kinetics of calcium binding to troponin-C, tropomyosin kinetics, and cross-bridge kinetics [52].

The existence of active fiber stress changes the material properties of myocardium. Therefore employing a time-dependent material properties in modeling is reasonable to model active contraction. Tang et al. applied this idea in their models and the results of RV volumes reached a high correspondence with the experimental data [113,115,126-127].

2.5.4. 3D Heart Models of Mechanical Function

3D mechanical behavior of the intact heart is an important indicator for the heart function. However, mechanical parameters such as stress cannot be measured under current clinical techniques. Computational models based on established continuum mechanics principles can help us have a better understanding of the mechanics of the normal and unhealthy hearts.

At the beginning of heart simulations, passive models which didn't consider the active contraction were the leading models in this area. Guccione et al. used a cylindrical finite element model incorporating representative transmural variation of fiber orientation to analyze passive LV inflation [38]. In a related study, Guccione et al. constructed an axially symmetric model of the canine LV from a representative base-apex section and incorporated data on myofiber orientations in this profile [41]. Accurate representations of ventricular anatomy have been used with a 3-D orthotropic "pole-zero" material law to model passive filling in the dog heart [76]. In these passive models, the myocardium was considered as the incompressible elastic solids.

With the development of knowledge about material properties of myocardium, a more complicated model, active model, becomes the most active one in heart simulation. In many of current cardiac mechanic models, the active contraction of the ventricles is considered to be arose from the active tension generated by the myocytes. The models of active tension can approximately be grouped into three categories: 1) time-varying elastance models, 2) "Hill" models, 3) fully history-dependent models either based on Huxley's crossbridge theory or on myofilament activation models. In time-varying elastance models, cardiac active tension is essentially dependent on muscle length and time [19,52,110]. In "Hill" models, the active fiber stress is modified by shortening or lengthening according to the force-velocity relation [4,77]. In fully history-dependent models, Huxley's crossbridge theory yields a system of partial differential

equations as functions of time and crossbridge position [54,89,121], whereas myofilament activation model yields a system of (less computationally expensive) ordinary differential equations as functions of time and shortening velocity [61-62,91,94,97-98].

Up to this day, a large number of active cardiac mechanic models have been proposed for different uses.

The first application is to investigate the relationship between electrical and mechanical behaviors in the heart. The clinical experiments found that asynchronous electrical activation can cause abnormalities in perfusion and pump function, this finding implied the influence of altered cardiac activation sequence on the mechanical behaviors. For better understanding he relationship between the pattern of electrical activation in the ventricles and the local sequence of mechanical strain, several electromechanical models were constructed. Usyk and McCulloch used a canine heart model to examine the delay between the onset of electrical activation and the onset of fiber shortening (EM delay, EMD) in sinus rhythm and LV pacing [119]. Their results were indicating the possibility of fiber shortening before electrical depolarization. A 3D EM model of the rabbit ventricles was built by Gurev et al. and used for a thorough analysis of the 3D distribution of EMD in the rabbit ventricles and its dependence on the loading conditions [43]. This study revealed that the loading conditions of the ventricles play an important role in the relationship between electrical and mechanical activation.

Also, electromechanical models of hearts were used in ventricular mechano-electric coupling and arrhythmias. Li et al. used ventricular electromechanical models as a tool to investigate the role of mechano-electric coupling in arrhythmogenesis [69-70]. Panfilov et al. and Keldermann et al. [90] used the EM models of the human left ventricle to investigate the effect of mechano-electric coupling via SAC(stretched-activated channels) on reentrant wave stability. Jie

et al. studied the role of SAC in the spontaneous induction of arrhythmias in the diseased heart with the help of ventricular EM models [55].

Furthermore, electromechanical models showed its powerful use in researches about the role of mechanical parameters in vulnerability to electric shocks. One whole-heart electromechanical model was built and used by Trayanoya et al. to unravel which mechanical deformation may lead to increased vulnerability to electric shocks and elevated defibrillation [117].

Finally, electromechanical models became more popular in the investigation of clinical surgeries. One example is Cardiac Resynchronization Therapy (CRT) which is a valuable therapy for the patients who exhibit dyssynchrony in contraction. Simulations of whole-heart EM behavior have begun to provide comprehensive analysis of the physiological responses that regulate CRT. Niederer et al. used an EM model constructed from in vivo MRI data to conduct a sensitivity study of the efficacy of CRT to various cellular and organ EM parameters in the heart [80].

2.5.5. Fluid-Structure-Interaction (FSI) Models

The Fluid structure interaction models were extensively used to better investigate and analyze the complete operational activities of the heart. The most active computational fluid-dynamics (CFD) approaches to simulate the heart flow might be roughly classified as three types: (1) geometry-prescribed CFD method, (2) fictitious Fluid-Structure Interaction (FSI) method (3) realistic FSI method.

Geometry-prescribed CFD method is the way to simulate the flow on prescribed moving meshes or boundaries constructed mostly from Computerized Tomography (CT) or Magnetic Resonance Imaging/Tomography (MRI/MRT) data. In this way, the structure's feedback on the fluid is not considered thus generally there is no structure model involved. Using Geometry-prescribed CFD approach Taylor et al. investigated the three dimensional LV ejection [116].

Vierendeels et al. developed a two dimensional canine LV model where they adopted Geometry-prescribed CFD method and did not consider the effect of ventricle wall [122]. They used this geometry-prescribed CFD model to analyze the flow patterns and the changes in the intraventricular pressure inside the cavity during diastole stage. Lassila et al. considered patient-specific case in developing a model of LV and carried out a numerical analysis using Geometry-prescribed CFD method [63]. The motion of the LV is reconstructed from a time-sequence of images and imposed as a boundary condition on the motion of the fluid domain.

The fictitious FSI method is a kind of macroscopic approximation approach. The most famous fictitious FSI method is the immersed boundary method which was introduced by McQueen and Peskin [75]. In the immersed boundary method, the heart wall is represented as a network of neutrally buoyant fibers where momentum is exchanged between the fluid and tissue fibers via a special interpolation scheme. The method represents an appealing middle ground between simpler geometry-prescribed CFD method and complex realistic FSI method. It also provides an elegant means of simulating the valve leaflets. Using the immersed boundary technique of Peskin and McQueen, Lemmon & Yoganathan investigated the diastolic functionalities of the LV including the atrium and pulmonary veins under various conditions of ventricle dysfunction and also assessed the flow behavior of the left atrium and ventricle [68]. Cheng et al. used immersed boundary method to simulate the flow pattern and intraventricular pressure changes inside the LV under the filling phase [21].

Realistic FSI method is the most profound and promising method for heart simulation, where the activities of structure and flow are included and the interaction between solid and flow is also considered. In realistic FSI models, the structure is generally modeled by the conventional Finite Element Method (FEM), the fluid is generally modeled by CFD method, and the interaction

16

between structure and fluid is coupled by realistic coupling algorithms. Chahboune *et al*. proposed a FEM based realistic FSI model for two-dimensional simulation of the complete cardiac cycle in a simplified model of the left ventricle [20]. Vierendeels *et al*. built an axisymmetric two-dimensional realistic FSI model with nonlinear thin-shell theory for the filling of a simplified canine ventricle, and produced reasonable pressure distributions and vortex patterns [122-123]. Watanabe *et al*. presented a three-dimensional realistic FSI model taking the propagation of excitation into account [125]. Using this model they simulated the fluid-structure interaction during the human left heart contraction in normal excitement and arrhythmia. A review of the previous researches with particular emphasis on the coupling mechanisms including the contraction, activation and ventricular blood flow inside the heart was reported by Lee et al. [66]

From 2005, Tang *et al.* constructed a series of patient-specific FSI Right and Left ventricular models to evaluate and optimize human pulmonary valve replacement/insertion (PVR) surgical procedure. All the FSI models of Tang's team belong to realistic FSI models. A time-dependent material model was introduced to simulate the active contraction of myocardium. Patient-specific MRI data were used in the construction of anatomical models. In 2007, Tang et al. built a patient-specific right/left ventricle and patch (RV/LV/patch) combination model with FSIs to investigate the effects of the patch used in conventional PVR surgery [126]. Results of modeling showed that patches with material properties better matching RV tissue properties and smaller size lead to better RV function recoveries. In a follow-up study, the patient-specific CMR-based models were used to compare two PVR surgical procedures often used in clinic [112]. Modeling results indicated that PVR with a smaller patch and more aggressive scar removal might lead to improved recovery of RV functions. Recently, Patient-Specific FSI Ventricular models with a contracting band were constructed and used to investigate a new surgical option placing an elastic band in the

right ventricle aim at improving RV cardiac function measured by ejection fraction (EF) [115,127]. Simulation results implied that the band insertion combined with active band has the potential to improve right ventricle ejection fraction.

2.5.6. Mesh Processing

For numerical simulation, heart models should be represented by 3D elements resulting from a meshing process. The most common meshes consist of Finite Element Mesh and grid-based mesh.

FE volumetric meshes based on linear elements, such as tetrahedral, hexahedral or their combination, are usually used for electrophysiology simulations. FE meshes based on a higher order element, like cubic Hermite elements, can provide a smooth representation of the model geometry and thus this kind of FE meshes are generally used to simulate large deformation mechanics [60]. Indeed, models aimed at electromechanical simulations usually include two coupled FEM volumetric meshes: one based on linear elements to solve the electrical component and one based on higher order elements [57] or Hermite interpolation functions [44] for the mechanical problem.

2.6. Significance

With the rapidly increasing number of late survivors of repair of tetralogy of Fallot, surgical management of patients with right ventricular dysfunction has become a major clinical challenge. The wide variability in clinical status, extent of right ventricular dilatation, scarring, and dysfunction at the time of presentation has resulted in disparate surgical results with pulmonary valve insertion alone [17]. The proposed multi-disciplinary approach of integrating innovative computational modeling, surgical procedures and noninvasive CMR techniques has the potential

for improved outcome of RV remodeling surgical procedures associated with pulmonary valve replacement surgery.

With the development of imaging techniques and computer science, it becomes possible to develop the patient-specific 3D computational RV/LV/Patch combination models with fluid-structure interactions to simulate blood flow and stress/strain in the right ventricle. Computational simulations will be used to supplement/replace empirical and often risky clinical experimentation to examine the efficiency and suitability of various reconstructive procedures in diseased hearts so that optimal design can be found.

Combining the non-invasive CMR techniques and finite element method, we plan to develop several kinds of patient-specific 3D computational models for human heart, such as structure-only models, fluid-structure-interaction models, isotropic models, anisotropic models, passive models, active models, etc. Pre-shrinkage procedures will be introduced to get the zero-load geometries. In the real movement of human heart, the no-load length of myocardium is different in the diastole and systole period, so it means that two zero-load geometries should be considered in the simulations. In this dissertation, we will develop a novel model with two different zero-load geometries hoping the new model can provide a more authentic simulation.

3. Data Acquisition and Biaxial Testing of RV Material Properties

The computational models were constructed using CMR data from Harvard Medical School. Material properties for ventricular tissue and patch materials determined by Dr. Billiar were used as bases for our material model selection. Patient-specific model parameters were determined to match RV volume data measured by CMR. Details are given below.

3.1. Cardiac MRI Acquisition and Pressure Condition

It has been well accepted that high resolution MRI is capable of ventricular morphology and valve/patch/scar positions. CMR studies were performed by Dr. Tal Geva in a dedicated MRI suite located in the Department of Cardiology at Boston Children's Hospital, Harvard Medical School [16]. The CMR data were used in morphological analyses and model building in this project. RV pressure was obtained from pre-PVR cardiac catheterization.

3.2. Segmentation Method

RV/LV/Valve geometry from patient-specific 3D CMR images were also obtained by Prof. Geva through performing a semi-automatic segmentation process with QMASS® (MR Analytical Software, Medis Medical Imaging Systems, Leiden, The Netherlands), an analytical software system for quantitative analysis of cardiac MRI studies. This project was based on these segmented CMR images. A self-developed MATLAB program was used to acquire the digital contour data. For each patient or healthy volunteer, approximately 30 RV/LV positions were acquired. Figure 3.1 shows pre-operative CMR images with segmentations and the segmented contour plots from one patient with repaired TOF and severe RV dilatation at begin of filling.

(a) Pre-Operation CMR Images with Segmentations from a Patient, End of Systole
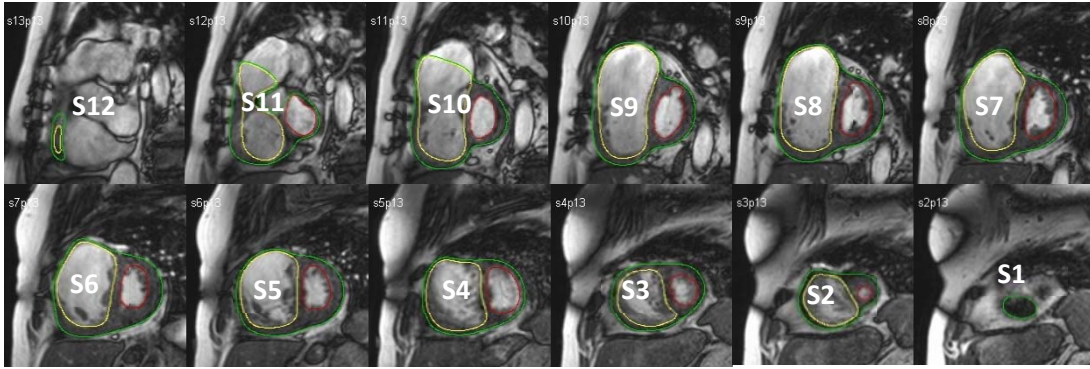
(b) Segmented Contours of RV-LV
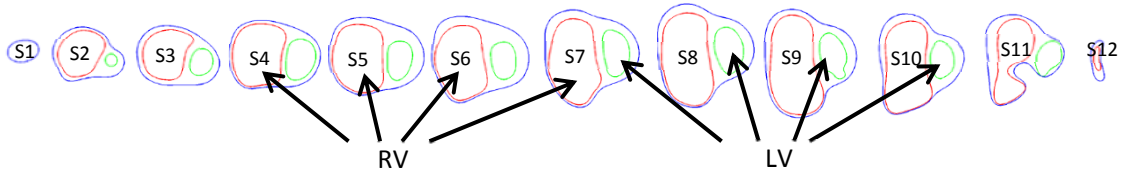
Figure 3.1. Pre-operative CMR images with the segmented contour plots from one patient with repaired TOF and severe RV dilatation at begin of filling.

3.3. Scar, Patch Information and Pressure in RV/LV

In CMR studies, CMR delayed contrast enhancement techniques have been used to get the extent and location of scar tissue and patch which will help us to determine the locations of patch/scar in construction of computation models. Figure 3.2 shows a CMRI-based re-constructed 3D geometry of RV and LV with the locations of patch, scar, tricuspid valve (inlet) and pulmonary artery (outlet). RV and LV pressure will be obtained by using catheter technique (fluid filled catheters) and used as boundary conditions in numerical simulations.
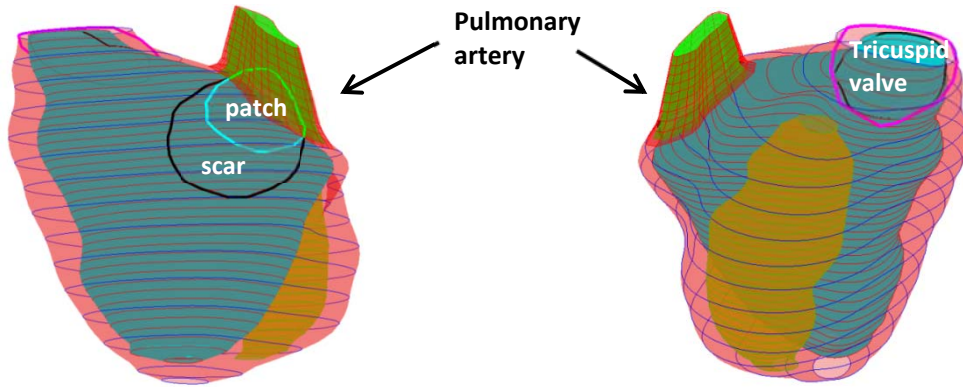
Figure 3.2. In vivo 3D MRI images of a TOF patient before PVR operation and segmented contours. (a) 12 MRI slices (S1-S16), slice spacing: 3mm. (b) Segmented contour plots showing inner and outer contours of ventricles.

3.4. Biaxial Testing of Ventricle Tissue Material Properties

Direct biaxial testing of human ventricle tissue material properties was performed by Prof. Kristen Billiar (Department of Biomedical Engineering, WPI) and will be used to guide material model selection in this project. In the direct biaxial testing, approximately 20 mm x 20 mm x 2mm slices of the right free ventricular wall and left ventricular wall specimens were used, which were dissected from two human hearts obtained within 24 hours of harvest from donors (without a history of heart disease) from National Disease Research Interchange (NDRI, Philadelphia, PA), perfused and shipped in chilled cardioplegic solution to eliminate contraction of the muscle (Figure 3.3). The preferred fiber direction was determined visually, and the ventricular sample was mounted on the biaxial test device in fiber direction aligned with the circumferential direction. Various biaxial forces were applied on the samples to obtain stretch-stress relationship of the samples. Figure 3.3(d) shows the results of direct biaxial test. Two groups of stress-strain curves were obtained where one group was from fiber direction and the other was from circumferential

direction. Detailed description of the custom biaxial testing device and method can be found from [13,102]. The stress-strain data were recorded for computational modeling use. In this project, we plan to use the modified Mooney-Rivlin model as our material model since the Mooney-Rivlin model can fit the biaxial test data well. Fung-Type model (classical model for hyperplastic material), the more popular model for ventricular tissue, is not available in ADINA. So parameter values in Mooney-Rivlin model were chosen to match Fung-Type models. Parameter values for Fung-type models are better accepted in the community. For each patient, parameter values in the model were determined to fit CMR volume data.

(a) The biaxial testing apparatus   (b) Human ventricle tissue sample

(c) Tissue sample mounted for   (d) Anisotropic stress-strain data
biaxial test   From a human ventricle slab
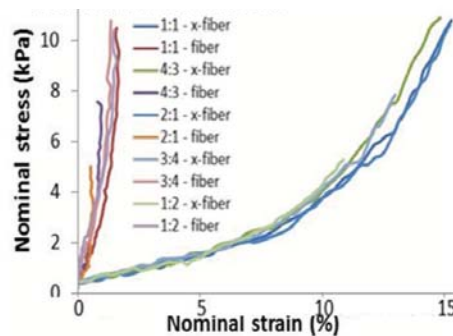
Figure 3.3. Biaxial mechanical testing and initial results. (a)The biaxial testing apparatus in Dr. Billiar's lab, (b)a human ventricle tissue sample, (c)tissue sample mounted for biaxial test, (d)anisotropic data from a human right ventricle sample.

4. 3D Geometry Reconstruction and Mesh Generation

There are three main steps involved in 3D geometry re-construction and mesh generation for human Right Ventricle FSI models: 1) acquire 3D *in vivo* MRI data; 2) re-construct 3D geometry and generate mesh for both structure and fluid domains; 3) connect fluid and structure domains and set fluid-structure interactions. Proper mesh is critical for the convergence of a 3D fluid-structure interaction model. However, the complex patient-specific ventricle structure and the existence of patch and scar significantly increase the difficulty of the mesh generation process which is very difficult to handle automatically by available commercial software. A semi-automatic procedure was introduced to generate mesh for 3D multi-component FSI models. The general idea of this technique explained as follows. For each component (made of one material) such as the ventricle, patch, scar or the fluid domain, its geometry is divided into enough volumes such that each volume has a more regular and ADINA-accepted shape for mesh/element generation. Figure 4.1 shows the volume shapes accepted by ADINA. Then, we specify an element group for each volume, which includes element style, material, and other information (such as indications assuming large strain or large displacement for kinematic formulation for the element group). After that, mesh density and mesh style is specified for each volume and elements of all the volumes were generated automatically in ADINA. Unstructured grids are significantly more difficult and complex than structured grids. However, they allow great flexibility in adapting the grid to define complex geometries because they have no constraints on their arrangement. Unstructured meshes will be selected for fluid model due to their complicated geometries and structured meshes will be used in solid model.

Hexahedron   Prism   Pyramid   Tetrahedron
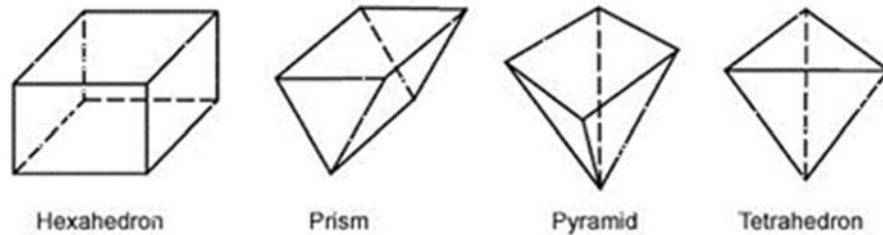
Figure 4.1. The volumes accepted by ADINA. For mesh generation, original ventricle shape should be divided into several small volumes and all the volumes have to be one of the four ADINA-accepted shapes.

The mesh generation procedure described above was used to generate 3D mesh for the following two geometrical domains:

a) Structure domain: 3D solid body defined by outer and inner surface of Right/Left ventricles with a segment of pulmonary artery.

b) Fluid domain: 3D fluid body whose external surface is defined by inner surface of Right ventricle with a segment of pulmonary artery.

The procedure is presented in details and illustrated in this chapter using the specific data (Figure 3.1) provided by Dr. Geva's group. The geometry reconstruction and mesh generation was made under ADINA computing environment.

4.1 Constructing Structure Domain

Structure Domain contains two parts, ventricles (Right and Left ventricle) and a segment of pulmonary artery. We construct ventricle and pulmonary artery domain respectively. Fig. 4.2(a) shows the stacked contours of ventricles obtained from MR images. More slices of contours were added by interpolation for computational modeling. Contours of pulmonary artery segment were

created artificially based on the instructions from Dr. Geva's team. Fig. 4.2(b) shows the stacked contours of ventricles and pulmonary artery segment after pre-modeling processing.

(a) Stacked contours of ventricles from MRIs.

(b) Stacked ventricular contours after pre-modeling processing.
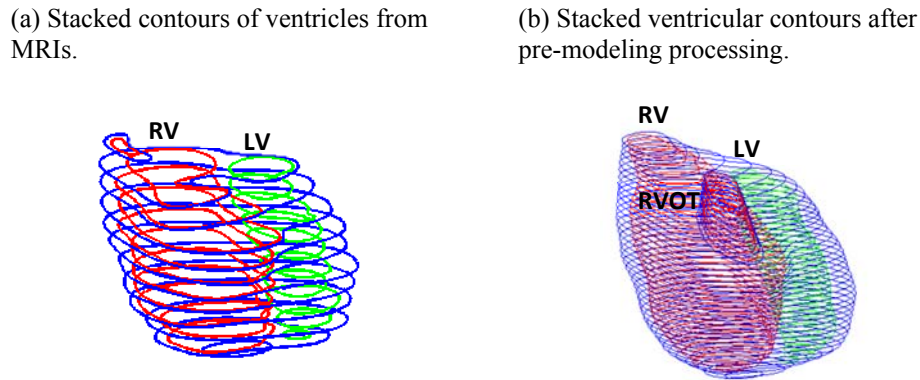
Figure 4.2. 3D stacked contours of ventricles used in computational modelling. (a) Contours from CMRIs (b) Contours after pre-modeling processing.

According to the geometric features of the pulmonary artery segment, its geometry was divided into several hexahedral volumes. However, due to the complexity of ventricle structure and the existence of scar, patch and pulmonary artery segment, including hexahedral volume mode, prismatic and pyramidal volume modes were employed to generate volumes to fit the ventricle geometry.

Each volume was generated, followed by defining the points, lines, and surfaces. One segment of ventricle part is used as example showing the procedure of volume generation specifically. To construct the structure domain, the first step is to import segmented contour data from MR images into ADINA input file (Fig. 4.3(a)), pixel by pixel. Our heart models are two-layer models which means the ventricular wall is divided to two parts, inner and outer part. Thus, some artificial contours (middle contours) were added to help construct two-layer ventricular wall. The second step is to generate proper lines based on input contour points as the edge of surface for a volume (Fig. 4.3(b) & (c) & (d)). In different slices, there are 54 polylines for lower slice (Fig.

4.3 (b)) and 68 polylines for upper slices (Fig. 4.3 (c)), going through the geometry points, generated to enclose an area which will be further assigned to be a surface. To generate the volume, the surface between two neighbored slices should also be created. Hence, 39 straight lines were generated to enclose an area between two neighboring slices (Fig. 4.3(d)). The third step is to define the surfaces by edges which were specified in the second step. The next step is to define the volume surrounded by defined surfaces. Most of volumes were hexahedron which was bounded by 6 facets with two facets in neighboring slices and 4 surfaces between these two neighboring slices. Due to the difference of structure between two slices, two prismatic volumes were introduced, which was bounded by 5 facets with one facet in the upper slice and 4 surfaces between two neighboring slices (Fig. 4.3(e)). By repeating these steps slice by slice, the geometry of the ventricles and pulmonary artery segment can be divided into several small geometry-fitting volumes.

After the volumes were constructed, element group was assigned to each volume. After specifying mesh density and mesh style for each volume, the structure domain now can be meshed in ADINA. There are a total of 244 elements generated for the example segment (Fig. 4.3(f)). All procedures described above were written in an ADINA-in file using the Adina infile program language.

(a) Points for mesh generation

Outer contours

RV inner
contours

LV inner
contours

(b) Lines defined in lower slice

Artificial contours
(middle)

RV inner contours

Outer contours

(c) Lines defined in upper slice

Artificial contours
(middle)

RV inner contours

LV inner contours

Outer contours

(d) Lines defined between two slices

interslice lines

LV

RV

(e) Volumes defined between two slices

RV

LV

prismatic volumes

(f) FE Meshes generated between two slices

RV

LV

Figure 4.3. Stages in the 3D geometry reconstruction and mesh generation of structure domain.

28

For the whole structure domain, there are a total of 1092 small volumes and 11,274 elements generated (Fig. 4.4(a) & (b)).

(a) Geometry of structure domain, consists of hexahedral/prismatic volumes

(b) Geometry and finite element mesh generation
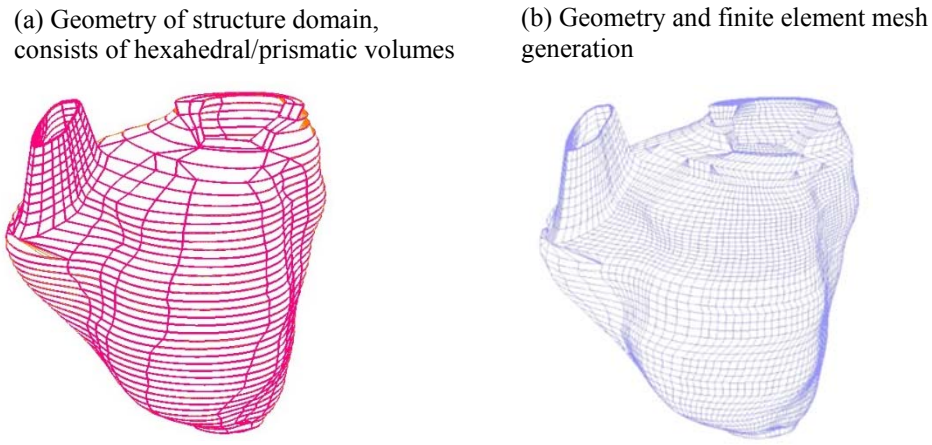
Figure 4.4. 3D geometry construction of structure domain and mesh generations. (a) geometry of structure domain (b) finite element mesh generation.

4.2 Constructing Fluid Domain

The fluid domain contains the following two parts:

1) Fluid in Right Ventricle

2) Fluid in a segment of pulmonary artery connecting with Right Ventricle

The geometries of Right Ventricle and pulmonary artery segment were constructed separately using the method in section 4.1 by hexahedral volumes. Compared with structure domain, it is easier to construct the volumes but volumes should be chosen carefully for the convergence. The 3D geometry reconstruction and mesh generation of the fluid domain were presented in Figure 4.5.

(a) Contours used to construct the fluid domain
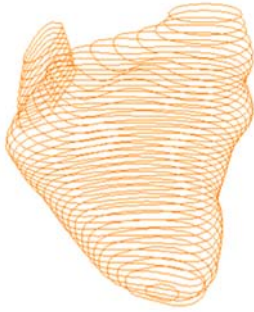
(b) Geometry of fluid domain, consists of hexahedral volumes
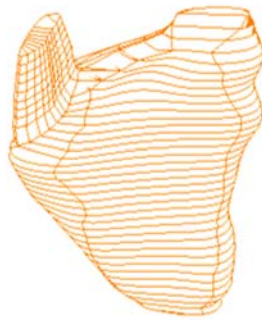
(c) Geometry and 4-node tetrahedral finite element
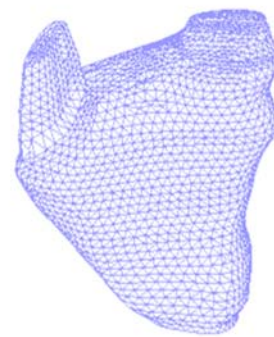
Figure 4.5. 3D geometry reconstructions and mesh generation of fluid domain (a) 3D stacked contours used in mesh generation (b) geometry of fluid domain consisting of hexahedral volumes (c) finite element meshes.

5. 3D In Vivo MRI-based FSI Models

5.1. Active Contraction of Right Ventricle

Actual RV contraction and expansion involve two different RV zero-load geometries (diastole and systole) and interconnect changes of RV volume, pressure, stress, strain, and imposed active stress or active material properties. A cardiac cycle consists of 4 phases (Phases 1 and 2 = systole; Phases 3 and 4 = diastole), pressure-volume plot of RV is given in Figure 5.1 to make it easier to understand isovolumic phases.

A: End-Filling
B: Begin-Ejection
C: End-Ejection
D: Begin-Filling
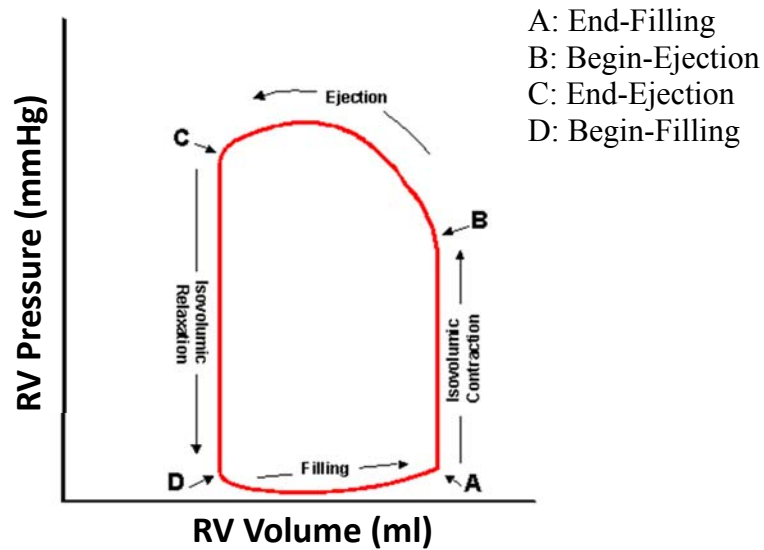
Figure 5.1. Pressure-Volume curve of RV

Phase 1. Isovolumic Contraction:

During this phase, both tricuspid (inlet) and pulmonary (outlet) valves close and RV volume don't change. Pressure in RV builds up to maximum. No-load Sarcomere Length (SL) of myocardium shortens (changing from diastolic zero-load length to systolic zero-load length). However, this sarcomere shortening is not physically observable, i.e., apparent Sarcomere Length of myocardium doesn't change since volume doesn't change. Active stress kicks in and RV strain/stress increases to peak, increased stress pushes pressure to maximum. This phase is short.

Phase 2. Ejection:

During this phase, pulmonary valve opens up (tricuspid valve still keeps closed) and ejection starts; RV volume drops; strain decreases and apparent SL shortens; no-load SL remains constant; pressure in RV drops; stress drops (pressure and stress balance each other). At end of systole, RV volume reaches its minimum.

Phase 3. Isovolumic Relaxation:

During this phase, pulmonary valve closes (both valves closed); no-load SL relaxes from systole no-load length to diastole no-load length (non-contracted length); apparent SL does not change since RV volume does not change. Strain and stress decrease to minimum. Pressure drops to minimum, so does RV stress. This phase is short.

Phase 4. Filling:

During this phase, tricuspid valve opens up (pulmonary valve still keeps closed) and filling starts; RV volume increases to its maximum; pressure in RV increases; apparent SL expands; no-load SL remains constant. Stress and strain increase. Phase 1 will follow when filling ends.

5.2. 3D FSI Model

5.2.1. Fluid Model

The blood flow will be assumed to be laminar, viscous, incompressible and Newtonian. Flow velocity at the flow-ventricle interface will be set to move with ventricular wall (no-slip condition) for unsteady flow. Natural boundary conditions (continuity of displacement, balance of stresses) will be specified at all interfaces. In fluid dynamics, when fluid flows encounter moving boundaries, the computational domain will be deformable, the Eulerian description would fail and the Lagrangian description must be used [9]. For fluid-structure interactions model, it is effective to use an Arbitrary Lagrangian-Eulerian (ALE) formulation to describe the fluid flow. Therefore,

incompressible Navier-Stokes equations with ALE formulation will be used as the governing equations which are suitable for problems with fluid-structure interactions and frequent mesh adjustments. Pressure conditions will be prescribed at the tricuspid (inlet) and pulmonary (outlet) valves. The complete flow model is given by,

Navier-Stokes equations with ALE formulation

$$\rho(\partial \mathbf{v} / \partial t + ((\mathbf{v} - \mathbf{v}_g) \cdot \nabla)\mathbf{v}) = -\nabla p + \mu \nabla^2 \mathbf{v} \tag{5.1}$$

where $\mathbf{v}$ and p are fluid velocity and pressure, $\mathbf{v}_g$ is mesh velocity, μ is blood viscosity, and ρ is the density. Reynolds number Re = ρUL/μ will be calculated and used to check the assumption about laminar, where U is the maximum velocity of the object relative to the fluid and L is a characteristic linear dimension (travelled length of the fluid).

Equation of continuity

$$\nabla \cdot \mathbf{v} = 0 \tag{5.2}$$

Boundary conditions

$$\mathbf{v}|_\Gamma = \frac{\partial x}{\partial t}, \frac{\partial \mathbf{v}}{\partial n}|_{inlet,outlet} = 0 \tag{5.3}$$

$$P_{inlet} = P_{RV}(t) \text{ (inlet open)}, \quad \mathbf{v}_{outlet} = 0 \text{ (outlet closed)} \tag{5.4}$$

$$P_{outlet} = P_{RV}(t) \text{ (outlet open)}, \quad \mathbf{v}_{inlet} = 0 \text{ (inlet closed)} \tag{5.5}$$

$$\sigma_{ij}^r \cdot n_j|_{interface,RV} = \sigma_{ij}^s \cdot n_j|_{interface} \tag{5.6}$$

where Γ represents the inner wall of right ventricle, P is the pressure and σ is structure stress tensor (superscripts r and s indicate different materials: fluid, RV tissue, scar, and patch). Inlet of RV (Tricuspid Valve) will open at the beginning of diastole and close at the end of filling. Outlet of RV (Pulmonary Valve) will open at the beginning of systole and close at the end of ejection.

5.2.2. Solid Model

The RV and LV materials will be assumed to be hyperelastic, anisotropic, nearly-incompressible and homogeneous. Scar tissue and patch material will be assumed to be hyperelastic, isotropic, nearly-incompressible and homogeneous. The governing equations for the structure models are:

Equation of Motion for Solid

$$\rho \frac{\partial^2 u_i}{\partial t^2} = \frac{\partial \sigma_{ij}}{\partial x_j}, \ i = 1, 2, 3 \tag{5.7}$$

Strain-displacement Relation

$$\varepsilon_{ij} = \frac{1}{2}\left(\frac{\partial u_j}{\partial a_i} + \frac{\partial u_i}{\partial a_j} + \sum_l \frac{\partial u_l}{\partial a_i}\frac{\partial u_l}{\partial a_j}\right), \ i, j = 1, 2, 3 \tag{5.8}$$

Nature and Traction Equilibrium Boundary Condition

$$\sigma_{ij} \cdot n_j|_{out\_wall} = 0 \tag{5.9}$$

$$\sigma_{ij}^r \cdot n_j|_{interface,RV} = \sigma_{ij}^s \cdot n_j|_{interface} \tag{5.10}$$

$$\sigma_{ij}^r \cdot n_j|_{interface,LV} = P_{LV}(t) \tag{5.11}$$

Here σ is the stress tensor, ε is Green's strain tensor, u is the displacement, and ρ is material density. AND a and x are coordinates before and after the transformation, which means that $u = x - a$. Equations (5.7)-(5.8) were used for RV/LV muscle and patch with parameter values in the constitutive equations (given below) adjusted for each material.

The nonlinear Mooney-Rivlin model will be used to describe the nonlinear anisotropic and isotropic material properties of the material with parameter values chosen to match experimental data available and adjusted to reflect stiffness variation of different materials [50,102,114]. The strain energy function for the isotropic modified Mooney-Rivlin model is given by [10,114]:

$$W = c_1(I_1 - 3) + c_2(I_2 - 3) + D_1[\exp(D_2(I_1 - 3)) - 1] \tag{5.12}$$

$$I_1 = \sum C_{ii} , \ I_2 = \frac{1}{2}[I_i^2 - C_{ij}C_{ij}] \tag{5.13}$$

where I_1 and I_2 are the first and second strain invariants, $C = [C_{ij}] = X^T X$ is the right Cauchy–Green deformation tensor $= [X_{ij}] = [\partial x_i / \partial a_j]$, (x_i) is current position, (a_i) is original position, and c_i and D_i are material parameters chosen to match experimental measurements. The strain energy function for the anisotropic modified Mooney-Rivlin model will be obtained by adding an additional anisotropic term in Eq.(5.12) [10]:

$$W = c_1(I_1 - 3) + c_2(I_2 - 3) + D_1\big[\exp\big(D_2(I_1 - 3)\big) - 1\big] + K_1/(2K_2)\exp[K_2(I_4 - 1)^2 - 1]$$

$$\tag{5.14}$$

Where $I_4 = C_{ij}(n_f)_i(n_f)_j$, C_{ij} is the Cauchy-Green deformation tensor, n_f is the fiber direction, K_1 and K_2 are material constants.

5.2.3. Fluid Structure Interactions

The fluid and structure will be coupled through their interface. The conditions of traction equilibrium and compatibility of displacements/velocities along the structure-fluid interfaces must be satisfied,

$$\boldsymbol{f}_f = \boldsymbol{f}_s \quad \text{(Traction Equilibrium)}, \tag{5.15}$$

$$\boldsymbol{v}_f = \boldsymbol{v}_s \quad \text{(Displacement Compatibility)} \tag{5.16}$$

$$\boldsymbol{v}_f = \dot{\boldsymbol{u}}_s \quad \text{(Velocity compatibility (Non slip condition))} \tag{5.17}$$

where v and f are the displacements and tractions, subscripts f and s stand for fluid and solid, respectively.

5.2.4. LV Model

For simplicity, LV will be included as a structure-only model with the same material parameter values used for RV tissues. The inclusion of LV is important to obtain the correct RV

motion and deformation. Blood flow in the LV will be not included to reduce the size of the computational code and total CPU time. A recorded LV pressure will be specified inside the LV so that the LV will expand and contract properly.

5.3. Pre Shrink-stretch Procedure: Zero-load Geometry

Simulations should start at zero-pressure status when stress and strain are zero, otherwise initial stress and strain should be provided, which are very hard to be measured in current experiments. If we start from zero-pressure status, zero-load geometry should be used as initial conditions in simulation. However, all the geometrical information of ventricles (CMR images) were obtained under in vivo condition where ventricles were pressurized so that the zero-load (under zero pressure) ventricular geometries were not known. To obtain the zero-load geometries, a pre-shrink processing would be applied to in vivo begin-diastolic ventricular geometries. Fiber direction of ventricular tissue will be considered in the pre-shrink processing, which will affect the elastic properties of ventricular tissue.

5.3.1. Model with One Zero-load Geometry (1G model)

It is very difficult to model the two isovolumic phases when the ventricular zero-load geometry, pressure, stress, and strain are changing without volume change. For simplicity, we combined the four phases into two simplified phases [114]: (a) the filling phase when RV volume and pressure increase from their minima to their maxima. This is the combination of phases 4 and 1 given in section 5.1; (b) the ejection phase when RV volume and pressure decrease from their maxima to their minima. This is the combination of phases 2 and 3 given in section 5.1.

Under this assumption, end-filling status (RV volume, pressure, stress, and strain) is same with begin-ejection status and end-ejection status is same with begin-filling status. Here we will

get only one zero-load geometry by applying pre-shrink processing on begin-diastolic ventricular geometry, then use this zero-load geometry in the whole simulation.

Active contraction and expansion were modeled by material stiffening during contraction and material softening during expansion. Stiffening the material leads to increased stress in the strain energy function. This is actually similar to adding an active stress in other active contraction models. The pre-shrink processing procedure for one zero-load geometry is described as below.

Step 1. Pre-Shrink

In vivo begin-diastole geometry (with minimal RV volume) was used as the initial geometry for pre-shrink processing. Initial inner circumferential shrinkage rate was chosen appropriately, generally we started from 2%. This initial shrinkage rate would be applied on the inner ventricular surface of in vivo begin-diastole ventricles. The volume conservation law,

$$\text{Ventricle Volume}\,|_{\text{in vivo}} = \text{Ventricle Volume}\,|_{\text{shrunk}} \qquad (5.18)$$

was employed to determine the shrinkage rate for the outer ventricular contours. The zero-load geometry was acquired by applying the circumferential shrinkage rates on in vivo begin-diastole geometry.

Step 2. Constructing Model and obtaining pressurized RV volume

Using the zero-load geometry obtained in **step 1** as the initial geometry for modelling, the structure-only model was constructed and solved under ADINA environment using the method described in chapter 4. The Right Ventricle Volume under minimal pressure (minimal volume) was desired.

Step 3. Comparison and Best Match with *In Vivo* RV volume

The obtained minimal RV volume in **step 2** was compared with the CMR data. If they didn't match as well as we desired, we adjusted the shrinkage rate for inner contours of ventricles

and the corresponding shrinkage rate for outer contours was determined due to mass conservation law. New shrinkage rates were applied on begin-diastole geometry, and repeat **step 2** to get a new model. RV volume under minimal pressure was obtained and compared with CMR data to see if pressurized RV volume matched CMR volume well. We repeated adjustment and comparison until pressurized RV matched CMR data as well as we desired.

Two 2D models were constructed to show the necessity of pre-shrink processing. One slice of in vivo MRIs at the time of minimal volume, containing RV and LV, was used in modelling. Ventricular inner and outer contours were segmented from this MRI. In one model, we applied pre-shrink processing on the contours with the 5% and 2% shrinkage rate for inner and outer contours respectively. In the other model, contours obtained from the MRI were directly in modelling without any shrinking. Minimal pressure was applied on the inner ventricular contours to recover the status with minimal volume. The quantitative comparisons with 2D model are presented below (Figure 5.2). Fig 5.2 (a) shows segmented contours based on in vivo MRI Image. Fig 5.2 (b) is the corresponding shrunk contours with 5%, and 2% shrinkage rate for inner and outer ventricular wall, respectively. However, if the simulation started directly from in vivo contours as shown in Fig. 5.2(a), the deformation is largely over-predicted and the maximum Stress-P1 value is over-estimated by 22.1% with minimal pressure loading (Fig. 5.2(c) & (d)).

(a) The in vivo 2D segmented contour

4.5 cm   1.8 cm

8.0 cm

(b) The shrunk contour

4.28 cm   1.71 cm

7.84 cm

(c) Band plot of Stress-P1 simulation starts with shrunk contour

Max = 21.3 kPa

(b) Band plot of Stress-P1 starts from non-shrunk contour.

Max = 17.4 kPa
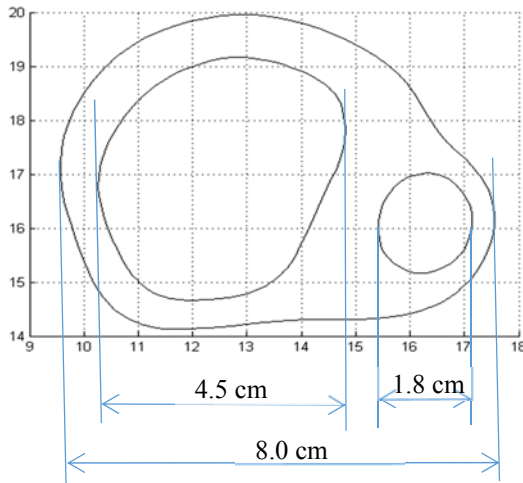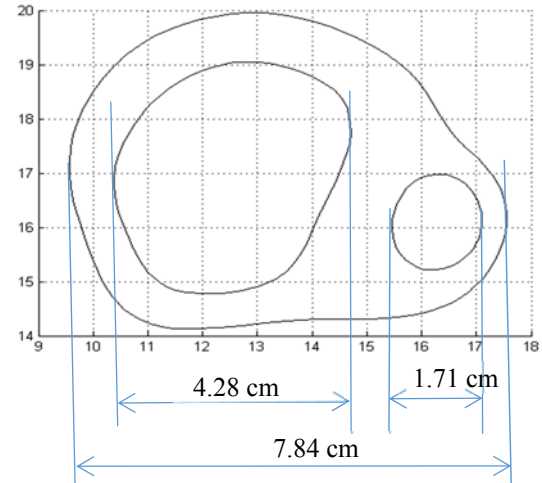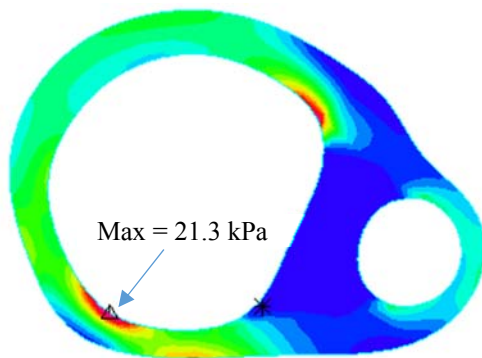
Figure 5.2. Shrink-stretch process has considerable impact on precision of simulation. (a) The in vivo 2D segmented contour of patient's ventricles; (b) Shrunk contour used as numerical start shape; (c) Band plot of Stress-P$_1$ simulation starts with shrunk contour; (d) Band plot of Stress-P$_1$ starts from non-shrunk contour.

5.3.2. Model with Two Zero-load Geometries (2G model)

Different with the assumption of the model with one zero-load geometry, in the model with two zero-load geometries, we won't combine the isovolumic phases into ejection and filling phase,

39

whereas we will omit the isovolumic phases in the simulation of the models with two zero-load geometries. In the new models, we obtained two zero-load geometries from begin-diastolic ventricular geometry by pre-shrink processing. One zero-load geometry was used in the simulation of filling phase, and the other one was used in simulation of ejection phase. Based on the ventricular movement described in section 5.1, it is well known that sarcomere length of ventricular tissue changes during the isovolumic phases indicating the change of zero-load geometry. Thus, the zero-load geometry in filling phase should be different with the one in ejection phase. Introducing two zero-load geometries in the new model is aimed to make the simulation more accurate. Experimental results about sarcomere length of ventricular tissue will be used in the pre-shrink processing.

The pre-shrink processing procedure for two zero-load geometries is similar with the procedure for one zero-load geometry. We still started from begin-diastolic ventricle geometry which has the minimal in vivo volume. Two different groups of axial and inner circumferential shrinkage rate were applied on begin-diastole geometry to obtain zero-load geometry for diastole phase and systole phase respectively. The shrinkage rates for the outer ventricular contours were determined by the mass conservation law. Based on experimental observations, zero-load geometry for diastole phase should be larger than the one for systole phase. To get the zero-load diastole geometry, we started with a 2% shrinkage, construct the model, and apply the minimum pressure to see if the pressurized RV volume matches the CMR data. If not, we adjust the shrinkage, re-made the model, pressurize it and check again. The process was repeated until RV volume matches CMR volume with error < 0.5%. For the zero-load systole geometry, assuming a 10-15% sarcomere shortening, we start with a 15% shrinkage, repeat model construction till the pressurized RV volume under end-systole pressure matched the CMR data well. Different

shrinkage rates were used for RV inner and outer surfaces due to mass conservation law. Figure 5.3 shows two different zero-load geometries used in one representative 2G model.

(a) Zero-load diastole geometry   (b) Zero-load systole geometry
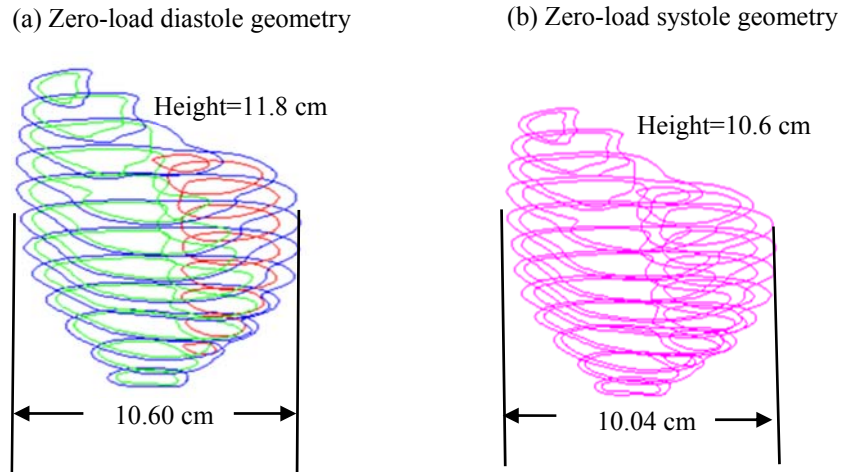
Figure 5.3. Zero-load geometries of 2G model. (a) Zero-load geometry used in diastole phase; (b) Zero-load geometry used in systole phase.

5.4 Pressure Condition

Pressure condition is one of the most important factors in determining the computational results. Figure 5.3 shows the recorded RV and LV pressure profiles obtained from one healthy people, which was used as the baseline curve for the imposed pressure conditions in our numerical models. For different patient or healthy volunteer, more patient-specific information was added in the baseline to obtain the patient-specific pressure conditions.

For each patient or healthy volunteer, we were provided only with maximal and minimal values of RV and LV pressure, not with pressure curve in one cardiac cycle. The maximal and minimal pressure values were used to modify the baseline pressure curve for acquisition of patient-specific pressure curves. We kept the curve shape of the pressure baseline, but adjusted the magnitude of the pressure curve according to maximal and minimal values of patient-specific pressure profiles.

(a) Recorded RV pressure profile.
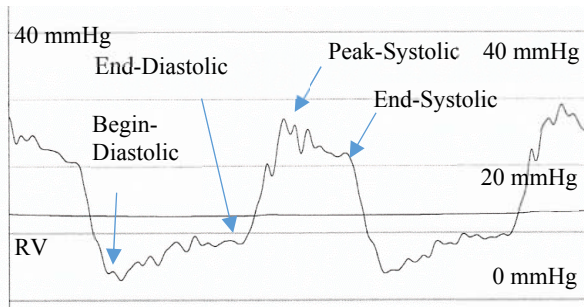
(b) RV pressure condition used in the model with Pmin, Pdia (end-filling), Pmax and Psys (end-ejection) marked.
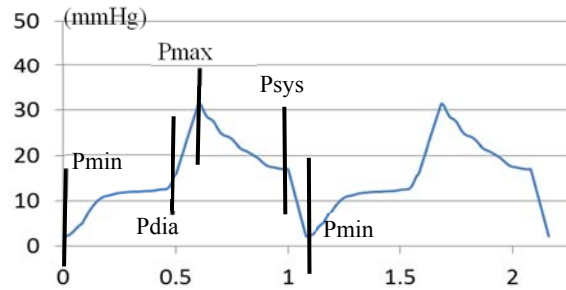
(c) Recorded aorta pressure profile.
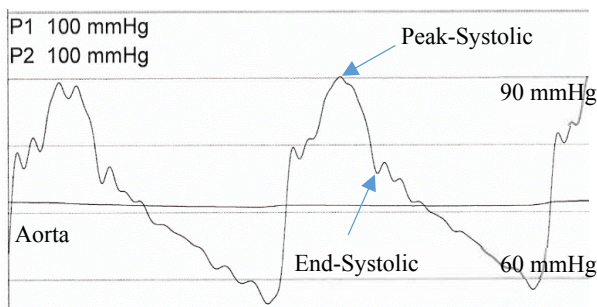
(d) Recorded LV pressure profile.
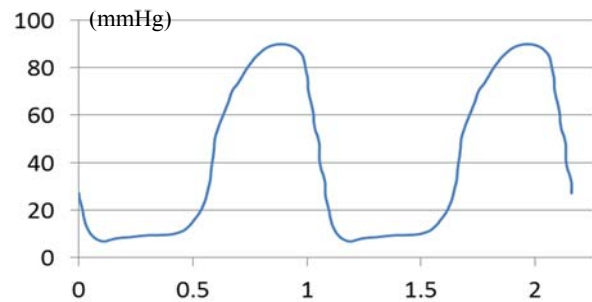
Figure 5.4. Recorded patient-specific pressure profiles and pressure conditions imposed on computational models. (a) Recorded RV pressure profile; (b) RV pressure condition used in the model with Pmin (begin-filling), Pdia (end-filling), Pmax,(begin-ejection) and Psys (end-ejection) marked; (c) recorded aorta pressure profile; (d) recorded LV pressure profile.

For the model with one zero-load geometry, we used the whole pressure curves as the numerical pressure conditions. In the model with two zero-load geometries, the part from Pmin to Pdia was used as numerical pressure conditions for the diastole phase, and the part from Pmax to Psys was used as numerical pressure conditions for the systole phase.

6. Solution Methods and ADINA Package

The models proposed in Chapter 5 were solved by a commercial software ADINA (Automatic Dynamic Incremental Nonlinear Analysis, ADINA R & D, Inc., Watertown, MA, USA) which provides a finite element program system to perform comprehensive finite element analysis of structures, heat transfer, fluids, and their interactions. For completeness, Section 6.1 briefly introduces the solution methods that are implemented in ADINA to solve fluid-structure interactions models. Section 6.2 gives a brief introduction on how to use ADINA package to perform the computation of structure-only models and fully coupled FSI models. The theoretical frame can be found in reference [9-10].

6.1. Solution Method for the FSI Model

6.1.1. 3D Finite Element Method for the Solid Model

Since 8-node hexahedral elements are most used in meshing structure part is, we will use the 8-node hexahedral element to illustrate the process of the discretization. In ADINA solver, solid model is solved by using total Lagrangian incremental nonlinear finite element method. All variables are written in terms of displacement (details see Eqn. 5.7-5.14) and the governing finite element equations are established in the displacement-based form.

Figure 6.1 shows a 3D 8-node finite element with one isoparametric coordinates. It should be noted that the isoparametric coordinates can be redefined to (-1,-1,-1), etc as needed in the AUI 'PLOT' (ADINA).

First, a series of the node-based interpolation functions are defined in the natural coordinate system of the element. Each node has a relevant interpolation function with the fundamental property that its value in the natural coordinate system is unity at this node and zero at all other nodes. Then, the element coordinates and element displacements are expressed in terms of

interpolation functions previously defined in the natural coordinate system of the element, which is the basic procedure of the isoparametric finite element formulation.
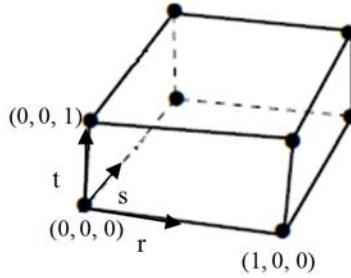
Figure 6.1. A 3D 8-node element with one isoparametric coordinates.

Specifically, the interpolation functions h_i corresponding to node i are given as below,

$$h_i(r, s, t) = G(r, r_i)G(s, s_i)G(t, t_i) \tag{6.1}$$

$$G(\alpha, \alpha_i) = \begin{cases} \alpha & if\ \alpha_i = 1 \\ 1 - \alpha & if\ \alpha_i = 0 \end{cases} \qquad \alpha = r, s, t \tag{6.2}$$

Where r_i, s_i, t_i are isoparametric coordinates of node i. r, s, t are isoparametric coordinates of any point.

Then, the coordinates and displacements can be expressed in terms of interpolation functions as,

$$x_h = \sum_{i=1}^{8} x_i\,h_i;\ \ y_h = \sum_{i=1}^{8} y_i\,h_i;\ z_h = \sum_{i=1}^{8} z_i\,h_i \tag{6.3}$$

$$u_h = \sum_{i=1}^{8} u_i\,h_i;\ \ v_h = \sum_{i=1}^{8} v_i\,h_i;\ w_h = \sum_{i=1}^{8} w_i\,h_i \tag{6.4}$$

where x_h, y_h, z_h are the coordinates and u_h, v_h, w_h are displacements at any point of the element h. x_i, y_i, z_i are the coordinates of the element nodes i and u_i, v_i, w_i are the displacements of the element nodes i ($i = 1, \dots, 8$). For clear and better expressions of the FE methods, eqn. (6.3-6.4) are re-written in matrix form as,

$$\boldsymbol{v}^{(m)} = \boldsymbol{H}^{(m)}\boldsymbol{V} \tag{6.5}$$

where the superscript m denotes the mth element, $\boldsymbol{v}^{(m)}$ is the vector of displacement components at all nodes of mth element, $\boldsymbol{H}^{(m)}$ is the vector of interpolation functions corresponding to the nodes of mth element and $\boldsymbol{V}$ is the vector of global displacement components at all nodes. After introducing interpolation functions and vector form, the governing equations for solid part given in chapter 5 can be transferred to displacement-based finite element equations. Strain-displacement relation (eqn. (5.8)) can be re-written as,

$$\boldsymbol{\varepsilon}^{(m)} = \boldsymbol{B}^{(m)}\boldsymbol{V} \tag{6.6}$$

Here, $\boldsymbol{\varepsilon}^{(m)}$ denotes the vector of strain tensor at the nodes of the mth element, $\boldsymbol{B}^{(m)}$ is coefficient matrix.

In our models, nonlinear Mooney-Rivlin model are used to describe the ventricular tissue, but due to the high complexity of the nonlinear Mooney-Rivlin model, here we use classical and relatively simple Hooke's law instead of Mooney-Rivlin model to introduce the method solution used by ADINA. In the incremental generalized Hooke's law for non-linear material properties, stress-strain relations can be written as

$$\boldsymbol{\sigma} = \boldsymbol{C}\boldsymbol{\varepsilon} \tag{6.7}$$

$$\boldsymbol{C} = C_{\text{ijrs}} = (\partial\sigma_{ij}/\partial\varepsilon_{rs} + \partial\sigma_{ij}/\partial\varepsilon_{sr})/2 \tag{6.8}$$

where $\boldsymbol{C}$ is the incremental material matrix, σ and ε are stress and strain respectively.

If the problem is a static problem, the equilibrium relations can be described as below by using the virtual displacement theorem

$$\sum_m \int_{V^{(m)}} \bar{\boldsymbol{\varepsilon}}^{(m)}\boldsymbol{\sigma}^{(m)}\, dV^{(m)} = \sum_m \int_{V^{(m)}} \bar{\boldsymbol{V}}^{(m)}\boldsymbol{f}^{B^{(m)}}\, dV^{(m)} + \sum_m \int_{S^{(m)}} \bar{\boldsymbol{V}}^{S^{(m)}}\boldsymbol{f}^{S^{(m)}}\, dS^{(m)} + \sum_i \bar{\boldsymbol{V}}^i\boldsymbol{F}^{iC}$$

$$\tag{6.9}$$

where $\bar{\boldsymbol{V}}$ are the virtual displacements and $\boldsymbol{f}^B$ is external body forces, $\boldsymbol{f}^S$ is external surface tractions, and $\boldsymbol{F}^{iC}$ is concentrated load.

From equations (6.5-6.9), the governing finite element equations in matrix form can be obtained and written as [p87-90, 11],

$$KV=R-F \qquad (6.10)$$

Where K is the stiffness matrix of the element assemblage, R is external load vector, F is concentrated load.

In our study, the loads are time-dependent, thus we need to consider the inertia forces which can be simply expressed as part of the body forces by applying d'Alembert's principle. After adding the inertia forces, the dynamic equilibrium equations become to [p165, 10],

$$M\ddot{V} + KV = R - F \qquad (6.11)$$

where M is the mass matrix of structure, and R, F, V are time dependent. $\ddot{V}$ would be expressed in terms of V at different time steps using finite difference method, then (6.11) will be solved by using modified Newton-Raphson iteration. In each iteration, the dynamic equations (6.11) become the equations which are more complicated than, but similar with the static equations (6.10). Thus, here we use the equations (6.10) to show the basic idea of the modified Newton-Raphson iteration.

Suppose that the system is in steady state at a discrete time point (pseudo-steady-state assumption), then the governing equilibrium equations (eqn. (6.10)) can be solved by using modified Newton-Raphson iteration as following equations [p493, 10], for i=1, 2, 3,...,

$$^{t+\Delta t}K^{(i-1)}\Delta V^{(i)} = {}^{t+\Delta t}R - {}^{t+\Delta t}F^{(i-1)} \qquad (6.12)$$

$$^{t+\Delta t}V^{(i)} = {}^{t+\Delta t}V^{(i-1)} + \Delta V^{(i)} \qquad (6.13)$$

with the initial conditions,

$$^{t+\Delta t}V^{(0)} = {}^{t}V, \; {}^{t+\Delta t}K^{(0)} = {}^{t}K, \; {}^{t+\Delta t}F^{(0)} = {}^{t}F \qquad (6.14)$$

where ^{t}V is the displacements of nodes, ^{t}K is the tangent stiffness matrix. First, the latest estimates of stiffness matrix $^{t+\Delta t}K^{(i-1)}$ and nodal point force $^{t+\Delta t}F^{(i-1)}$ are used to obtain the

displacement increment $\Delta V^{(i)}$ which will be used to update nodal point displacements from

$^{t+\Delta t}V^{(i-1)}$ to $^{t+\Delta t}V^{(i)}$. Then, the latest estimates of displacement $^{t+\Delta t}V^{(i)}$ will be used to update

stiffness matrix $^{t+\Delta t}K^{(i)}$ and nodal point forces $^{t+\Delta t}F^{(i)}$. The iteration will be repeated until the

solution of (6.10) reaches sufficient accuracy.

6.1.2　3D Finite Element Method for the Fluid Model

Similar with the process for structure part, we first rewrite the governing equations of fluid

model (eqn. (5.1-5.2)) to weak form. Then interpolation functions are introduced for each element,

and finite element governing equations are expressed in terms of interpolation functions.

Difference method and Newton-Raphson iteration method are also used to obtain the solution

iteratively.

First, we rewrite the governing equations for fluid model (eqn. (5.1-5.2)) in the scalar form

(see eqn. (6.14-6.16)). Then, the weak form of the governing equations are established by using

Galerkin method [9]. Specifically, eqn. (6.14) are weighted with the velocities and integrated over

the computational domain *V*. Eqn. (6.16) are weighted with the pressures and integrated over the

computational domain *V*. Integration by parts is used and simplified form are obtained as eqn.

(6.17-6.19) [p677, 10].

$$\rho \left(\frac{\partial u_i}{\partial t} + u_{i,j}\left(u_j - u_{g,j} \right) \right) = \sigma_{ij,j} \tag{6.14}$$

$$\sigma_{ij} = -p\delta_{ij} + 2\mu\varepsilon_{ij} \tag{6.15}$$

$$u_{i,i} = 0 \tag{6.16}$$

$$\int_V \bar{u}_i \rho \left(\frac{\partial u_i}{\partial t} + u_{i,j}\left(u_j - u_{g,j} \right) \right) dV + \int_V \bar{\varepsilon}_{ij}\sigma_{ij} dV = \int_{S_f} \bar{u}_i^S f_i^S dS \tag{6.17}$$

$$\sigma_{ij} n_j |_{S_f} = f_i^S \tag{6.18}$$

47

$$\int_V \bar{p} u_{i,i} dV = 0 \tag{6.19}$$

where f_i^S is the prescribed tractions on the surface S_f.

In flow part, 3D tetrahedral (4-node) elements are employed. Fig. 6.2 shows a 4-node element with one isoparametric coordinates.
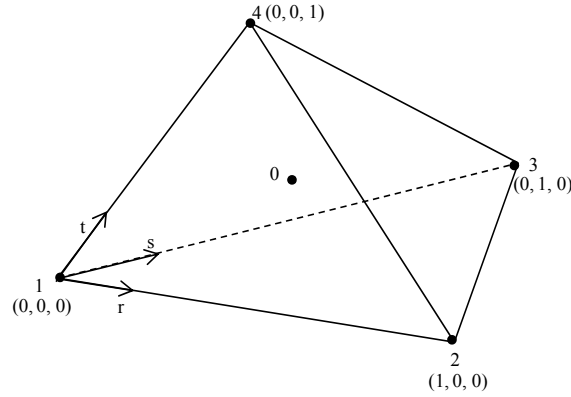
Figure 6.2 3D tetrahedral (4-node) elements using for Galerkin formulation.

In each 4-node tetrahedral element, the interpolation functions are defined at all the corner nodes h_i ($i=1,2,3,4$) and the auxiliary center node h_0, and h_0 is just used to define the velocity variable. The fundamental property of the corner-node interpolation functions (h_i ($i=1,2,3,4$)) is that its value is unity at this node and zero at all other nodes.

$$h_1 = 1-r-s-t, \quad h_2=r, \quad h_3=s, \quad h_4=t, \quad h_0=h_1h_2h_3h_4 \tag{6.20}$$

where r,s and t are isoparametric coordinates of any point.

In terms of interpolation functions h_i, all variables can be expressed as

$$p_h = \sum_{i=1}^{4} p_i h_i \tag{6.21}$$

$$\boldsymbol{u}_h = \sum_{i=0}^{4} \boldsymbol{u}_i h_i \tag{6.22}$$

where p_h and $\boldsymbol{u}_h$ are pressure and velocity at any point of the element, p_i and $\boldsymbol{u}_i$ stand for pressure and velocity at the element nodes i.

48

Assembling all the elemental variables $\{p_h\}$, $\{u_h\}$ together to U and P which present the vector of all nodel velocity and the vector of all nodal pressure respectively, the nonlinear finite elements equations for fluid model will be obtained as below under some proper boundary conditions [p678, 73],

$$
\begin{bmatrix} M & 0 \\ 0 & 0 \end{bmatrix} \begin{bmatrix} \dot{U} \\ \dot{P} \end{bmatrix} + \begin{bmatrix} K & K_p \\ K_p^T & 0 \end{bmatrix} \begin{bmatrix} U \\ P \end{bmatrix} = \begin{bmatrix} R \\ 0 \end{bmatrix}
\tag{6.23}
$$

where $\dot{U}$ and $\dot{P}$ denotes the derivative of velocity and pressure with respect to time t, R is the load vector.

First, Euler backward difference is used to rewrite $\dot{U}$ and $\dot{P}$ in terms of U and P at different times. Then, Newton-Raphson iteration method with incremental analysis is applied to solve eqn. (6.23) iteratively as follows [p835, 73],

$$
\left({}^{(t+\Delta t)} \begin{bmatrix} K & K_p \\ K_p^T & 0 \end{bmatrix}^{(i-1)} + \frac{1}{\Delta t} \begin{bmatrix} M & 0 \\ 0 & 0 \end{bmatrix} \right) \begin{bmatrix} \Delta U^{(i)} \\ \Delta P^{(i)} \end{bmatrix}
$$

$$
= \begin{bmatrix} {}^{t+\Delta t}R \\ 0 \end{bmatrix} - \left(\begin{bmatrix} M & 0 \\ 0 & 0 \end{bmatrix} \begin{bmatrix} {}^{(t+\Delta t)} \dot{U}^{(i-1)} \\ {}^{(t+\Delta t)} \dot{P}^{(i-1)} \end{bmatrix} + {}^{(t+\Delta t)} \begin{bmatrix} K & K_p \\ K_p^T & 0 \end{bmatrix}^{(i-1)} \begin{bmatrix} {}^{(t+\Delta t)} U^{(i-1)} \\ {}^{(t+\Delta t)} P^{(i-1)} \end{bmatrix} \right)
\tag{6.24}
$$

$$
\begin{bmatrix} {}^{(t+\Delta t)} U^{(i)} \\ {}^{(t+\Delta t)} P^{(i)} \end{bmatrix} = \begin{bmatrix} {}^{(t+\Delta t)} U^{(i-1)} \\ {}^{(t+\Delta t)} P^{(i-1)} \end{bmatrix} + \begin{bmatrix} \Delta U^{(i)} \\ \Delta P^{(i)} \end{bmatrix}
\tag{6.25}
$$

It should be noted that the finite element methods could be applied for incompressible fluid flow analysis only if the inf-sup condition (eqn. (6.26)) is satisfied [10, 12].

$$
\inf_{p_h \in P_h} \sup_{v_h \in V_h} \frac{\int p_h \nabla \cdot v_h \, dV}{\|p_h\|_0 \|v_h\|_1} \geq \beta > 0
\tag{6.26}
$$

where P_h is the finite element space of the pressures, V_h is the finite element space of the velocities, the subscript h denotes some element and β is a mesh-independent constant [73]. If this condition is satisfied, the elements will be optimal for the velocity and pressure interpolations; that is, the numerical scheme will be stable.

6.1.3 Fluid-Structure Interactions

Consider displacement of the structure part and velocity of the flow part as one variable vector and solve displacement and velocity simultaneously using the iterative method is known as the Direct FSI coupling method. Because of the complexity of our problem, we used the Iterative FSI coupling method in our cases, which requires less memory than the Direct FSI Coupling method.

In the iterative FSI coupling method, the fluid and solid equations will be solved individually where the latest information provided by the other part is used as boundary conditions at each time step. Specifically speaking, the solid model firstly will be solved with the latest pressure and stress condition provided by the flow part of the last time step. Then, the flow model will be solved by using the displacement and velocity obtained from the structure part as the boundary conditions. These two steps will be repeated until the convergence is reached.

6.2. ADINA Package

ADINA system has been used widely in many fields of application, including the automotive, aerospace, manufacturing, nuclear, and biomedical industries, civil engineering applications, and research. In the models for cardiovascular diseases, ADINA system has been tested and used by Tang to solve many FSI models [111-115,126-127].

The ADINA system offers a one-system program for comprehensive finite element analyses of structures, fluids, and fluid-structure interactions. The system consists of the following modules,

ADINA-AUI: The ADINA User Interface program (AUI) provides complete pre- and post-processing capabilities for all the ADINA solution programs.

ADINA-M: The ADINA Modeler (ADINA-M) is an add-on module to ADINA-AUI that provides solid modeling capabilities and direct integration with all other Parasolid-based CAD systems.

ADINA: The premium finite element program for linear and highly nonlinear analyses of solids and structures.

ADINA-F: Computational Fluid Dynamics (CFD) program for the analysis of compressible and incompressible flow with state-of-the-art capabilities for moving boundaries and automatic remeshing.

ADINA-T: Module for the heat transfer analysis of solids and field problems.

ADINA-FSI: The ADINA-FSI program is the leading code used by industries for fully coupled analysis of fluid flow with structural interactions problems.

ADINA-TMC: This module provides capabilities for thermo-mechanical coupled (TMC) analysis, including analysis of contact with heat transfer.

In this project, ADINA module and ADINA-FSI module were selected to analyze structure-only and coupled fluid flow with structural interactions, respectively. A batch of programming commands were written into input files (.in files) for the creation of structure and fluid models, and ADINA-AUI module was used to load these .in files to generate .dat files for running ADINA and ADINA-FSI program. The detail build up procedure are presented in the next section.

6.3. Build-Up Procedure Using ADINA

6.3.1. Geometry Creation

The geometry consists of points, lines, surfaces, and volumes, which are generated under ADINA computing environment. The details of the procedure are described in Chapter 4.

6.3.2. Physical Model Generation

Physical properties, such as material properties, initial conditions and boundary conditions are necessary to be specified before the FSI simulation.

Material Properties Assignment

The physical properties were assigned to the geometry model directly.

Solid Model: The RV and LV materials were assumed to be hyperelastic, anisotropic, nearly-incompressible and homogeneous. Patch and scar materials were assumed to be hyperelastic, isotropic, nearly-incompressible and homogeneous. Different material properties can be assigned to each volume to reflect the complexity of biological tissues.

Fluid model: The blood flow was assumed to be laminar, viscous, incompressible and Newtonian.

Element Group Generation

Before generating elements, the element groups for solid and fluid model need to be defined. An element group can be regarded as a container for elements which share certain common attributes, e.g. material, kinematics formulation, numerical integration order, interpolation formulation, results output [9].

Solid Model: The 3D solid element groups with Mooney-Rivlin material model were used for describing the material properties of ventricle tissue, patch and scar.

Fluid model: The density of the blood ρ and the viscosity need to be specified.

Mesh Generation

First, the 3D element types (3D Solid/3D Fluid for solid/fluid model) were selected for the volumes. Then, the mesh density was assigned by specifying the proper numbers of division along the edges of volumes. With all the settings, meshes were generated under ADINA environment.

Initial Conditions/Boundary Conditions

In structure-only models, the inner boundary of ventricular wall was specified as the pressure conditions in ventricles, and the outer boundary of ventricular wall was set as free boundary condition which means there was no constraint on the outside surface of ventricles. Inlet (pulmonary valve) and outlet (pulmonary artery) of RV were fixed by using the command "FIXBOUNDARY". All the initial values for displacement, stress and strain were set as zero.

In fluid-structure-interaction models, all the initial values of displacement, velocity, stress and strain were given as zero. Boundary conditions were defined differently and respectively in solid part and fluid part. In solid part, we specified the inner boundary of ventricular wall as the fluid-structure boundaries using ADINA command "FSBOUNDARY". And no constraint was added on the outside surface of ventricles, known as free boundary condition. Fixed boundary conditions were applied on inlet and outlet of Right Ventricle. In fluid part, we specified the outer boundary of the fluid domain as the fluid-structure boundaries. Flow velocity at the flow-structure interface was set to move with ventricular inner wall (non slip condition). The pressure conditions were specified at inlet (pulmonary valve) and outlet (pulmonary artery). In this study, patient-specific ventricular pressure was imposed.

Analysis Control

Additionally, the following control data are needed for a successful FSI simulation,

1) Master degrees of freedom: In this project, we provide only X-translation, Y-translation, Z-translation degrees of freedom, while rotation is prohibited.

2) Time function: The time function is used for applying time-dependent loads or gradually increasing loads.

3) Time step: The time step sequence is assigned to control the time/load-step increment. The assignment of time step should satisfy Courant–Friedrichs–Lewy condition (CFL condition).

4) Solution control variables: The iteration method, maximum number of iterations, iteration tolerance, and the output information are all necessary.

7. Statistical Method

7.1. Student's T-test

A t-test is any statistical hypothesis test where the test statistic follows a Student's t-distribution under the null hypothesis. It can be used to determine if two sets of data are significantly different from each other.

In our research, we will use t-test, which is two-sample location test. Two-sample location test is a test of the null hypothesis such that the means of two populations are equal. These tests are often referred to as "unpaired" or "independent samples" t-tests, as they are typically applied when the statistical units underlying the two samples being compared are non-overlapping.

The unpaired t-test is used when two separate sets of independent and identically distributed samples are obtained, one from each of the two populations being compared. Thus, when we are investigating the difference of parameters between different outcome groups for one surgery by using patient-average data, the unpaired tests can be used.

We use OFFICE EXCEL code 'ttest' to do the analysis of comparison. Simple introduction about 'ttest' is given as following:

TTEST(array1,array2,tails,type)

Array1 is the first data set,Array2 is the second data set. In our problem, Array 1 is data of group 1, and Array 2 is data of group 2. Tails specifies the number of distribution tails. If tails = 1, TTEST uses the one-tailed distribution. If tails = 2, TTEST uses the two-tailed distribution. Here we adapted two-tailed. Type is the kind of t-Test to perform, and we use type=2 meaning Two-sample equal variance (homoscedastic).

7.2. Pearson Correlation Analyses

Pearson correlation analysis is a measure of the linear correlation between two variables X and Y, giving a value between $+1$ and -1 inclusive, where 1 is total positive correlation, 0 is no correlation, and -1 is total negative correlation. It is widely used in the sciences as a measure of the degree of linear dependence between two variables.

In this study, the change of RVEF (Right Ventricular Ejection Fraction) is our focus which indicates if the RV function is improved after PVR. Pearson correlation analyses will be used to investigate the simple linear relationship between the change of RVEF and the geometrical or mechanical parameters, such as RV volume, stress etc.

Here, we use MATLAB code 'corrcoef' to implement correlation analysis, and simply introduction of 'corrcoef' is shown below.

R = corrcoef(X) returns a matrix R of correlation coefficients calculated from an input matrix X whose rows are observations and whose columns are variables. The matrix R = corrcoef(X) is related to the covariance matrix C = cov(X) by corrcoef(X) is the zeroth lag of the normalized covariance function, that is, the zeroth lag of xcov(x,'coeff') packed into a square array.

[R,P]=corrcoef(...) also returns P, a matrix of p-values for testing the hypothesis of no correlation. Each p-value is the probability of getting a correlation as large as the observed value by random chance, when the true correlation is zero. If P(i,j) is small, say less than 0.05, then the correlation R(i,j) is significant.

7.3. Linear Mixed-Effect Modelling

In this research, it is hard to obtain a large number of data due to the complexity of computational modelling. Generally, it will take around one month to construct a computational heart model for a well-trained researcher in this area. We plan to construct computational models

for 8 patients with improved outcome, 8 patients with non-improved outcome and 6 healthy subjects. If we take patient-average values as the data being investigated, it means we only have around 20 data. Due to power analysis, this data size will lead to a low power which is around 0.20. Since power is defined as 1-P(Type II error), a low power means a large P(Type II error) which means the amount of data is not enough for t-test.

To conquer the insufficiency of the data, we plan to compare the quarter-average data of different groups aiming to find some parameters which can categorize patients. For each case, the quarter-average data was obtained by the following procedure. For each slice, there are 100 points for every RV inner and outer contour. The 100 points are divided evenly into 4 parts, and we take the average for each part and set the mean value as one quarter-average value. Now for each slice, we will have 4 quarter-average values for every RV inner and outer contour and this is the quarter-average data. One patient generally has around 10 slices and then we can have approximately 40 data in the quarter-average sense for one patient. The number of data is amplified by 40 times compared with patient-average data.

Now the data is large enough for statistical analysis, unfortunately student's T-test is not suitable to compare this kind of data due to the correlation between different quarter-average values in the same case. An advanced technique, Linear Mixed-Effect Models, which allows taking into account the correlation of observations contained in a dataset, will be used here to compare the quarter-average data between different groups.

Linear Mixed-Effect Model (LMM)

Linear mixed-effects models (regression analysis) will be used to find the detailed relationships between responder and different parameters. Linear mixed-effects models are extensions of linear regression models for data that are collected and summarized in groups. These

models describe the relationship between a response variable and independent variables, with coefficients that can vary with respect to one or more grouping variables. A mixed-effects model consists of two parts, fixed effects and random effects. Fixed-effects terms are usually the conventional linear regression part and the random effects are associated with individual experimental units drawn at random from a population. The random effects have prior distributions whereas fixed effects do not. Mixed-effects models can represent the covariance structure related to the grouping of data by associating the common random effects to observations that have the same level of a grouping variable.

The formulation of the classical of LMM

$$y_i = X_i\beta + Z_ib_i + \varepsilon_i$$

Here, y_i is the vector of responses for subject i, X_i is the vector of influences, β is the design matrix (or parameters of linear model), and ε_i is the vector of residual errors. It is worth mentioning that Z_i and b_i are the matrix of covariates and the corresponding vector of random effects. Due to the existence of Z_i and b_i, the correlation of observations can be taken into account in LMM. $b_i \sim N_q(0, \mathcal{D})$ and $\varepsilon_i \sim N_{n_i}(0, \mathcal{R}_i)$ with $b_i \perp \varepsilon_i$.

Also, $\mathcal{D} = \sigma^2 D$ and $\mathcal{R}_i = \sigma^2 R_i$, and σ^2 is an unknown scale parameter. D and $\mathcal{R}_i$ will be assumed generally to be positive-definite unless stated otherwise. Several methods, including penalized least squares, maximum-likelihood estimation, can be applied to obtain the estimates of parameters $\beta, \sigma^2, \mathcal{D}, and \mathcal{R}_i$ for the classical LMM. More theoretical details can be found in the book "Linear Mixed-Effects Models Using R" by Andrzej [31]. In the real application, we will use R (a statistical software) to perform the relevant statistical analysis.

In R, the generic function lme (), which is the most frequently used function to fit LMMs in R, will be used to specify and fit linear mixed-Effects models. To fully define a LMM, the mean

structure, the random-effects structure and the grouping factors should be specified. Also, we need to define the correlation structure, variance function and model frame. Table 7.1 summarizes the needed arguments for the function lme().

Argument		Component(s) created/defined
Name	Class	
fixed	*formula*	Mean structure
	groupedData	Mean structure; grouping factors
	lmlist	
random	*reStruct*	Random-effects structure; grouping factors
correlation	*corStruct*	Correlation structure
weights	*varFunc*	Variance function
data	*data.frame*	Data
	groupedData	Data; grouping factors
method		Estimation Method

Table 7.1 R syntax: selected arguments of the function lme() used to specify a linear mixed-effects model.

The argument fixed is primarily used to define the mean structure of an LMM. A two-sided formula, such as "response ~ predictor", is the most common choice for the fixed argument.

The argument random is the primary argument used to define the random-effects structure.

The arguments weights and correlation allow to specify the residual variance-covariance matrix R_i.

The data argument is used to provide the raw data and optionally the information about the data hierarchy.

Finally, the method argument implies the method used to obtain the estimates. Generally, we have "REML" and "ML", two most common methods. "REML" means the restricted maximum likelihood method and "ML" means general maximum likelihood method.

7.4 Prediction using Median Values

Based on the results of group comparison, we may find the significant difference for some parameter between different patient groups. If there exists the significant difference, we may create some simple prediction test by using the data of healthy persons.

The basic idea is to use the median value of the patient group as threshold value to predict patient case. Take the parameter RV volume as example, and suppose that mean RV volume of patient group 1 is larger than that from patient group 2. In the prediction, if RV volume of one person is greater than the median value of the whole patient group, we will predict the person as a patient of group 1. Otherwise, the person will be predicted as one patient from group 2.

7.5 Logistic Regression Analysis and 2-fold Cross-validation Procedure

Here we have two different groups, for each experimental object we have several parameters such as volume, curvature, or blood pressure etc. Now we plan to find a parameter or a combination of parameters to predict the group categorization. Group will be taken as the outcome where the outcome will be 1 if the case belongs to target group otherwise the outcome will be 0. Thus logistic regression method will be used here to investigate the relationship between outcome and parameters.

All the possible combinations of parameters will be employed to construct logistic regression model. We will apply 2-fold Cross-validation Procedure on each model to get the estimation of model parameters and also evaluate the obtained model.

For one regression model, specifically speaking, we will separate the whole data into two groups evenly and randomly. At first we use one group as the train data and the other will be the test data. Parameters of regression model will be estimated based on the train data, the test data will be used to calculate the Area Under the ROC Curve (AUC) which can be considered as the

evaluation of regression model (Larger AUC implies the better regression model). Then we will interchange the train and test data, same procedure will be applied to get a new estimation for the model parameters and a new AUC value. For the stability and accuracy, we will repeat 2-fold Cross-validation Procedure 100 times for each regression model and mean AUC will be taken as the final evaluation for the regression model.

AUC calculation

First, we need to plot the ROC curve where false positive rate (FPR) and true positive rate (TPR) are defined as x and y axes respectively. Since TPR is equivalent to sensitivity and FPR equals to 1 - specificity, the ROC graph is sometimes called the sensitivity vs (1 - specificity) plot. The TPR defines how many correct positive results occur among all positive samples available during the test. FPR, on the other hand, defines how many incorrect positive results occur among all negative samples available during the test.

Once we have the ROC curve, AUC can be obtained approximately by using a numerical technique. We divide the x axis into several small non-overlapped intervals, in each interval the mean y value will be used as the height to calculate the area of the small rectangle, the sum of all the small rectangles will be considered as the approximation of AUC.

8. CMR-based Geometrical Analysis

In this chapter, we used the data acquired from 20 healthy volunteers (11 males, mean year : 22.8) and 56 TOF patients (37 males, mean year : 25.3), who were previously enrolled in our RV surgical remodeling trials. Based on the change of right ventricle ejection fraction (RV EF) from pre-operation to post-operation, we divided the 56 patients into two groups which were better-outcome patient group (BPG) and worse-outcome patient group (WPG). Patients with positive RV EF change (Δ RVEF) consisted of BPG and patients with negative RV EF change (Δ RVEF) consisted of WPG. 3D reconstruction models were built to obtain RV geometrical parameters such as volume, wall thickness, circumferential curvature, longitudinal curvature, surface area and surface-to-volume ratio. Firstly, comparison analyses were performed on all the geometrical parameters among different groups to see if there is any significant difference between BPG and WPG. Parameters with significant differences might be considered as potential indices to differentiate BPG from WPG. Then, correlation analyses were performed between geometrical parameters and ΔRVEF to find whether there exists any geometrical parameter significantly correlating with ΔRVEF. Statistically significant correlations indicate the potential to predict ΔRVEF. Finally, logistical regression models were constructed and tested to see which geometrical parameter or combination can provide good prediction about whether PVR surgery can improve RV function of the rTOF patients.

8.1. RV Volume and RV EF

For each patient or healthy volunteer, we have segmented CMR-based RV/LV contours (see Figure 3.1) at some evenly distributed time points covering one whole cardiac cycle. These contours provided us with the geometrical information of ventricles. Example of pre-PVR 3D

stacked contours of one TOF patient at begin of filling and begin of ejection were given in Figure 8.1.

(a) 3D stacked contours Begin of filling

(b) 3D stacked contours Begin of ejection
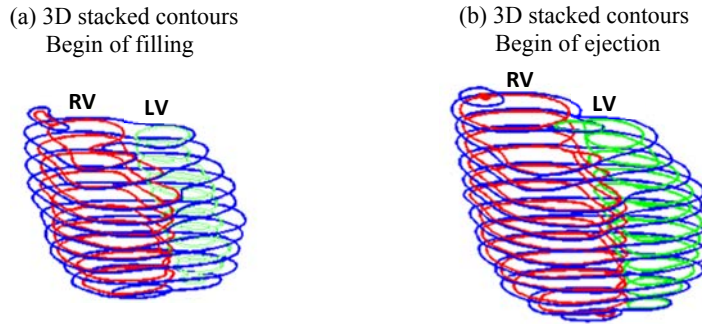
Figure 8.1 Pre-PVR 3D stacked contours of one representative patient with repaired TOF at (a) Begin of filling (b) Begin of ejection.

We approximated the volume of RV as the following equation,

$$RV\ Volume = \sum_{i=1}^{n-1} S_i \times d_i$$

here, n is the total number of the slices containing RV inner contours, S_i is the area of RV inner contour on i^{th} slice, d_i is the distance between two neighboring slices (between i^{th} and $(i+1)^{th}$ slices). Because the distance between two neighboring slices is a constant for one patient, we can use d to express the distance replacing d_i, the RV volume is given as following

$$RV\ Volume = \sum_{i=1}^{n-1} S_i \times d$$

The way to calculate the area of each RV inner contour is given as below (See Figure 8.2).

Step 1. Find the central point of the region surrounded by RV inner contour.

Step 2. Connect the central point with the points on the contour. Then the region surrounded by contour is divided into a series of triangles.

Step 3. Approximate the area of the region in the contour by adding up the areas of these triangles.

So far, we obtained RV volume at end-systole (RVESV) and RV volume at end-diastole (RVEDV), then RVEF would be calculated as RVEF=(RVEDV-RVESV)/RVEDV.
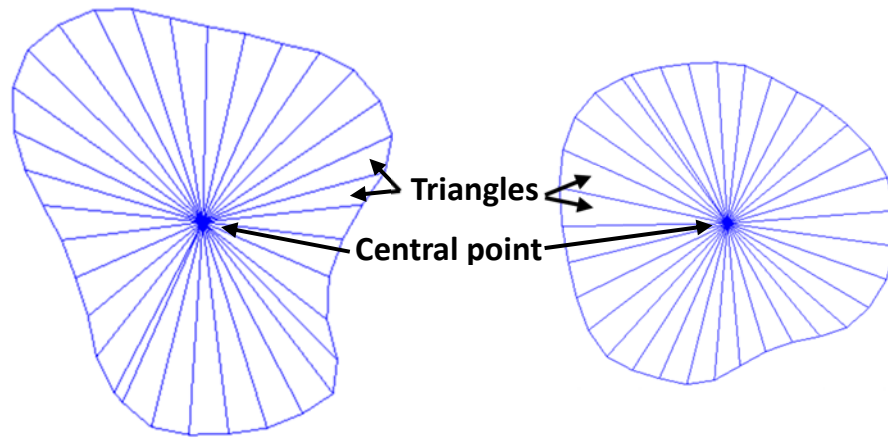
Figure 8.2. Calculation of the region surrounded by RV inner contour.

8.2. Classification based on RVEF

By using the method described in section 8.1, we could obtain RV EF of each patient before and after PVR based on their CMR-based data. Then we could determine the change of RV EF from pre-PVR to post-PVR results where RVEF change is defined as Post-RVEF subtracts Pre-RVEF.

Group 1, Best Responders		Group 2, Worst Responders			
Patient ID	Δ RVEF (%)	Patient ID	Δ RVEF (%)	Patient ID	Δ RVEF (%)
42	7.19	36	-0.18	44	-5.82
15	6.58	19	-0.21	11	-6.13
12	6.53	13	-0.29	39	-6.28
52	5.49	24	-0.43	29	-6.40
50	2.60	27	-0.60	38	-7.08
53	2.40	7	-0.79	55	-7.08
1	2.28	35	-1.04	58	-7.09
17	2.17	56	-1.15	18	-7.44
51	2.13	57	-1.28	54	-7.58
37	2.05	16	-3.03	5	-8.15
6	1.97	45	-3.33	34	-8.52
8	1.83	30	-3.89	32	-8.56
33	1.57	60	-3.90	41	-9.50
10	1.54	47	-4.02	59	-9.90
48	1.50	49	-4.08	21	-10.79
2	0.38	22	-4.56	20	-12.32
46	0.26	9	-4.81	26	-12.96
43	0.23	40	-5.44	3	-13.21
		4	-5.61	31	-13.39
Number: 18, male: 11		Number: 38, male: 28			
Average ± std: 2.7% ± 2.2%		Average ± std: -5.7% ± 3.9%			

Table 8.1. Results of RVEF, change of RVEF and classification.

Then, we divided the 56 patients into two groups based on the change in RVEF from pre-PVR to post-PVR. Better-outcome Patient Group (BPG) comprised of 18 patients with positive change in RVEF after PVR whereas Worse-outcome Patient Group (BPG) comprised of 38 patients with negative change in RVEF after PVR. Data regarding to the change in RVEF and group classification is shown in Table 8.1. P-value ($1.47 \times 10^{-11} < 0.05$) of comparison on RVEF change between two patient groups showed the significant difference of grouping.

8.3. Quarter-average Parameter Values

In this project, ventricular morphology of one patient or healthy volunteer was acquired by using planar tagged MRI at different time points during one cardiac cycle. At each time point, 10-14 equidistant planar slices were used to cover ventricles from base to apex. We were provided

with the CMR-based segmented ventricular contours. Here, CMR-based data at a time point (for example end-diastolic data) were used to explain the method for obtaining the quarter-average parameter values. Suppose there are 10 slices used to cover ventricles at end of diastole for a patient. After segmentation, we were provided with different CMR-based contours in each slice. Only inner and outer contours of ventricles were required for our analyses.

Take one slice as example, suppose there are RV inner contour, RV outer contour, LV inner contour and LV outer contour on this slice. For each contour, we have the following information: (1) total amount of points in this contour, (2) the coordinates of all the points in this contour. Generally, total number of points differs from one contour to another and the points are distributed unevenly. For the sake of convenience in the analyses, now we need to re-obtain points on each contour so that the amount of points is same for each contour and the points are equidistantly distributed. In this project, we choose the amount of points for each contour as 100. The procedure for this processing are given below.

Step 1. Choose starting points.

On each slice, we first find two paired points with similar positions in the RV inner and outer contour, and set them as the starting points of the two contours.

Step 2. Adjust starting points in longitudinal sense.

Take RV inner contours as example, all the starting points of RV inner contours were adjusted so that they could be connected as a smooth curve in longitudinal direction.

Similarly, all the starting points of other contours would lie in a longitudinal smooth curve after adjustment.

Step 3. Obtain evenly distributed points on each contour.

For each contour, begin from the adjusted starting points, 100 equidistant points are obtained by using interpolation based on the original points.

After this procedure, we would have 100 equidistant points for each contour. The points with the same number on inner and outer contour should have the similar position in planar sense. The points with the same number on the same type of contours should have the similar position in longitudinal sense.

Quarter-average Values:

Take RV part as example, first, four points were selected on every RV inner contour to divide the inner circumferential length to 4 parts evenly. Correspondingly, four points were selected on every RV outer contour having similar positions with the points on the paired inner contour.

Next, a figure of 3D-stacked contours with selected quarter points were plotted for longitudinal adjustments. All the quarter points would be adjusted according to the smoothness in longitudinal direction.

After all of the adjustments, the final quarter points could divide contours into 4 parts almost evenly. For each part, we divided it to 25 segments evenly, and then we obtained a new 100 points on each contour. All the parameters were calculated at all nodal points and averaging their quantities over the 25 points in each quarter provided the quarter-average values.

8.4. Geometrical Analysis

Wall Thickness (WT)

After choosing the start point and equidistant division, the points with the same number on inner and outer contours will be corresponding points, so the coordinates of the two corresponding

points were used to get the distance between the two points which can be considered as the thickness of the wall at the pair wise points.

Circumferential Curvature (C-cur)

Curvature is the representation of geometrical properties in mathematics, which represents how fast the unit tangent vector to the curve rotates. In our problem, we were considering the geometrical characteristics of the hearts, so it was a 3D problem. We used circumferential curvature and longitudinal curvature to describe the geometry of the RV. In this part, the method to calculate circumferential curvature was introduced. For longitudinal curvature, the calculation method was introduced in the next sub-part.

In each slice, every point had the same coordinate in z-direction. So we can consider right ventricular inner/outer contour as a planar curve. Then the circumferential curvature at each point on an RV inner/outer contour can be calculated using:

$$\kappa_c = \frac{x'y'' - x''y'}{(x'^2 + y'^2)^{3/2}} \tag{8.1}$$

Where $(x(t), y(t))$ was the parametric equation of the planar contour and the derivatives were evaluated using neighboring points on the contour. Finite Difference Method was used to get the derivate in the formula by using discrete points. Central difference was used to get a higher approximation.

For first derivate, $x_i' = \frac{x_{i+1} - x_{i-1}}{2\Delta x}$

For second derivate, $x_i'' = \frac{x_{i+1} - 2x_i + x_{i-1}}{\Delta x^2}$

Longitudinal Curvature (L-cur)

For the points in different slices, if the points had the same number, then they would be corresponding points in the longitudinal direction which means they were able to be connected as

a smooth curve in longitudinal sense. Thus in 3D view, we could use a 3D curve to connect the points with same number in different slices, and a parametric curve $\mathbf{X}$=(x(t), y(t), z(t)) could be used to describe this 3D curve, then we were able to calculate the longitudinal curvature. Longitudinal curvature at each point on RV contours can be calculated using:

$$\kappa = \frac{\sqrt{(z''(t)y'(t)-y''(t)z'(t))^2+(x''(t)z'(t)-z''(t)x'(t))^2+(y''(t)x'(t)-x''(t)y'(t))^2}}{(x'^2(t)+y'^2(t)+z'^2(t))^{3/2}} \quad (8.2)$$

where the longitudinal curve is given by $\mathbf{X}$=(x(t), y(t), z(t)), the derivatives were evaluated using points from neighboring slices vertically below and above the point being considered. Interpolations were used to obtain vertical neighboring points from the neighboring slices. One-sided formulas were used for the top and bottom slices.

Right Ventricular Surface Area and Surface-to-Volume Ratio (RV SA, RV SVR)

Right ventricular surface area (RV SA) indicates inner surface area of RV. Body surface area (BSA), which means surface area of a human body, is measured and used to define volume indexed to BSA (V_i). Specifically, volume indexed to BSA (V_i) is defined by dividing volume by BSA. Then, RV surface-to-volume ratio (RV SVR) is defined as the ratio of RV SA to RV V_i.

8.5. Comparison between Different Groups

Student t test is used to compare mean RV volume, surface area and surface-to-volume ratio between different groups. Due to the small size of data, we plan to use the quarter mean values in analysis of RV wall thickness, curvatures. However, different values in the quarter data involve correlation which makes student t test improper in the analysis of quarter data. Linear Mixed-Effect Model (LMM) is used here to compare quarter mean values of RV wall thickness, circumferential and longitudinal curvature between different groups.

8.5.1. Patient Group (PG) vs Healthy Group (HG)

Table 8.2 summarized mean values of RV WT, C-cur, L-cur, volume, SA and SVR from Patient Group (PG=BPG+WPG) and Healthy Group (HG). The results of comparative analyses between PG and HG are also given in Table 8.2. Bar plots of the average values are given in Figure 8.3 showing group differences.

At the beginning of ejection, mean RV volume of PG was 101.4% higher than that from HG (323.8 ± 85.6 cm^3 vs. 160.8 ± 44.8 cm^3, $p < 0.001$), and similar results were found at begin of filling.

Average begin-ejection SA of PG was found to be 58.1% higher than that from HG (266.8 ± 55.8 cm^2 vs. 168.7 ± 32.8 cm^2, $p < 0.001$), and similar results were also found in average begin-filling SA.

At begin of ejection, mean SVR of PG was 26.5% lower than that from HG (1.39 ± 0.31 cm^2/mL vs. 1.89 ± 0.30 cm^2/mL, $p < 0.001$). At begin of filling, mean SVR of PG was also found significantly lower than that from HG (P-value < 0.001).

Average begin-ejection WT of PG was found to be 50% higher than that from HG (0.30 ± 0.15 cm vs. 0.20 ± 0.10 cm, $p < 0.001$), and similar results were also found in average begin-filling WT.

At begin of ejection, mean C-cur of PG was 19.7% lower than that from HG (0.61 ± 0.48 1/cm vs. 0.91 ± 0.93 1/cm, $p = 0.001$). At begin of filling, mean C-cur of PG was also found significantly lower than that from HG (P-value = 0.0411).

However, L-cur was found similar between PG and HG. At begin of ejection, the mean value of L-cur from PG was 0.42 1/cm while mean HG L-cur was 0.41 1/cm (2.4% difference). At begin of filling, mean PG L-cur was 0.47 1/cm and mean HG L-cur was 0.44 1/cm (6% difference).

In sum, TOF patients were found to have large differences in geometrical parameters from healthy people. TOF patients have larger RV volume, larger RV SA, lower RV SVR, larger RV WT and smaller C-cur than healthy group at both begin of ejection and begin of filling.

	Begin of Ejection			Begin of Filling		
	PG	HG	P value	PG	HG	P value
RV volume (cm^3)	323.8±85.6	160.8±44.8	<0.001	168.1±56.5	68.3±23.0	<0.001
RV SA (cm^2)	266.8±55.8	168.7±32.8	<0.001	184.9±42.4	96.1±26.9	<0.001
RV SVR (cm^2/mL)	1.39±0.31	1.89±0.30	<0.001	1.90±0.54	2.54±0.46	<0.001
WT (cm)	0.30±0.15	0.20±0.10	<0.001	0.45±0.27	0.37±0.17	0.0139
C-cur (1/cm)	0.61±0.48	0.73±0.58	0.001	0.91±0.93	1.07±1.02	0.0411
L-cur (1/cm)	0.42±0.26	0.41±0.24	0.7212	0.47±0.31	0.44±0.28	0.2808

Table 8.2. Comparison of RV volumes, geometric parameters, between healthy group (HG) and patient group (PG) at begin of ejection and begin of filling. Data is based on quarter mean values. Values are expressed as mean ± standard deviation.
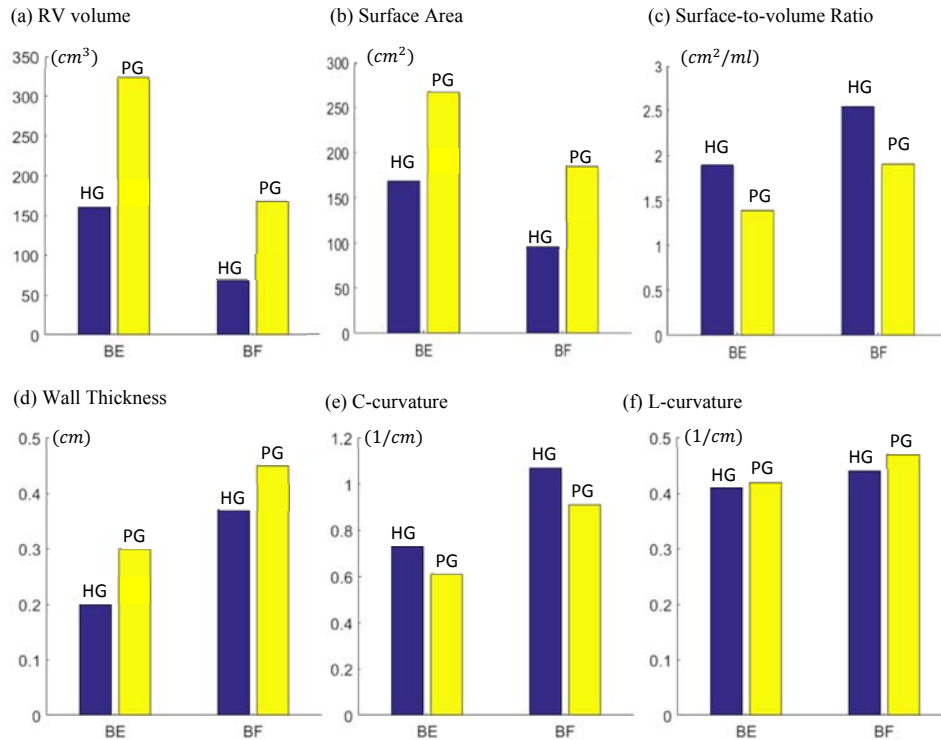
Figure 8.3 Bar plots comparing average RV volume, SA, SVR, WT, C-cur, L-cur values from Healthy Group (HG) and Patient Group (HG) at Begin-Ejection (BE) and Begin-Filling (BF). Blue: HG; Yellow: PG.

8.5.2. Better-outcome Patient Group (BPG) vs Worse-outcome Patient Group (WPG)

Table 8.3 summarized mean values of RV volume, SA, SVR, C-cur, L-cur and WT from BPG and WPG, and also showed the results of comparison between the two different outcome groups at both begin of ejection and begin of filling. Figure 8.4 gave bar plots of average parameter values, showing clear comparison between BPG and WPG. The results showed that the mean RV SA, SVR and L-cur had large differences between two patient groups. At begin of ejection, mean RV SA of BPG was 241.1 cm^2 which was 13.6% lower than that from WPG (279.0 cm^2, P-value=0.0161). Mean RV SVR of BPG was 1.26 cm^2/ml which was 13.1% lower than that from WPG (1.45 cm^2/ml, P-value=0.0271). Mean L-cur of BPG was 0.44 1/cm which was 10% higher

than that from WPG (0.40 1/cm, P-value=0.0685, *borderline*). At begin of filling, average RV SA from BPG was 46.3% lower than that from WPG (102.7 cm^2 vs 191.5 cm^2, P-value=0.0888, *borderline*). Average SVR from BPG was 15.0% lower than that from WPG (1.70 cm^2/ml vs 2.00 cm^2/ml, P-value=0.0557, *borderline*). Average L-cur from BPG was 13.3% higher than that from WPG (0.51 1/cm vs 0.45 1/cm, P-value=0.0776, *borderline*). However, RV volume, WT and C-cur were found similar between BPG and WPG especially at begin of ejection. Begin-ejection average RV volume from BPG and WPG were 296.0 cm^3 and 337.0 cm^3 respectively (12.2% difference, P-value=0.0948). Begin-filling average RV volume from BPG and WPG were 156.5 cm^3 and 173.6 cm^3 respectively (9.8% difference, P-value=0.2946). Begin-ejection average WT from BPG and WPG were 0.28 cm and 0.30 cm respectively (6.7% difference, P-value=0.2297). Begin-ejection mean C-cur from BPG and WPG were 0.60 1/cm and 0.59 1/cm (2% difference, P-value=0.7127). Thus, we may consider RV SA, SVR and L-cur as the potential indicators for PVR outcome.

	Begin of Ejection			Begin of Filling		
	BPG	WPG	P value	BPG	WPG	P value
RV volume (cm^3)	296.0±84.5	337.0±84.1	0.0948	156.5±49.5	173.6±59.3	0.2946
RV SA (cm^2)	241.1±58.3	279.0±50.9	0.0161	102.7±42.1	191.5±41.4	0.0888
RV SVR (cm^2/mL)	1.26±0.34	1.45±0.27	0.0271	1.70±0.46	2.00±0.56	0.0557
WT (cm)	0.28±0.13	0.30±0.15	0.2297	0.39±0.20	0.46±0.27	0.0558
C-cur (1/cm)	0.60±0.42	0.59±0.46	0.7127	0.81±0.58	0.90±0.95	0.1806
L-cur (1/cm)	0.44±0.28	0.40±0.23	0.0685	0.51±0.36	0.45±0.27	0.0776

Table 8.3. Comparison of RV volumes, geometric parameters, between better-outcome patient group (BPG) and worse-outcome patient group (WPG) at begin of ejection and begin of filling. Data is based on quarter mean values. Values are expressed as mean ± standard deviation. Abbreviations as in Table.
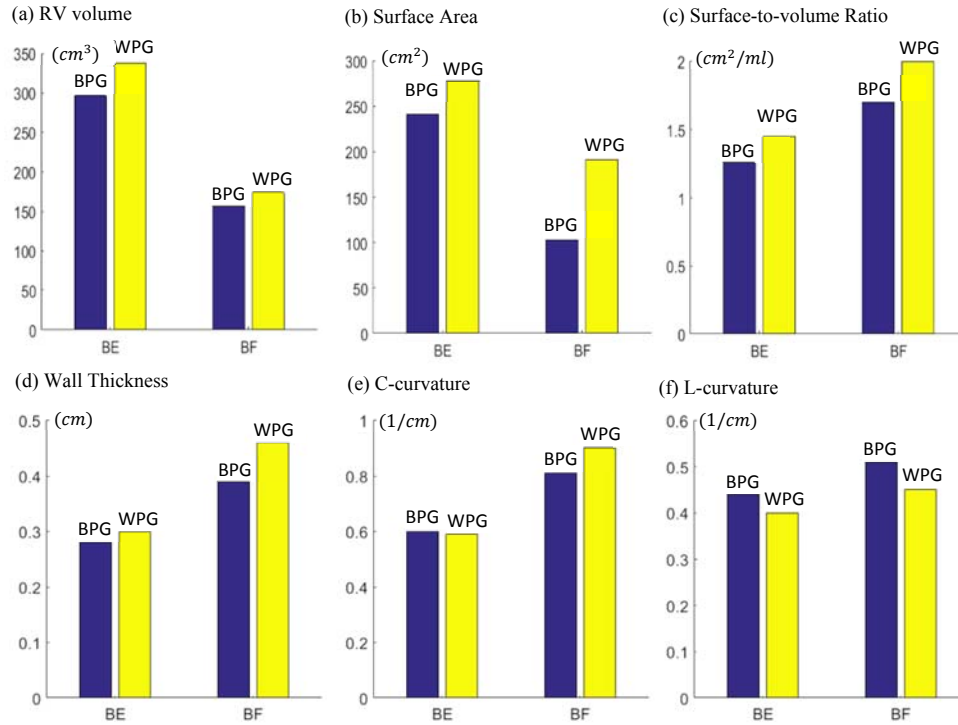
Figure 8.4. Bar plots comparing average RV volume, SA, SVR, WT, C-cur, L-cur values from Better-outcome Patient Group (BPG) and Worse-outcome Patient Group (WPG) at Begin-Ejection (BE) and Begin-Filling (BF). Blue: BPG; Yellow: WPG.

8.6. Correlation with RV EF

Furthermore, specific relationship between geometrical parameters and RV EF change is desired and important for searching good indicators of PVR response. Once the significant correlation exists between one parameter and RV EF change, the parameter might be considered as potential indicator to identify patients with better outcome after PVR.

In this analysis, patient mean values are used. Correlation analysis are implemented respectively between RV volume, SA, SVR, WT, C-cur, L-cur and RVEF change at both begin of ejection and begin of filling.

R-value shows linear correlation, and P-value shows significance of correlation. Table 8.4 and Figure 8.5 showed the results of correlation analyses. At begin of ejection, RV EF change were found negatively correlated with RV volume (R-value = -0.4088, P-value = 0.0018), SA (R-value = -0.4432, P-value = 0.0006), SVR (R-value = -0.3810, P-value = 0.0038) but positively correlated with L-cur (R-value = 0.3513, P-value = 0.0079). At begin of filling, RV EF change were also negatively correlated with RV volume (R-value = -0.3257, P-value = 0.0143), SA (R-value = -0.3314, P-value = 0.0126), SVR (R-value = -0.2843, P-value = 0.0337) and also positively correlated with L-cur (R-value = 0.2992, P-value = 0.0251). However, RV EF change didn't correlate with WT and C-cur.

	Begin of Ejection		Begin of Filling	
	R-value	P-value	R-value	P-value
RV Volume	-0.4088	*0.0018*	-0.3257	*0.0143*
RV SA	-0.4432	*0.0006*	-0.3314	*0.0126*
RV SVR	-0.3810	*0.0038*	-0.2843	*0.0337*
WT	-0.1399	0.3038	-0.2343	0.0822
C-cur	0.0153	0.9107	-0.1519	0.2638
L-cur	0.3513	*0.0079*	0.2992	*0.0251*

Table 8.4. Result of correlation analyses between Volume/WT/C-cur/L-cur and RV EF change at both begin of ejection and begin of filling.
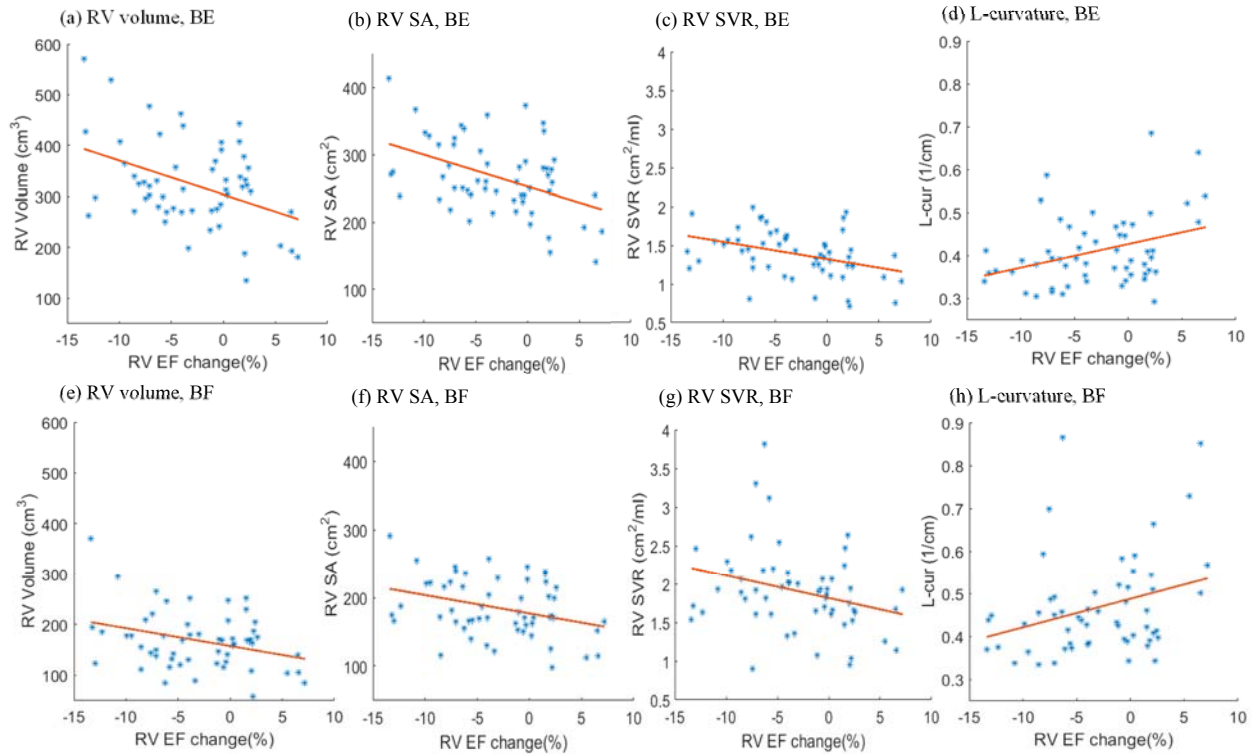
Figure 8.5. Correlation analyses between RVEF change and RV volume/SA/SVR/L-cur at begin of ejection and begin of filling.

8.7. Logistic Regression Analysis and 2-fold Cross-validation Procedure

The logistic regression method with 2-fold cross-validation procedure was used to search the best predictor for patient's group category from the combinations of the 6 geometrical parameters including WT, C-cur, L-cur, RV volume, SA and SVR. For all 63 possible combinations of the 6 geometrical parameters, the logistic regression models were constructed and their prediction accuracies were calculated for the patient's group category.

Table 8.5 showed the regression results of all the single parameters and the first 6 combinations in the order of highest to lowest prediction accuracy based on begin-ejection data. Higher accuracy indicates that the combination is able to assign patients to their ultimate outcome group more correctly. Pre-PVR SVR was the best predictor among all the combinations with an

76

area under the ROC curve of 0.658, and it is also the best single predictor. The second best single predictor was begin-ejection RV SA with an area under the ROC curve of 0.629. The best combination of parameters included SVR + C-cur with an area under the ROC curve of 0.628. The second best combined predictors were begin-ejection RV volume + SVR with an area under the ROC curve of 0.622.

Logistical Model	Cutoff prob.	Sensitivity	Specificity	Sensitivity + Specificity	AUC	Mean AUC	95% CI	Rank
SVR	0.32	0.68	0.63	1.31	0.656	0.658	0.656-0.662	1
SA	0.44	0.35	0.90	1.25	0.631	0.629	0.625-0.631	2
SVR+C-cur	0.39	0.48	0.80	1.28	0.665	0.628	0.625-0.636	3
Vol+SVR	0.28	0.71	0.50	1.21	0.605	0.622	0.608-0.625	4
SA+SVR	0.43	0.37	0.87	1.24	0.645	0.622	0.612-0.624	5
Vol+ SA	0.43	0.38	0.84	1.22	0.622	0.612	0.600-0.615	6
L-cur	0.43	0.25	0.89	1.14	0.553	0.548	0.533-0.552	44
Vol	0.47	0.16	0.94	1.10	0.496	0.532	0.529-0.539	50
WT	0.39	0.21	0.86	1.06	0.502	0.501	0.485-0.505	61
C-cur	0.79	0.01	1.00	1.01	0.438	0.428	0.425-0.432	63

Table 8.5 Prediction sensitivity, specificity, area under the curve values, and right ventricular parameters for outcome group prediction by logistic regression method. Based on data at begin of ejection. AUC average and 95% CI are based on 200 rounds of 10 repeats. AUC, Area under the curve; CI, confidence interval; WT, wall thickness.

Table 8.6 showed the regression results of all the single parameters and the first 6 combinations in the order of highest to lowest prediction accuracy based on begin-filling data. Higher accuracy indicates that the combination is able to assign patients to their ultimate outcome group more correctly. Pre-PVR L-cur + C-cur + wall thickness combination was the best predictor

among all the combinations with an area under the ROC curve of 0.696, and the best single predictor was SVR with an area under the ROC curve of 0.644. The second best single predictor was wall thickness with an area under the ROC curve of 0.629. The second best combination of parameters included begin-filling SVR + C-cur + L-cur + wall thickness with an area under the ROC curve of 0.679.

Logistical Model	Cutoff Prob.	Sensitivity	Specificity	Sensitivity + Specificity	AUC	Mean AUC	95% CI	Rank
C-cur+L-cur +WT	0.42	0.50	0.78	1.29	0.701	0.696	0.694-0.704	1
SVR+C-cur +L-cur+WT	0.30	0.64	0.65	1.29	0.684	0.679	0.677-0.682	2
SA+ C-cur +L-cur+WT	0.26	0.66	0.58	1.24	0.674	0.675	0.674-0.681	3
SVR+C-cur +L-cur	0.36	0.54	0.72	1.26	0.668	0.673	0.668-0.674	4
Vol+C-cur +L-cur+WT	0.42	0.48	0.77	1.25	0.678	0.672	0.671-0.674	5
C-cur+L-cur	0.43	0.46	0.82	1.27	0.674	0.666	0.663-0.667	6
SVR	0.34	0.64	0.69	1.33	0.647	0.644	0.642-0.645	14
WT	0.34	0.62	0.63	1.25	0.629	0.629	0.624-0.630	20
L-cur	0.33	0.46	0.78	1.24	0.598	0.584	0.582-0.588	50
SA	0.33	0.63	0.53	1.16	0.589	0.576	0.572-0.583	52
C-cur	0.28	0.83	0.29	1.12	0.557	0.554	0.553-0.561	60
Vol	0.30	0.74	0.31	1.06	0.484	0.483	0.480-0.487	63

Table 8.6 Prediction sensitivity, specificity, area under the curve values, and right ventricular parameters for outcome group prediction by logistic regression method. Based on data at begin of filling. AUC average and 95% CI are based on 200 rounds of 10 repeats. AUC, Area under the curve; CI, confidence interval; WT, wall thickness.

8.8. Conclusion

In this chapter, 3D reconstruction models were constructed based on CMR images from 20 healthy people and 56 selected rTOF patients. Morphological parameters including RV Volume, WT, C-cur, L-cur, SA and SVR were obtained and used in relevant analyses.

Comparison analyses between HG and PG shows that all morphological parameters except L-cur have significant differences, which indicates that RV morphologies of rTOF patients are significantly different from those of healthy patients.

Comparison analyses between BPG and WPG indicates that the differences of RV SA and SVR between BPG and WPG are statistically significant. L-cur of BPG has a large difference from WPG but the p-value is near the borderline (0.05). These results shows that RV SA, SVR, L-cur have the potential to differentiate BPG from WPG.

Correlation analyses between morphological parameters and ΔRVEF point out that RV volume, SA, SVR and L-cur are significantly correlated with ΔRVEF. Therefore, the four parameters might be used to predict ΔRVEF, and then equivalently these parameters have the potential to predict PVR surgery outcome.

Logistical regression models for all the possible combinations of morphological parameters were constructed and compared. At the beginning of ejection, SA and SVR have highest accuracy in predicting whether RV function can be improved after PVR surgeries among all the combinations.

In sum, RV SA and SVR are most possible predictors for PVR surgeries outcome among all the morphological parameters. RV volume and L-cur are not good as SA and SVR, but they also have the potential to predict RVP outcome well.

9. Mechanical and Geometrical Analysis Using 3D RV Models with One Zero-load Geometry

In this chapter, twenty-two 3D structure-only patient-specific active RV/LV models were constructed for 16 selected TOF patients and 6 healthy volunteers who previously enrolled in our RV surgical remodeling trial. All the models constructed in this chapter were 1G models which meant that only one zero-load geometry was used in model construction. For patients, pre- and post-PVR CMR data were obtained and pre-PVR data were used in model construction. For healthy people, CMR data at a time point were obtained and used to build models. Mechanical results, such as RV stress and strain, were obtained through numerical simulations. Morphological results, such as curvature and wall thickness, were acquired by using the methods described in Chapter 8. Mechanical and morphological results were combined together and used in the analysis to identify the factors that may be associated with improved RV function after PVR surgery. Similar with what we did in chapter 8, firstly we did correlation analyses between mechanical parameters and ΔRVEF to see whether there exists any parameter significantly correlated with ΔRVEF. Then, comparison analyses were performed among different groups to find if there exists any significant differences. Finally, we did prediction for PVR outcome by using median as threshold and logistical regression respectively to find the best predictor(s).

In the selected 22 people, there were 9 males and 13 females with median age being 42.75 years. Demographic information, RV volumes, pressure conditions, and RV EF were summarized in Table 9.1.

Patient	Sex	Age (y)	Begin-Filling Pressure	Begin-Ejection Pressure	RV EDV (cm³)	RV ESV (cm³)	RV EF (%)	ΔEF (%)
Healthy Group								
H1	F	46.7	3.6	22	128.4	46.9	63	-
H2	M	23.6	5	27.9	226.6	105.4	53	-
H3	M	20.8	4.5	24	231.7	107.0	54	-
H4	M	19.4	3.9	23.8	213.5	94.2	56	-
H5	M	17.7	4.2	24.3	233.7	105.5	55	-
H6	M	6.7	4.3	24.8	67.6	28.2	58	-
Mean		22.5	4.25	24.5	183.6	81.2	56.5	-
± SD		±13.2	±0.48	±1.93	±69.4	±34.6	±3.62	
Better-Outcome Patient Group								
P1	M	22.5	21.6	31.4	406.9	254.5	37.5	1.4
P2	F	42.0	10	45	323.3	177.8	45.0	4.0
P3	F	14.3	3	29	204.0	104.3	48.8	5.6
P4	F	15.3	2	15	193.7	105.1	45.7	6.6
P5	M	17.0	3	27	188.3	108.3	42.5	2.0
Mean		22.2	7.92	29.5	263.2	150.0	43.9	3.92
± SD		±11.5	±8.29	±10.7	±97.7	±66.2	±4.22	±2.24
Worse-Outcome Patient Group								
P6	F	38.5	6	28	328.8	196.0	40.4	-3.4
P7	M	47.7	2	31	408.8	254.8	37.7	-2.6
P8	M	50.0	3	33	364.6	239.5	34.3	-2.9
P9	F	56.9	5	41	385.1	184.6	52.1	-18.0
P10	M	11.6	10	36	204.2	121.3	40.6	-8.4
P11	M	43.5	17	65	665.1	464.0	30.2	-15.2
P12	M	54.1	4	63	334.8	170.8	49.0	-7.0
P13	F	49.5	12	52	277.2	151.3	45.4	-5.0
P14	M	17.8	2	30	365.0	178.0	51.2	-9.5
P15	F	44.6	11	50	299.0	186.0	37.8	-12.3
P16	F	45.3	9	49	571.1	371.3	35.0	-13.4
Mean		41.8	7.36	43.5	382.2	228.9	41.2	-8.88
± SD		±14.4	±4.82	±13.2	±131	±102	±7.27	±5.29

Table 9.1 Demographic and CMR data for 22 selected healthy volunteers and TOF patients with patient group assignment.

9.1 Agreement of RV volume between CMR data and numerical results

The modified anisotropic and isotropic Mooney-Rivlin models introduced in Chapter 5 were used in our computational models to describe ventricular muscle and other components (such as scar, patch and artery material) respectively.

In isotropic Mooney-Rivlin models, parameter values for patch, scar and artery were chosen as: Patch, c_1=26.5 KPa, c_2=0, D_1=26.5 KPa, D_2=9.0; Scar, c_1=13.3 KPa, c_2=0, D_1=13.3 KPa, D_2=9.0; Artery, c_1=36.8 KPa, c_2=0, D_1=14.4 KPa, D_2=2.0 . The stress-stretch plots for patch, scar and artery materials were given in Figure 9.1.
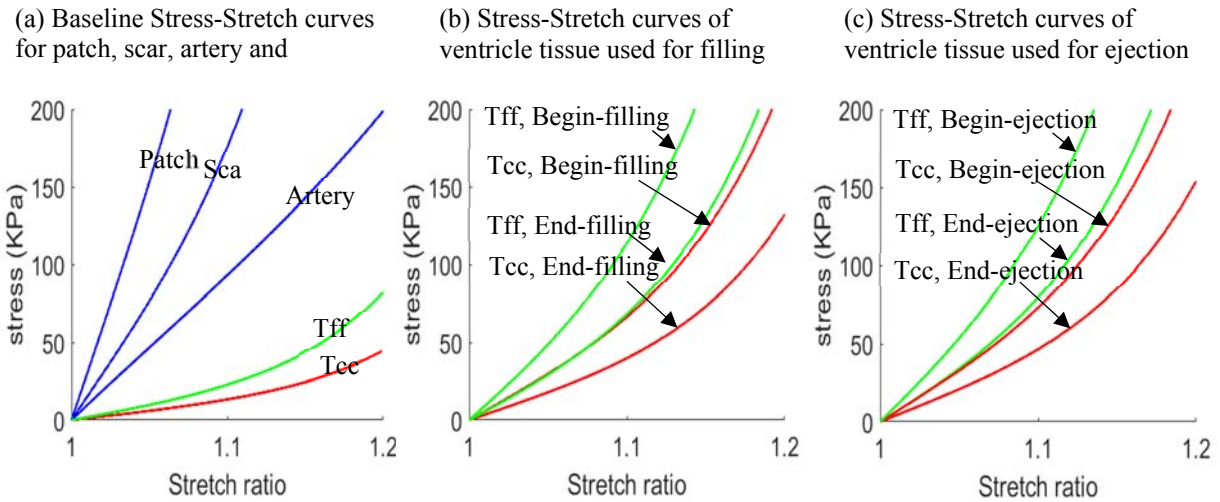
Figure 9.1 Material Stress-Stretch curves used in the representative model. (a) Baseline Stress-Stretch curves from Mooney-Rivlin isotropic patch, scar, artery and anisotropic RV tissue models. Parameter values of baseline model were defined as "1 stiff", (b) Stress-Stretch curves of ventricle tissue in the filling phase. At the begin of filling, stiffness ratio is 5.0. At the end of filling, stiffness ratio is 3.0; (c) Stress-Stretch curves of ventricle tissue in the ejection phase. At the begin of ejection, stiffness ratio is 3.5. At the end of ejection, stiffness ratio is 5.5.

In anisotropic Mooney-Rivlin model, baseline of parameters for inner ventricular tissue were chosen as c_1=3.47 KPa, c_2=0, D_1=1.09 KPa, D_2=3.00, K_1=16.61 KPa, K_2=3.00 with fiber angle 80 degree, baseline for outer ventricular tissue were set as c_1=3.96 KPa, c_2=0, D_1=1.02 KPa, D_2=3.00, K_1=16.15 KPa, K_2=3.20 with fiber angle -60 degree. The stress-stretch curves of the baseline for ventricular materials were shown in Figure 9.1. Time-dependent parameter values (c_1(t), D_1(t), K_1(t)) were chosen to fit the CMR-measured RV volume data for each patient to obtain patient-specific material models. Active contraction and expansion of myocardium were modeled by stiffening and softening material in our models which was reflected in the change of c_1(t), D_1(t), K_1(t) values.

Because patient-specific fiber orientation data were not available, we chose to construct a 2-layer RV/LV model and set fiber orientation angles using the fiber angles published by Hunter and colleagues and available human data [50]. Figure 9.2 shows Epicardial and endocardial fiber layers from human and pig hearts and how the 2-layer RV/LV model was constructed in the representative model.

| (a) Pig Model, Epicardium | (b) Human Heart, Front View | (c) Fiber orientation, a repaired TOF patient | (d) Two-layer, Construction |
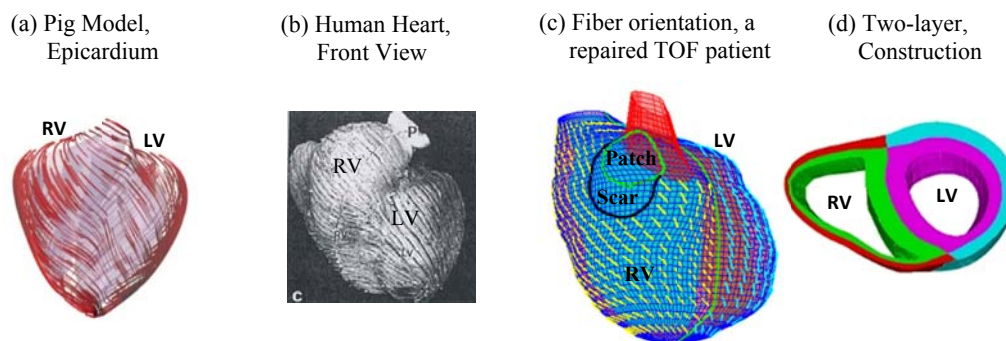
Figure 9.2. Illustration of model construction procedure using selected CMR image slices from a TOF patient. (a-b) fiber orientation from a pig model and a human heart; (c) fiber orientation from one RV/LV model of a patient with repaired TOF; (d) two-layer construction.

83

One patient model was used as a representative model to show the chosen material parameter values and the agreement of RV volume with CMR-measured values. Figure 9.1 showed the stress-stretch curves of ventricular tissues used for the representative model at the beginning and end of filling/ejection phase. Numerical RV volume-time curve of the representative model was obtained and compared with its corresponding experiment data (Figure 9.3). Table 9.2 shows computational RV volume data compared with CMR-based volume data at begin of ejection and begin of filling for all the models. Good agreement between computational and CMR-measured volume data was found (error < 3%).
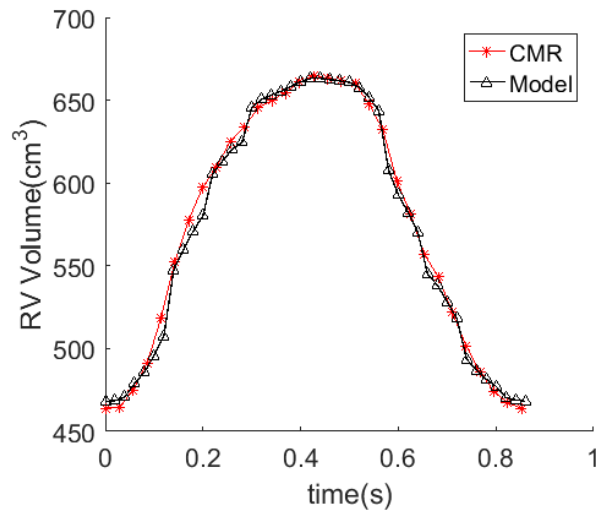
Figure 9.3 Computational volume results from the representative model showed the agreement with corresponding CMR data.

Model	MRI-based RV EDV	Numerical RV EDV	Relative difference	MRI-based RV ESV	Numerical RV ESV	Relative difference
H1	128.4	125.2	2.49	46.9	46.9	0.00
H2	226.6	227.1	0.22	105.4	106.8	1.33
H3	231.7	226.7	2.16	107.0	108.22	1.14
H4	213.5	213.1	0.19	94.2	92.4	1.91
H5	233.7	232.6	0.47	105.5	106.1	0.57
H6	67.6	66.37	1.82	28.2	28.1	0.35
P1	406.9	403.8	0.76	254.5	252.5	0.79
P2	323.3	323.8	0.15	177.8	177.5	0.17
P3	204.0	200.9	1.52	104.3	102.9	1.34
P4	193.7	193.9	0.10	105.1	104.9	0.19
P5	188.3	189.2	0.48	108.3	108.9	0.55
P6	328.8	328.3	0.15	196.0	195.7	0.15
P7	408.8	408.4	0.10	254.8	257.1	0.90
P8	364.6	363.5	0.30	239.5	238.9	0.25
P9	385.1	384.7	0.10	184.6	187.3	1.46
P10	204.2	203.3	0.44	121.3	120.9	0.33
P11	665.1	663.2	0.29	464.0	468.3	0.93
P12	334.8	331.5	0.99	170.8	171.4	0.35
P13	277.2	276.7	0.18	151.3	152.2	0.59
P14	365.0	359.3	1.56	178.0	176.8	0.67
P15	299.0	299.6	0.20	186.0	185.3	0.38
P16	571.1	572.9	0.32	371.3	371.7	0.11
Mean±Std	300.9±137.4	299.7±137.5	**0.68±0.74**	170.7±101.4	170.9±102.2	**0.66±0.51**

Table 9.2 Summary of CMR-based and numerical RV volume at begin of ejection and begin of filling with the relative difference between CMR-based data and numerical data.

9.2 Correlation analyses between Right Ventricular Ejection Fraction Change and geometrical/mechanical parameters

Table 9.3.1 & 9.3.2 summarized numerical patient-average results of mechanical and geometrical parameters including RV Stress-P_1, Strain-P_1, volume, WT, C-cur and L-cur. Correlation analyses were performed on the parameters to determine whether there exists any association between RV EF change from pre-PVR to post-PVR and RV size (RV volume and WT), geometry (C-cur and L-cur), or Stress-P_1/Strain-P_1 data. The results of correlation analyses were included in Table 9.3.1&9.3.2 and Figure 9.4.1&9.4.2. Table 9.3.1 and Figure 9.4.1 showed the

results based on begin-ejection data, while Table 9.3.2 and Figure 9.4.2 showed the results based on begin-filling data.

At begin of ejection, RV EF change correlated negatively with RV Stress-P_1 ($r = -0.56$, $P = 0.025$) and RV volume ($r = -0.60$, $P = 0.015$). However, no correlation was found between RV EF change and RV WT, C-cur, L-cur or Strain-P_1.

At begin of filling, RV EF change also correlated negatively with RV Stress-P_1 ($r = -0.52$, $P = 0.041$) and RV volume ($r = -0.52$, $P = 0.039$), but RV EF change did not correlate with RV WT, C-cur, L-cur or Strain-P_1.

Patient ID	ΔEF(%)	WT(cm)	C-cur (1/cm)	L-cur (1/cm)	RV volume (mL)	Stress-P_1 (kPa)	Strain-P_1
P1	1.4	0.39	0.47	1.24	406.9	56.9	0.29
P2	4	0.47	0.43	0.96	323.3	82.4	0.44
P3	5.6	0.48	0.5	1.2	204	61.9	0.48
P4	6.6	0.42	0.53	1.84	193.7	33.5	0.46
P5	2	0.51	0.53	1.85	188.3	42	0.4
P6	-3.4	0.34	0.39	0.77	328.8	65.3	0.43
P7	-2.6	0.65	0.37	1.01	408.8	41	0.33
P8	-2.9	0.49	0.54	1.54	364.6	64.1	0.36
P9	-18	0.48	0.42	0.91	385.1	172.1	0.66
P10	-8.4	0.41	1.34	1.32	204.2	82.9	0.49
P11	-15.2	0.8	0.36	0.59	665.1	82.4	0.23
P12	-7	0.71	0.44	0.72	334.8	83.1	0.42
P13	-5	0.45	0.46	0.97	277.2	191.7	0.66
P14	-9.5	0.43	0.65	1.6	365	65.4	0.44
P15	-12.3	0.46	0.44	1.23	299	154.3	0.51
P16	-13.4	0.59	0.33	1.25	571.1	76.2	0.34
Mean ± SD	-4.9 ±7.6	0.5 ±0.1	0.5±0.1	1.2±0.4	345.0±131	84.7±46.8	0.4±0.1
R value		-0.35	0.01	0.41	-0.60	-0.56	-0.11
P value		0.18	0.97	0.11	*0.015*	*0.025*	0.68

Table 9.3.1 Summary of patient-average values of RV volume, WT, C-cur, L-cur, Stress-P_1 and Strain-P_1 at begin of ejection and their correlations with right ventricular ejection fraction change. R and P values are for the correlations between change in RV EF and geometrical and stress/strain data.
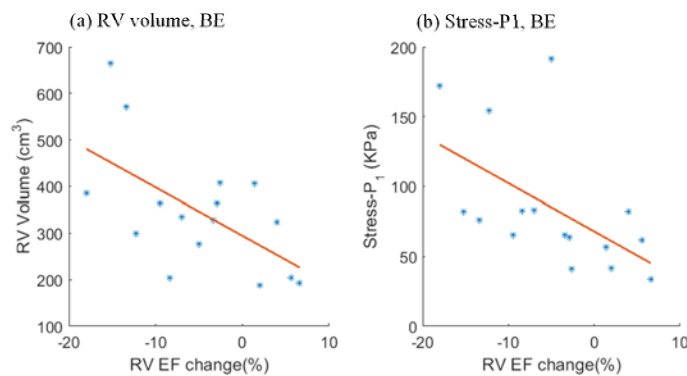
Figure 9.4.1 Correlation analyses between RVEF change and RV volume/Stress-P1 at begin of ejection.

Patient ID	ΔEF(%)	WT(cm)	C-cur (1/cm)	L-Cur (1/cm)	RV volume (mL)	Stress (kPa)	Strain
P1	1.4	0.43	0.6	1.32	254.5	2.91	0.03
P2	4	0.54	0.52	0.9	177.8	9.56	0.03
P3	5.6	0.54	0.68	1.54	104.3	2.31	0.02
P4	6.6	0.47	0.69	2.31	105.1	2.16	0.02
P5	2	0.53	0.67	1.75	108.3	2.04	0.03
P6	-3.4	0.38	0.48	0.75	196	9.03	0.14
P7	-2.6	0.71	0.45	0.84	254.8	1.55	0.03
P8	-2.9	0.54	0.64	1.37	239.5	3.65	0.05
P9	-18	0.52	0.54	0.89	184.6	7.88	0.09
P10	-8.4	0.46	1.46	1.41	121.3	13.23	0.14
P11	-15.2	0.87	0.4	0.65	464	15.83	0.04
P12	-7	0.85	0.57	0.82	170.8	2.64	0.01
P13	-5	0.5	0.54	0.87	151.3	17.8	0.16
P14	-9.5	0.53	0.9	1.49	178	3.23	0.01
P15	-12.3	0.47	0.54	1.23	186	15.03	0.14
P16	-13.4	0.66	0.41	1.32	371.3	8.31	0.04
Mean ± SD	-4.9 ±7.6	0.6 ±0.1	0.6±0.3	1.2±0.4	204.2±97.9	7.3±5.6	0.1±0.1
R value		-0.33	0.059	0.49	-0.52	-0.52	-0.35
P value		0.21	0.83	0.056	*0.039*	*0.041*	0.18

Table 9.3.2 Summary of patient-average values of RV volume, WT, C-cur, L-cur, Stress-P_1 and Strain-P_1 at begin of filling and their correlations with right ventricular ejection fraction change. R and P values are for the correlations between change in RV EF and geometrical and stress/strain data.
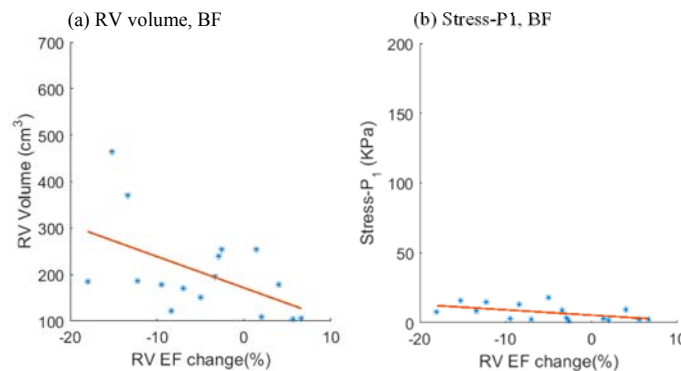
Figure 9.4.2 Correlation analyses between RVEF change and RV volume/Stress-P1 at begin of filling.

9.3 Group Comparison

Based on their RV ejection fraction (EF) changes, the patients were categorized into two groups, the Better-Outcome Patient Group (BPG, n=5) which had positive RV EF changes (RV EF change: 3.94 ± 2.20) and Worse-Outcome Patient Group (WPG, n=11) which had negative RV EF changes (RV EF change: -8.88 ± 5.30, p-value: 0.00015) (See Table 9.1). 6 healthy volunteers consisted of healthy group (HG). Comparison analyses were performed among three groups on all the geometrical and mechanical parameters. For RV volume, patient-average values and student T test were used in the comparative analyses. For the other parameters (including RV WT, C-cur, L-cur, Stress-P_1 and Strain-P_1), quarter mean values and Linear Mixed-Effect Model were used in the comparative analyses.

9.3.1 HG vs PG

Comparison of geometrical parameters

Table 9.4 summarized and compared the average values of geometrical parameters (RV volume, wall thickness, L-cur and C-cur) between healthy group (HG) and patient group (PG = BPG + WPG). Bar plots of the average values are given in Figure 9.5 showing group differences. RV volume was the parameter with the most noticeable difference between HG and PG. At the beginning of ejection, average PG RV volume was 87.9% higher than that from HG (344.9 ± 131.3 cm^3 vs. 183.6 ± 69.4 cm^3, p=0.0102). At the beginning of filling, average RV volume of PG was 151.5% higher than that from HG (204.2 ± 97.9 cm^3 vs. 81.2 ± 34.6 cm^3, p=0.0076). The high percentage difference at begin-filling was due to the fact that RV of PG contracted much less that HG.

C-cur and L-cur also showed large differences between HG and PG. At begin of ejection, mean PG C-cur was 35.8% lower than mean HG C-cur (0.52 ± 1.21 1/cm vs. 0.81 ± 1.05 1/cm,

p=0.0237), and mean PG L-cur was 38.4% higher than mean HG L-cur (1.19 ± 1.21 1/cm vs. 0.86 ± 0.71 1/cm, p=0.0756). At begin of filling, average C-cur of PG was 22.9% lower than that from HG (0.64 ± 1.23 1/cm vs. 0.83 ± 0.51 1/cm, p=0.1519), and average L-cur of PG was 23.2% higher than that from HG (1.22 ± 1.22 1/cm vs. 0.99 ± 0.66 1/cm, p=0.2585).

It is worth noting that the ratio of L-cur over C-cur for PG at begin-ejection is 2.29, compared to 1.06 for HG. At begin of filling, the ratio of L-cur over C-cur for PG is 1.90, compared to 1.19 for HG. So PG average RV longitudinal curvature is 100% greater than PG average circumferential curvature, while L-curvature and C-curvature for HG were about equal.

RV WT did not show much differences between HG and PG. That is clear from both Table 9.4 and Figure 9.5.

	Begin of Ejection			Begin of Filling		
	PG	HG	P value	PG	HG	P value
RV volume (cm^3)	344.9±131.3	183.6±69.4	0.0102	204.2±97.9	81.2±34.6	0.0076
WT (cm)	0.51±0.24	0.51±0.30	0.9315	0.57±0.27	0.64±0.32	0.3616
C-cur (1/cm)	0.52±1.21	0.81±1.05	0.0237	0.64±1.23	0.83±0.51	0.1519
L-cur (1/cm)	1.19±1.21	0.86±0.71	0.0756	1.22±1.22	0.99±0.66	0.2585
Stress-P$_1$ (kPa)	82.2±79.4	51.2±55.7	0.1031	7.31±8.49	3.00±2.30	0.0831
Strain-P$_1$	0.43±0.19	0.51±0.17	0.1486	0.06±0.07	0.07±0.06	0.5376

Data is based on quarter mean values. Values are expressed as mean ± standard deviation.

Table 9.4 Comparison of RV volumes, geometric parameters, and stress/strain values between healthy group (HG) and patient group (PG=BPG+WPG) at begin of ejection and begin of filling.

(a) RV volume   (b) Wall Thickness

(c) C-curvature   (d) L-curvature
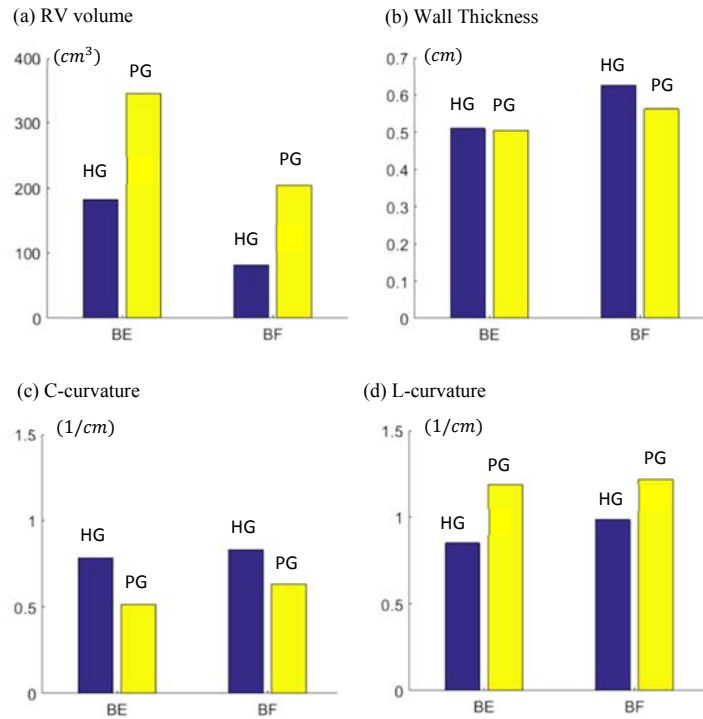
Figure 9.5 Bar plots comparing average RV volume, WT, C-cur, L-cur values from Healthy Group

(HG) and Patient Group (HG) at Begin-Ejection (BE) and Begin-Filling (BF). Blue: HG; Yellow:

PG.

Comparison of mechanical parameters

Figure 9.6 gave stress and strain plots of one healthy volunteer and one TOF patient at Begin-Ejection and Begin-Filling respectively. Without patch and scar, Stress-P_1 and Strain-P_1 distributions of the healthy volunteer were more uniform than that from the TOF patient model near the patch area. Table 9.4 also summarized and compared RV maximum principal stress and strain (denoted by Stress-P_1 and Strain-P_1) between HG and PG. Figure 9.7 gave the bar plots of average stress and strain values, showing clear comparisons between healthy group and patient group. At the beginning of ejection, average Stress-P_1 of PG was 60.5% higher than that from HG (82.2 ± 79.4 kPa vs. 51.2 ± 55.7 kPa, p=0.1031). At the beginning of filling, mean Stress-P_1 of PG

was 143.7% higher than that from HG (7.31±8.49 kPa vs. 3.00±2.30 kPa, p=0.0831). The high

percentage should be discounted because the overall stress values were small. At begin of ejection,

average Strain-P_1 from HG was 18% higher than that from PG. Noticing that average Strain-P1

values from both HG and PG at begin-filling were about the same, higher strain from HG means

that healthy ventricles had better contractibility, consistent with our expectations.

(a) Stress-P_1, Healthy Begin-Ejection
Max= 601.9 kPa

(b) Strain-P_1, Healthy Begin-Ejection
Max= 0.884

(c) Stress-P_1, Healthy Begin-Filling
Max= 41.27 kPa

(d) Strain-P_1, Healthy Begin-Filling
Max= 0.192

(e) Stress-P_1, Patient Begin-Ejection
Max= 560.5 kPa

(f) Strain-P_1, Patient Begin-Ejection
Max= 0.7617

(g) Stress-P_1, Patient Begin-Filling
Max= 127.8 kPa

(h) Strain-P_1, Patient Begin-Filling
Max= 0.2039

Min Universal Scale Max

Figure 9.6 Stress and strain plots from one healthy volunteer (a)-(d) and one TOF patient (e)-(h)

showing stress/strain distribution patterns.

(a) Stress-P_1
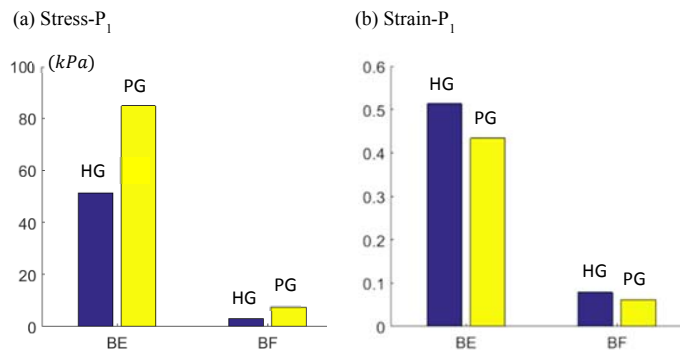
(b) Strain-P_1

Figure 9.7 Bar plots comparing average Stress-P1 and Strain-P1 values from Healthy Group (HG)

and Patient Group (HG) at Begin-Ejection(BE) and Begin-Filling (BF). Blue: HG; Yellow: PG.

9.3.2 HG may help differentiate BPG from WPG

Comparison between BPG and WPG

Table 9.5 showed mean values and results of comparative analyses between BPG and WPG. RV volume, L-cur and Stress-P_1 showed large differences between two patient groups. WT, C-cur and Strain-P_1 were found to be similar between two patient groups.

At begin of ejection, mean RV Stress-P_1 of BPG was 42.0% lower than that from WPG (54.7±38.4 kPa vs 94.3±89.2 kPa; *P*=0.09). Mean RV volume of BPG was 31.1% lower than that from WPG (263.2±97.7 mL vs 382.1±131.1 mL; *P*=0.09). Mean L-cur of BPG was 30.3% higher than that from WPG (1.42±1.40 1/cm vs 1.09±1.11 1/cm; *P*=0.12). At begin of filling, the comparison gave similar results. However, significance (P-value < 0.05) was only found in L-cur at the beginning of filling.

Parameter	Begin of ejection			Begin of filling		
	BPG	WPG	P value	BPG	WPG	P value
RV volume (mL)	263.2±97.7	382.1±131.1	0.09	150.0±66.2	228.9±102.4	0.14
WT (cm)	0.45±0.20	0.53±0.26	0.29	0.50±0.21	0.60±0.29	0.27
C-cur	0.49±0.26	0.54±1.45	0.79	0.63±0.34	0.64±1.46	0.94
L-cur	1.42±1.40	1.09±1.11	0.12	1.58±1.56	1.07±1.00	0.03
Stress	54.7±38.4	94.3±89.2	0.09	3.76±4.17	8.87±9.39	0.09
Strain	0.41±0.18	0.43±0.20	0.71	0.03±0.02	0.08±0.07	0.07

Table 9.5 Comparison of RV volumes, geometric parameters and stress/strain between BPG and WPG at the beginning of ejection and beginning of filling.

Compare HG to BPG and WPG

Table 9.6 summarized and compared geometrical and mechanical parameter values of BPG and WPG to HG. Figure 9.8 gave the bar plots of average Stress-P_1, Strain-P_1, RV volume, C-cur, L-cur and WT at begin-ejection, showing the differences among the three groups.

Stress-P_1 from BPG was found to be closer to that from HG, compared to Stress-P_1 of WPG. At the beginning of ejection, mean Stress-P_1 of BPG was only 6.8% higher than that from HG (54.7±38.4 kPa vs. 51.2±55.7 kPa, p=0.6889), and the difference was not significant; while average Stress-P_1 of WPG was 84.1% higher than that of HG (94.3±89.2 kPa vs. 51.2±55.7 kPa, p=0.0418), and the difference was significant. At the beginning of filling, average Stress-P_1 of BPG was 25% higher than that from HG (3.76±4.17 kPa vs. 3.00±2.30 kPa, p=0.5968), while average Stress-P_1 of WPG was 195.7% higher than that of HG (8.87±9.39 kPa vs. 3.00±2.30 kPa, p=0.0290). *The results suggested that comparing patient's RV stress values with healthy RV stress values may help identify patients with possible better outcome.*

Similarly, BPG RV volumes at Begin-Ejection were closer to HG RV volumes (263 cm^3 vs. 184 cm^3, 43% higher) compared to WPG volumes (382 cm^3 vs. 184 cm^3, 107% higher). BPG L-curvature was much greater than HG L-curvature at Begin-Ejection (1.42 vs. 0.86 1/cm, 65% higher) than WPG L-cur over HG (1.09 vs. 0.86 1/cm, 27% higher). Based on these results, RV volume and L-cur could be useful in identifying better-outcome patients.

Table 9.6 and Figure 9.8 showed that differences in wall thickness, C-cur and Strain-P_1 between BPG and WPG may not be very useful in differentiating BPG patients from WPG patients.

	Begin of Ejection (maximal volume and pressure)			Begin of Filling (minimal volume and pressure)		
	BPG	HG	P value	BPG	HG	P value
RV volume (cm³)	263.2±97.7	183.6±69.4	0.1482	150.0±66.2	81.2±34.6	0.0534
WT (cm)	0.45±0.20	0.52±0.30	0.4441	0.50±0.21	0.64±0.32	0.1099
C-cur (1/cm)	0.49±0.26	0.81±1.05	0.0094	0.63±0.34	0.83±0.51	0.0082
L-cur (1/cm)	1.42±1.40	0.86±0.71	0.0263	1.58±1.56	0.99±0.66	0.0420
Stress-P_1 (kPa)	54.7±38.4	51.2±55.7	0.6889	3.76±4.17	3.00±2.30	0.5968
Strain-P_1	0.41±0.18	0.51±0.17	0.1042	0.03±0.02	0.07±0.06	0.1047
	WPG	HG	P value	WPG	HG	P value
RV volume (cm³)	382.1±131.1	183.6±69.4	0.0038	228±102.4	81.2±34.6	0.0041
WT (cm)	0.53±0.26	0.52±0.30	0.8150	0.60±0.29	0.64±0.32	0.6508
C-cur (1/cm)	0.54±1.45	0.81±1.05	0.0709	0.64±1.46	0.83±0.51	0.2427
L-cur (1/cm)	1.09±1.11	0.86±0.71	0.2006	1.07±1.00	0.99±0.66	0.6194
Stress-P_1 (kPa)	94.3±89.2	51.2±55.7	0.0418	8.87±9.39	3.00±2.30	0.0290
Strain-P_1	0.43±0.20	0.51±0.17	0.2603	0.08±0.07	0.07±0.06	0.9860

Table 9.6 Comparison of geometric and stress/strain mean values between healthy group (HG) and patient groups (better-outcome patient group (BPG), worse-outcome patient group (WPG) at begin of ejection and begin of filling. Data is based on quarter mean values. Values are expressed as mean ± standard deviation.
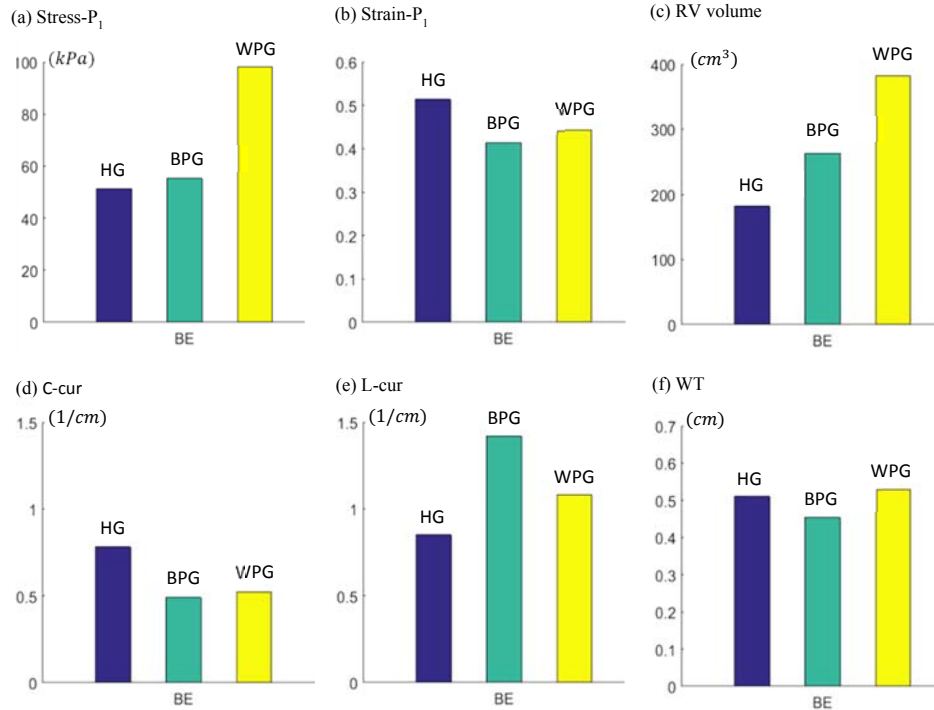
Figure 9.8 Bar plots comparing average Stress-P1, Strain-P1, RV volume, C-cur, L-cur and WT values from Healthy Group (HG), Better-outcome Patient Group (BPG) and Worse-outcome Patient Group (WPG) at Begin-Ejection(BE). Blue: HG; Green: BPG; Yellow: WPG.

9.4 Prediction by using Median as Threshold

For each parameter, median of patient-average values from 16 patients was used as threshold value for prediction. For example, the median of RV WT at begin of ejection was 0.475 cm and the comparison analyses (Table 9.5) showed that average RV WT of WPG at begin of ejection was higher than that from BPG. Then, if a patient has mean RV WT at begin of ejection lower than the median (0.475 cm), the patient would be predicted to belong to BPG, and if mean RV WT was higher than the median, the patient would be predicted to belong to WPG. If the prediction matches the actual group assignment, the prediction was considered as "True". Otherwise, the prediction was considered as "False". The results of this analyses were shown in Table 9.7. Begin-ejection results and begin-filling results were given in table 9.7.1 and table 9.7.2

96

respectively. At begin of ejection, Stress-P_1 and RV volume were found to have the highest prediction accuracy (68.8%), other parameters showed lower accuracy. At begin of filling, Strain-P_1 was found to have highest accuracy (81.3%) in prediction.

Patient	WT	C-cur	L-cur	RV EDV	Stress-P_1	Strain-P_1
P1	0.39 T	0.47 F	1.24 T	406.9 F	56.9 T	0.29 T
P2	0.47 T	0.43 T	0.96 F	323.3 T	82.4 F	0.44 F
P3	0.48 F	0.50 F	1.20 F	204.0 T	61.9 T	0.48 F
P4	0.42 T	0.53 F	1.84 T	193.7 T	33.5 T	0.46 F
P5	0.51 F	0.53 F	1.85 T	188.3 T	42.0 T	0.4 T
P6	0.34 F	0.39 F	0.77 T	328.8 F	65.3 F	0.43 F
P7	0.65 T	0.37 F	1.01 T	408.8 T	41.0 F	0.33 F
P8	0.49 T	0.54 T	1.54 F	364.6 T	64.1 F	0.36 F
P9	0.48 T	0.42 F	0.91 T	385.1 T	172.1 T	0.66 T
P10	0.41 F	1.34 T	1.32 F	204.2 F	82.9 T	0.49 T
P11	0.80 T	0.36 F	0.59 T	665.1 T	82.4 T	0.23 F
P12	0.71 T	0.44 F	0.72 T	334.8 T	83.1 T	0.42 F
P13	0.45 F	0.46 T	0.97 T	277.2 F	191.7 T	0.66 T
P14	0.43 F	0.65 T	1.60 F	365.0 T	65.4 F	0.44 T
P15	0.46 F	0.44 F	1.23 F	299.0 F	154.3 T	0.51 T
P16	0.59 T	0.33 F	1.25 F	571.1 T	76.2 T	0.34 F
Median	*0.475*	*0.45*	*1.215*	*331.8*	*70.8*	*0.435*
True Prediction	56.3%	31.3%	56.3%	68.8%	68.8%	43.8%
CI	(32.0%, 80.6%)	(8.6%, 54.0%)	(32.0%, 80.6%)	(46.1%, 91.5%)	(46.1%, 91.5%)	(19.5%, 68.1%)

Table 9.7.1 True or False prediction results using the median parameter values at beginning of ejection to predict patient's group. The median values were used as the thresholds for group assignments. F and T mean False and True respectively. CI means confidence interval.

Patient	WT	C-cur	L-cur	RV ESV	Stress-P_1	Strain-P_1
P1	0.43 T	0.60 F	1.32 T	254.50 F	2.91 T	0.03 T
P2	0.54 F	0.52 T	0.90 F	177.80 T	9.56 F	0.03 T
P3	0.54 F	0.68 F	1.54 T	104.30 T	2.31 T	0.02 T
P4	0.47 T	0.69 F	2.31 T	105.10 T	2.16 T	0.02 T
P5	0.53 T	0.67 F	1.75 T	108.30 T	2.04 T	0.03 T
P6	0.38 F	0.48 F	0.75 T	196.00 T	9.03 T	0.14 T
P7	0.71 T	0.45 T	0.84 T	254.80 T	1.55 F	0.03 F
P8	0.54 T	0.64 F	1.37 F	239.50 T	3.65 F	0.05 T
P9	0.52 F	0.54 F	0.89 T	184.60 T	7.88 T	0.09 T
P10	0.46 F	1.46 F	1.41 F	121.30 F	13.23 T	0.14 T
P11	0.87 T	0.40 T	0.65 T	464.00 T	15.83 T	0.04 T
P12	0.85 T	0.57 T	0.82 T	170.80 F	2.64 F	0.01F
P13	0.50 F	0.54 F	0.87 T	151.30 F	17.80 T	0.16 T
P14	0.53 T	0.90 F	1.49 F	178.00 F	3.23 F	0.01 F
P15	0.47 F	0.54 F	1.23 T	186.00 T	15.03 T	0.14 T
P16	0.66 T	0.41 T	1.32 F	371.30 T	8.31 T	0.04 T
Median	*0.53*	*0.555*	*1.275*	*181.3*	*5.765*	*0.035*
True Prediction	56.3%	31.3%	68.8%	68.8%	68.8%	81.3%
CI	(32.0%, 80.6%)	(8.6%, 54.0%)	(46.1%, 91.5%)	(46.1%, 91.5%)	(46.1%, 91.5%)	(62.2%, 100%)

Table 9.7.2 True or False prediction results using the median parameter values at beginning of filling to predict patient's group. The median values were used as the thresholds for group assignments. F and T mean False and True respectively. CI means confidence interval.

9.5 Logistic Regression Analysis with 2-fold Cross-validation Procedure

The logistic regression method with 2-fold cross-validation procedure was used to search the best predictor for patient's group category from the combinations of the 6 potential parameters including WT, C-cur, L-cur, RV volume, Stress-P_1 and Strain-P_1.

For all 63 possible combinations of the 6 parameters, the logistic regression models were constructed and their prediction accuracy for patient's group category were calculated. In this analysis, we followed the group assignment given in section 9.3 where BPG consisted of 5 patients

with positive RV EF change after PVR and WPG contained 11 patients with negative RV EF change after PVR. 2-fold cross-validation procedure was adopted in prediction accuracy calculation. The logistic regression models with their prediction accuracies for patient's group category were shown in Table 9.8. Table 9.8.1 showed the results based on begin-ejection data while the results based on the data at begin of filling were given in table 9.8.2.

Table 9.8.1 & 9.8.2 showed the 6 best combinations (out of 63) of RV parameters that correctly assigned patients to their ultimate outcome group. At the beginning of ejection (Table 9.8.1), RV Stress-P_1 was the best single predictor among the 6 individual parameters with an area under the ROC curve of 0.711. The second best single predictor was RV volume with an area under the ROC curve of 0.652. The best combination of parameters included wall thickness + C-cur + Stress-P_1 with an area under the ROC curve of 0.677. At the beginning of filling (Table 9.8.2), RV Stress-P_1 was also the best single predictor among the 6 individual parameters with an area under the ROC curve of 0.713. The second best single predictor was RV volume again with an area under the ROC curve of 0.653. The best combination of parameters was still wall thickness + C-cur + Stress-P_1 with an area under the ROC curve of 0.679. Among all combinations of parameters, stress was the best predictor based on sensitivity and specificity.

Logistical Model	Cutoff Prob.	Sensitivity	Specificity	Sensitivity + Specificity	AUC	Mean AUC	95% CI	Rank
Stress-P_1	0.34	0.68	0.77	1.45	0.711	0.711	0.708-0.718	1
WT+C-cur +Stress-P_1	0.33	0.70	0.62	1.32	0.647	0.677	0.673-0.692	2
Vol+Strain-P_1	0.62	0.48	0.82	1.30	0.614	0.656	0.653-0.663	3
WT+C-cur +Vol+Strain-P_1	0.01	0.84	0.50	1.34	0.662	0.656	0.653-0.661	4
WT+C-cur +Vol+Stress-P_1	0.71	0.69	0.66	1.35	0.660	0.652	0.645-0.656	5
Vol	0.36	0.54	0.81	1.35	0.646	0.652	0.648-0.658	6
L-cur	0.34	0.46	0.68	1.14	0.561	0.592	0.587-0.614	22
WT	0.25	0.82	0.37	1.19	0.534	0.529	0.520-0.533	43
C-cur	0.25	0.85	0.29	1.14	0.493	0.479	0.475-0.495	57
Strain-P_1	0.07	0.98	0.07	1.05	0.393	0.380	0.371-0.386	63

Table 9.8.1 Prediction sensitivity, specificity, area under the curve values, and right ventricular parameters for outcome group prediction by logistic regression method. Data at beginning of ejection was used in this analysis.

Logistical Model	Cutoff Prob.	Sensitivity	Specificity	Sensitivity + Specificity	AUC	Mean AUC	95% CI	Rank
Stress-P_1	0.37	0.63	0.84	1.47	0.704	0.713	0.708-0.725	1
WT+C-cur +Stress-P_1	0.44	0.74	0.73	1.47	0.736	0.679	0.676-0.694	2
WT+C-cur +Vol+Strain-P_1	0.01	0.85	0.51	1.36	0.664	0.654	0.647-0.661	3
Vol	0.40	0.56	0.81	1.37	0.641	0.653	0.634-0.657	4
WT+C-cur +Vol+Stress-P_1	0.58	0.61	0.67	1.28	0.650	0.653	0.644-0.661	5
Vol+ Strain-P_1	0.41	0.63	0.76	1.39	0.679	0.651	0.645-0.654	6
L-cur	0.25	0.74	0.54	1.28	0.662	0.594	0.588-0.604	22
WT	0.22	0.88	0.33	1.21	0.534	0.523	0.515-0.526	45
C-cur	0.25	0.88	0.25	1.13	0.461	0.476	0.472-0.479	58
Strain-P_1	0.22	0.92	0.13	1.05	0.388	0.384	0.383-0.389	63

Table 9.8.2 Prediction sensitivity, specificity, area under the curve values, and right ventricular parameters for outcome group prediction by logistic regression method. Data at beginning of filling was used in this analysis.

9.6 Conclusion

In this chapter, twenty-two 1G structure-only FE models were constructed for selected healthy volunteers and the patients with rTOF. Mechanical parameters including stress and strain were obtained from numerical simulations and used in relevant analyses.

Correlation analyses showed that Stress-P_1 was significantly correlated with ΔRVEF while no significant correlation was found between Strain-P_1 and ΔRVEF. Thus, stress might be a potential predictor for RV function after PVR surgeries.

Group comparison indicated that Stress-P_1 had a large difference between BPG and WPG, however the p-value was near the borderline (0.05). Therefore, we compared HG to the two patient groups, and we found that stress of BPG was close to that of HG (p-value was larger than 0.5)

while stress of WPG was significantly different from that of HG (p-value was smaller than 0.03). With the help of HG, Stress-P_1 has the potential to differentiate BPG from WPG.

In the prediction using median as threshold, Stress-P_1 held the highest prediction accuracy. The similar result was also found in the prediction using logistical regression, Stress-P_1 was the best predictor for PVR outcome (improved or non-improved).

In sum, mechanical stress might be considered as another good indicator for PVR surgeries outcome.

10. Mechanical and Geometrical Analysis Using 3D RV Models with Two Zero-load Geometries

In this section, we focused on model improvement. Based on 1G models, we introduced two zero-load geometries in our numerical modeling which was named as 2G models. 16 patients used in Chapter 9 were also used in this chapter for the construction of 3D RV/LV models with two zero-load geometries (2G models). The basic information of these patients can be found in table 9.1. All the patients were also divided into two groups following the grouping rule used in chapter 9.

Methods introduced in Chapter 5 were used to obtain two different zero-load geometries, one was for simulation of diastole and the other was for systole. Shrinkage rate for diastolic and systolic zero-load geometries were chosen around 2% and 15% respectively. Results of mechanical and geometrical parameters were obtained from new models (2G models) for analysis. Comparative analyses were performed between 1G models and 2G models to see if there exists any difference between the two kinds of models.

10.1 Agreement between numerical results and CMR data

One 2G model was selected as the representative to show the agreement between numerical RV volume results and CMR-based volume data.

In the representative 2G model, for diastolic zero-load geometry, the shrinkage ratio for inner contours of ventricles was 4% and the shrinkage ratio for outer contours was obtained according to mass conservation of ventricles. The shrinkage ratio for z direction (longitudinal direction) was 0% which means no change happened in longitudinal direction due to the material properties of ventricular tissue. For systolic zero-load geometry, the shrinkage ratio for ventricular inner contours and longitudinal direction were set as 7% and 10% respectively. Zero-load

geometry for diastole is larger than that for systole since the sarcomere length shortens during active construction from end of diastole to begin of systole. In corresponding 1G model, the shrinkage ratio for inner contours of ventricles was 4% and the shrinkage ratio for longitudinal direction was 0%.

In 2G models, we also adopted anisotropic Mooney-Rivlin model introduced in chapter 5 as the material model of ventricular tissues. For patch, scar and artery, modified isotropic Mooney-Rivlin model (chapter 5) was used as their material models. Baseline of parameter values for each material were same with those used in chapter 9 (see details in chapter 9). For ventricular tissues, time-dependent parameter values (c_1(t), D_1(t), K_1(t)) were determined by fitting the CMR-measured RV volume data to simulate active contraction and expansion of myocardium.

Figure 10.1 showed the stress-stretch curves and parameter values of ventricular tissues for the representative model at begin of ejection, end of ejection, begin of filling and end of filling. Figure 10.1 also showed and compared the numerical RV volume data of the representative model obtained from simulations with MRI-based data. In this representative model, good agreement between computational and CMR-measured volume data was found (error < 2%).
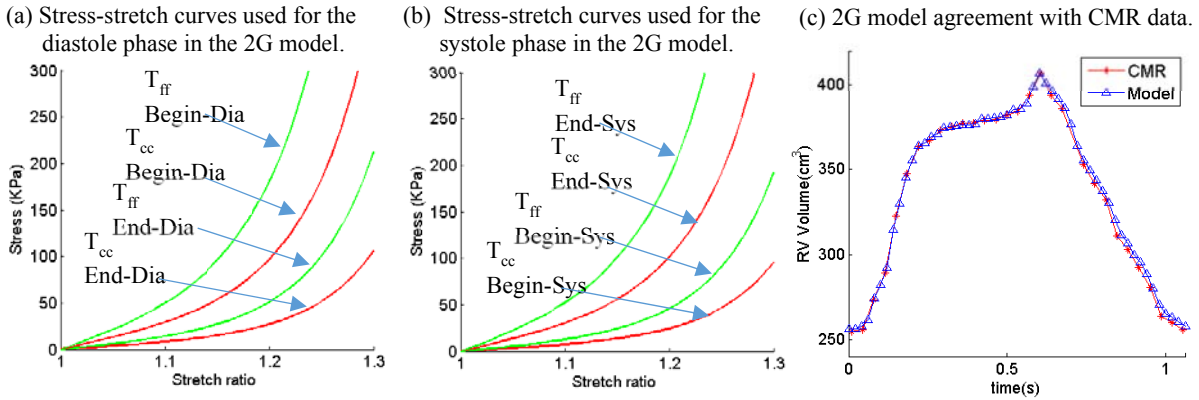
Figure 10.1. Material Stress-Stretch curves used for the new 2G and the numerical RV volume results. (a) stress-stretch curves used for the diastole phase in the 2G model; (b) stress-stretch curves used for the systole phase in the 2G model. T_{ff}: stress in fiber direction; T_{cc}: stress in cross-fiber direction. (c) 2G model agreement with CMR data.

10.2 Comparison between 1G and 2G models

In 1G models, two isovolumic phases were combined into filling and ejection phases. In filling phase, RV volume and pressure increase from their minima to maxima. In ejection phase, RV volume and pressure decrease from their maxima to minima. End-filling status is same with begin-ejection status, and end-ejection status is same with begin-filling status.

In 2G models, two isovolumic phases were omitted from simulations and we only simulated the movement during diastole and systole. In diastole, RV volume increases from its minima to maxima when RV pressure increases from minima to end-diastole pressure which is smaller than maxima and will increase to maxima during diastolic isovolumic phase. In systole, RV volume decreases from its maxima to minima when RV pressure decreases from maxima to end-systole pressure which is larger than minima and will decrease to minima during systolic isovolumic phase. Thus, end-filling status is different with begin-ejection status and end-ejection status is also different with begin-filling status.

105

For the 1G model, results at begin-filling (BF) and begin-ejection (BE) corresponding to minimal and maximal pressure (or RV volume) were obtained for analysis. For the 2G model, results at begin-filling (BF), end-filling (EF), begin-ejection (BE), and end-ejection (EE) were obtained for analysis. The traditional begin-systole, end-systole, end-diastole, and begin-diastole conditions correspond to our begin-ejection, end-ejection, end-filling, and begin-filling, respectively.

10.2.1 Stress Comparison

Table 10.1 summarized the mean stress values of the 16 patients from 1G and 2G models. According to the total average values in table 10.1, the mean stress of 1G models was 84.70kPa at the beginning of ejection and 7.32 kPa at the beginning of filling. For 2G models, the mean stress at begin of ejection 108.41 kPa which was 28% higher than that from 1G models, and the mean stress at begin of filling was 7.17 kPa which was similar with the mean stress of 1G models (2% difference).

	Old Model		New Model			
Patient	1G-BF (kPa)	1G-BE (kPa)	2G-BF (kPa)	2G-EF (kPa)	2G-BE (kPa)	2G-EE (kPa)
1	2.914	56.92	4.19	29.32	76.16	27.41
2	9.034	65.35	8.66	43.46	109.90	29.65
3	1.551	41.03	2.62	21.21	58.93	17.46
4	3.655	64.06	5.53	33.56	89.91	30.62
5	9.564	82.41	9.58	55.91	127.76	30.45
6	2.314	61.89	2.59	34.02	92.17	16.02
7	2.160	33.45	2.09	17.13	46.03	9.82
8	2.042	41.97	2.25	21.68	62.14	13.19
9	7.880	172.05	7.43	57.61	161.20	35.88
10	13.229	82.90	13.19	52.42	121.48	36.46
11	15.832	82.42	16.63	50.78	109.86	46.13
12	2.638	83.11	2.86	56.68	146.04	25.21
13	17.799	191.73	10.30	59.89	151.85	33.71
14	3.232	65.36	4.75	34.79	89.98	24.25
15	15.027	154.31	13.90	77.69	182.61	53.04
16	8.307	76.18	8.17	43.40	108.53	32.93
Ave	**7.323**	**84.70**	**7.17**	**43.10**	**108.41**	**28.89**

Table 10.1.   Comparison of average stress results from 1G and 2G models. BF: Begin-Filling; BE: Begin-Ejection; EF: End-Filling; EE: End-Ejection.

Different from 1G models, the 2G models can provide end-ejection and end-filling stress conditions which were not available in 1G models. The right ventricles had the same volume at end of filling and begin of ejection, however the average value of RV begin-ejection stress (peak-systole stress) was 151.5% higher than the average value of RV end-filling stress (108.41 kPa vs. 43.10 kPa). Similarly, the right ventricles had the same volume at end of ejection and begin of filling, but the average value of RV end-ejection stress was 300% higher than the average value of RV begin-filling stress (28.98 kPa vs. 7.17 kPa).

The representative model chosen in section 10.1 was also used here to show stress distribution plots. A cut surface was selected to show the stress plots on the inner surface of RV. Figure 10.2 showed the stress plots from the 1G and 2G models at the time when RV volume reached its maxima and minima. Large difference was found between 1G and 2G models due to these plots.

(a) 1G model, begin-ejection.   (b) 2G model, begin-ejection.   (c) 2G model, end-filling.

Avg = 56.92 kPa   Avg = 76.16 kPa   Avg = 29.33 kPa

(d) 1G model, begin-filling.   (e) 2G model, end-ejection.   (f) 2G model, begin-filling.

Avg = 2.91 kPa   Avg = 27.41 kPa   Avg = 4.19 kPa

Min   Universal Scale   Max
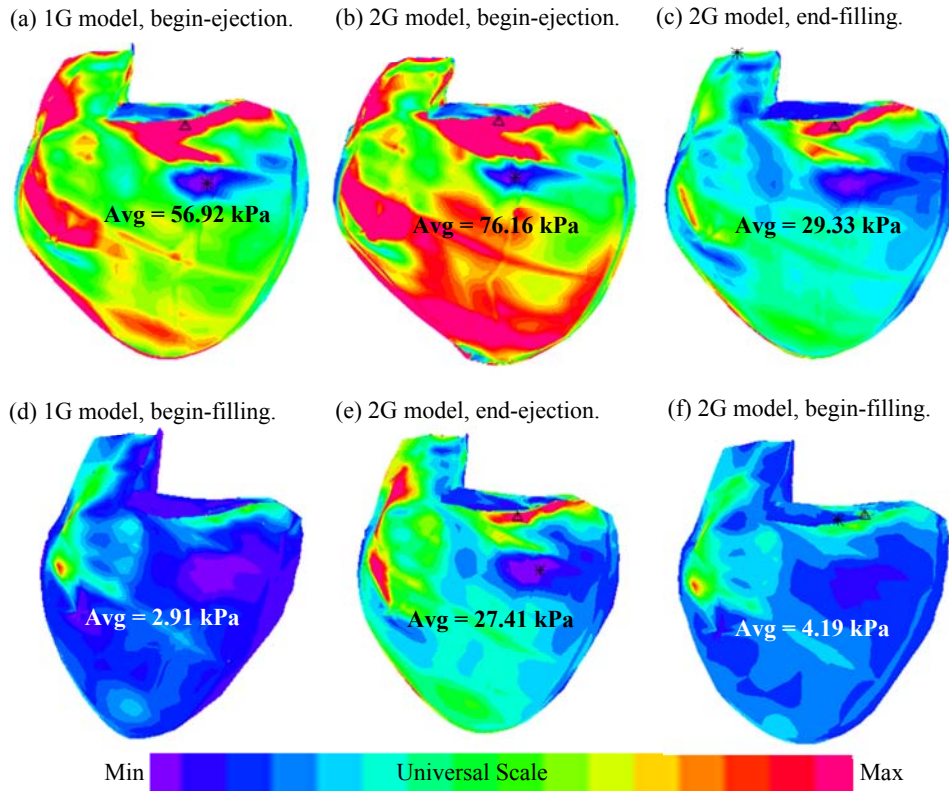
Figure 10.2   Stress plots from 1G and 2G models showing large differences. (a) 1G model, begin-systole; (b) 2G model, begin-systole; (c) 2G model, end-diastole; (d) 1G model, begin-diastole; (e) 2G model, end-systole; (f) 2G model, begin-diastole. Note: (a)-(c) all with maximum RV volume; (d)-(f) all with minimum RV volume.

10.2.2 Strain Comparison

Table 10.2 summarized the mean strain values of the 16 patients from 1G and 2G models.

According to the total average values in table 10.2, the mean strain of 1G models was 0.434 at the beginning of ejection and 0.062 at the beginning of filling. For 2G models, the mean strain at begin of ejection 0.606 which was 39.6% higher than that from 1G models, and the mean strain at begin of filling was 0.048 which was 23% lower than that from 1G models.

Patient	1G Model		2G Model			
	1G-BF	1G-BE	2G-BF	2G-EF	2G-BE	2G-EE
1	0.028	0.289	0.024	0.295	0.441	0.143
2	0.144	0.425	0.115	0.495	0.698	0.262
3	0.029	0.327	0.042	0.330	0.498	0.159
4	0.053	0.356	0.087	0.357	0.534	0.219
5	0.033	0.444	0.036	0.496	0.653	0.124
6	0.017	0.484	0.012	0.480	0.663	0.109
7	0.016	0.463	0.011	0.449	0.658	0.100
8	0.031	0.401	0.016	0.367	0.565	0.119
9	0.091	0.662	0.056	0.588	0.783	0.212
10	0.137	0.489	0.136	0.494	0.649	0.273
11	0.038	0.230	0.040	0.231	0.373	0.153
12	0.010	0.416	0.009	0.510	0.672	0.091
13	0.160	0.658	0.030	0.500	0.743	0.159
14	0.012	0.442	0.017	0.440	0.621	0.101
15	0.142	0.515	0.110	0.463	0.657	0.250
16	0.044	0.335	0.024	0.304	0.481	0.142
Ave	**0.062**	**0.434**	**0.048**	**0.425**	**0.606**	**0.164**

Table 10.2.   Comparison of average strain results from 1G and 2G models.

Again, the 2G models can provide end-ejection and end-filling strain conditions which were not available in 1G models. The right ventricles had the same volume at end of filling and begin of ejection, however the average value of RV begin-ejection strain (peak-systole strain) was 42.6% higher than the average value of RV end-filling strain (0.606 vs. 0.425). Similarly, the right ventricles had the same volume at end of ejection and begin of filling, but the average value of RV end-ejection strain was 242% higher than the average value of RV begin-filling strain (0.164 vs. 0.048).

Figure 10.3 showed the strain plots from the 1G and 2G models at the time when RV volume reached its maxima and minima. Large difference was found between 1G and 2G models based on these plots.
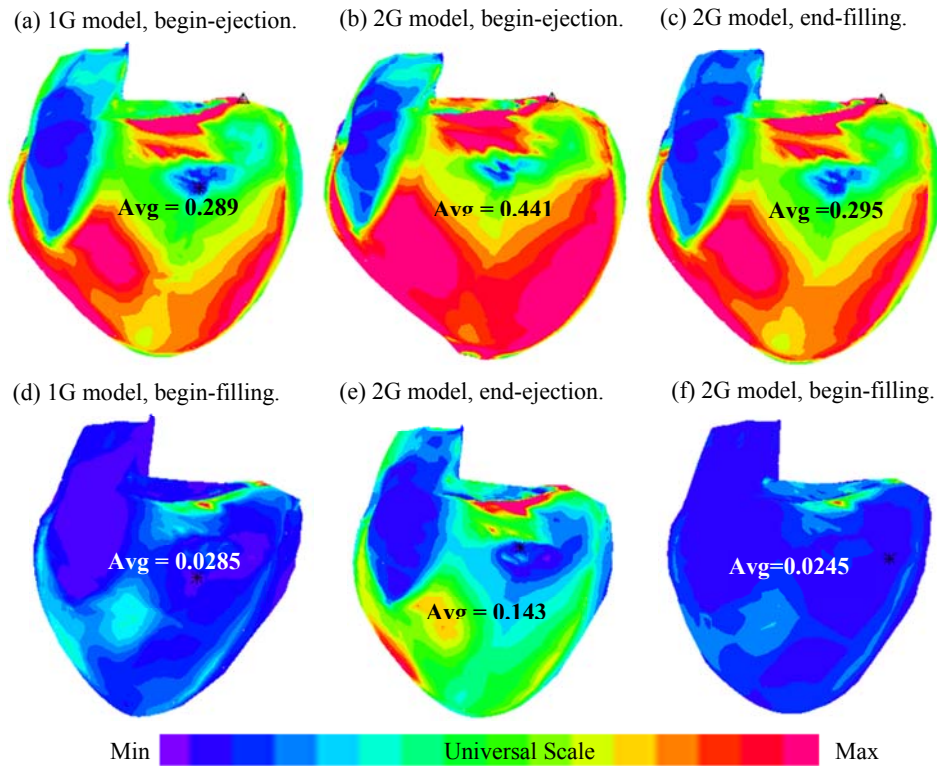
Figure 10.3 Strain plots from 1G and 2G models showing large differences. (a) 1G model, begin-systole; (b) 2G model, begin-systole; (c) 2G model, end-diastole; (d) 1G model, begin-diastole; (e) 2G model, end-systole; (f) 2G model, begin-diastole. Note: (a)-(c) all with maximum RV volume; (d)-(f) all with minimum RV volume.

Figure 10.4 gives plots of average stress/strain variations in a cardiac cycle from 1G and 2G models to show the differences of stress/strain variations in one cardiac cycle between two different models. In 2G models, because isovolumic phases were considered, end-filling was not assumed to be same with begin-ejection and end-ejection was not assumed to be same with begin-filling. Then there were jumps found at transition from end-filling to begin-ejection and from end-

ejection to begin-filling in the curves of 2G models but these phenomena were not found in 1G models.

(a) Average stress from the old 1G model.

(b) Average stress from the new 2G model.

(c) Average strain from the 1G model.

(d) Average strain from the 2G model.
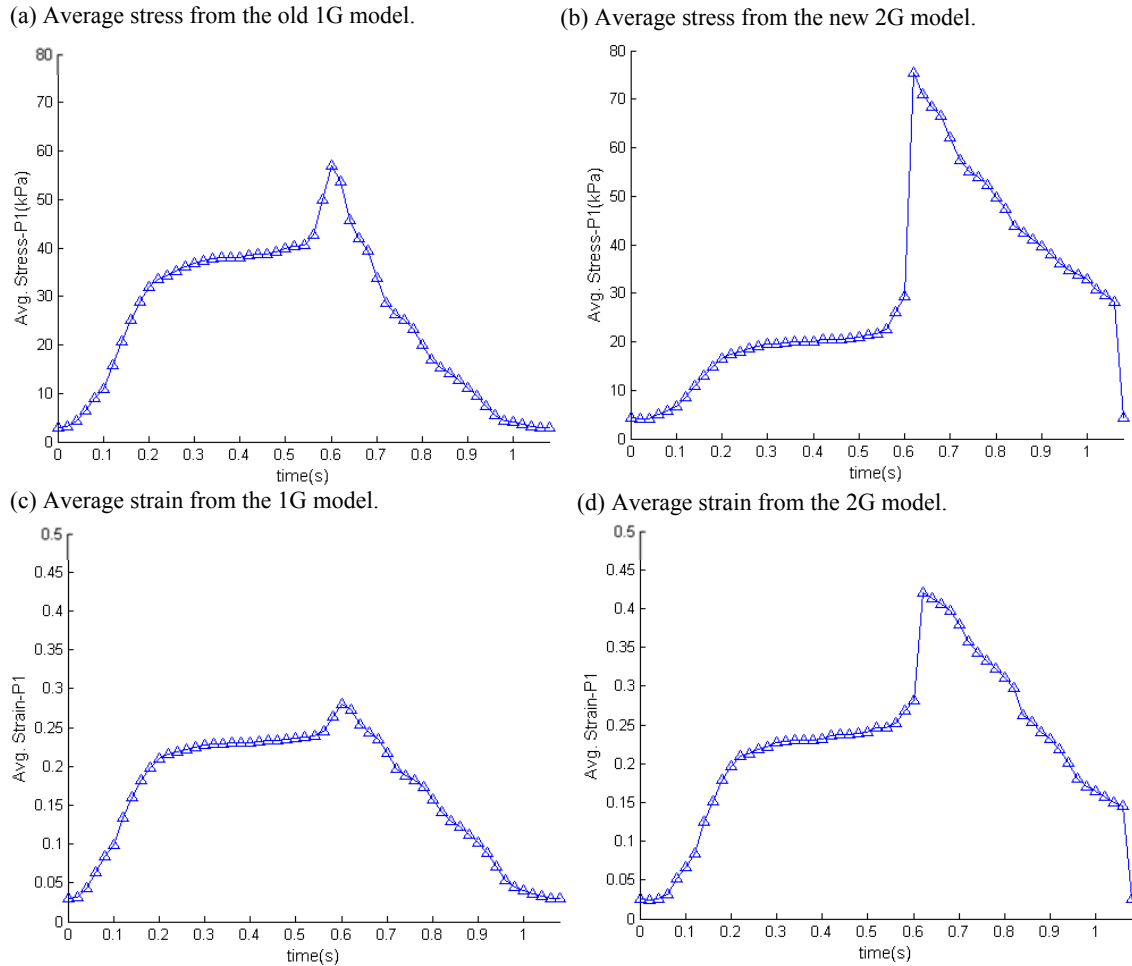
Figure 10.4 Stress and strain variations (average value on the inner RV surface) in one cardiac cycle from a TOF patient showing the difference between the two models. Sudden increase at the end of diastole and sudden decrease at the end of systole reflected our omission of the two isovolumic phases. (a) Average stress from the old 1G model; (b) average stress from the new 2G model; (c) Average strain from the 1G model; (d) average strain from the 2G model.

10.2.3 Geometrical parameters comparison

Geometrical analysis was performed on the results obtained from the simulations of 1G and 2G models. In isovolumic contraction and relaxation, ventricular volumes keep unchanged but

111

small shape changes are possible. Therefore, the values of geometrical parameters (such as curvature and wall thickness) might change during isovolumic phases and the 2G models can provide the results of the geometrical parameters at end of filling (or end of ejection) which might be different with the begin-ejection (or begin-filling) values and lack in the 1G models.

The computational results of RV circumferential curvature, longitudinal curvature and wall thickness from 1G and 2G models were summarized in Table 10.3.

The average values of RV wall thickness at begin of filling from 1G and 2G models were 0.575 cm and 0.564 cm, respectively (2% difference). The begin-ejection average RV wall thickness from 1G and 2G models were 0.491 cm and 0.505 cm, respectively (3% difference).

For the circumferential curvature, the average begin-filling values from 1G and 2G models were 0.638 1/cm and 0.630 1/cm, respectively (1% difference). The average begin-ejection values from two kind of models were 0.524 1/cm and 0.514 1/cm, respectively (2% difference).

For the longitudinal curvature, the average begin-filling value from the 1G models was very close to the average begin-filling value from the 2G model (1.216 1/cm vs 1.193 1/cm). The average begin-ejection value from 1G models was 1.186 1/cm which was close to the average end-ejection value (1.155 1/cm) from the 2G models. However, the average begin-ejection and end-ejection longitudinal curvatures from 2G models were 1.263 1/cm and 1.389 1/cm, respectively. The higher longitudinal curvatures in the systole phase were due to the larger shrinkage in the longitudinal direction linked to our selected fiber orientations.

	1G Model		2G Model			
Patient	1G-BF	1G-BE	2G-BF	2G-EF	2G-BE	2G-EE
RV Wall Thickness (cm)						
16P	0.564	0.505	0.575	0.519	0.491	0.525
Circumferential Curvature (1/cm)						
16P	0.630	0.514	0.638	0.516	0.524	0.618
Longitudinal Curvature (1/cm)						
16P	1.216	1.186	1.193	1.155	1.263	1.389

Table 10.3 Comparison of RV wall thickness and curvatures results from the 1G and 2G models.

Bar plots were also used here to more straightforwardly show the differences of the mean parameter values between 1G and 2G models (Figure 10.5). In the plots, at the time when RV volume reached minimal, blue was used for begin-filing time of 1G models, green and yellow were used for begin-filling and end-ejection time of 2G models respectively. At the time when RV volume reached maximal, blue was used for begin-ejection time of 1G models, green and yellow were used for end-filling and begin-ejection time of 2G models respectively. All the findings from section 10.2.1 to section 10.2.3 could be also found in the figure.

10.3 Conclusion

Sixteen 2G models were constructed in this chapter and compared to the corresponding 1G models built in Chapter 9. The main difference between 1G and 2G was that 2G models can provide the end-filling and end-ejection information that lacked in 1G models, which was also the improvement of 2G models compared to 1G models. Furthermore, comparative analyses between 1G and 2G models showed that at begin of filling 2G models had similar morphological and mechanical properties with 1G models, but at begin of ejection 2G models had similar morphological properties and different mechanical properties with 1G models.
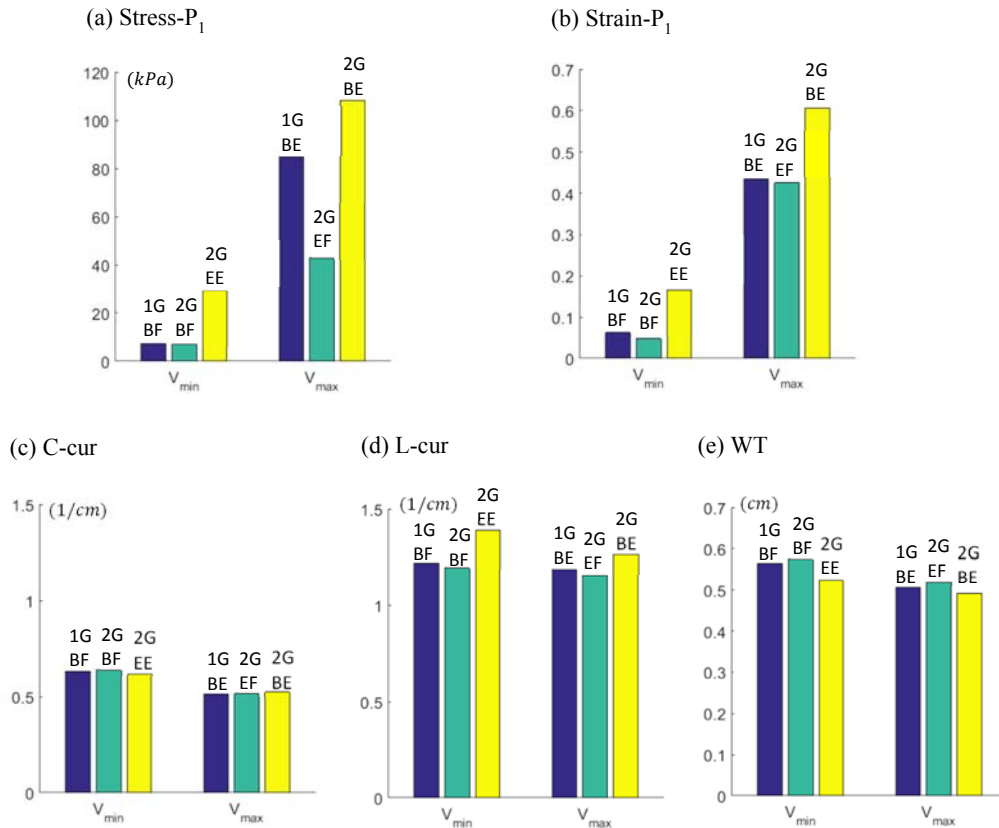
Figure 10.5 Bar plots comparing average Stress-P₁, Strain-P₁, C-cur, L-cur and WT values from 1G models and 2G models at the time when RV volume reaches maximal and minimal. At min-volume time (Vmin): Blue: Begin-filling of 1G; Green: Begin-filling of 2G; Yellow: End-ejection of 2G. At max-volume time (Vmax): Blue: Begin-ejection of 1G; Green: End-filling of 2G; Yellow: Begin-ejection of 2G.

11. Fluid-Structure-Interaction Model

11.1 Introduction

Blood flow in right ventricle was assumed to be laminar, Newtonian, viscous and incompressible. The Navior-Stokes equations with ALE formulation were used as the governing equations. Pressure conditions were prescribed at the tricuspid (inlet) and pulmonary (outlet) valves. To simplify the computational model, the cardiac cycle was split into two phases: (1) The filling phase (diastole) when blood flows into the RV, the inlet was open and the outlet was closed; (2) The ejection phase (systole) when blood flows out from the RV, the inlet was closed and the outlet was open. When the inlet or outlet was closed, flow velocity was set to zero and pressure was left unspecified. When the inlet or outlet was open, flow velocity was left unspecified and pressure was set to RV pressure data. No-slip boundary conditions and natural force boundary conditions were specified at all interfaces to couple fluid and structure models together.

In this chapter, we still focused on model improvement. By introducing fluid part and fluid-solid-interaction in previous 1G model, FSI models were constructed. Two patients with repaired TOF were chosen for FSI modeling. One patient was chosen from better-outcome patient group with 1.4% RVEF change from pre- to post-RVR and the other patient was chosen from worse-outcome patient group with -15.2% RVEF change from pre- to post-PVR. Flow velocity, pressure and shear stress were obtained from fluid parts and compared between two patients. Furthermore, the results of structure parts from FSI models were compared with structure-only models to see if FSI models can bring any change in 1G models. Flow results of BPG patient were compared to those of WPG patient to see if there exists any difference in flow parameters between BPG and WPG, and then the difference indicates the potential to predict PVR outcome.

11.2 Flow Results

FSI models can provide us with flow parameters such as velocity and pressure in RV. Also, the effect of flow on RV inner surface could be shown as flow shear stress. In this section, the patient with worse outcome was used to exhibit numerical flow results. 3D solutions have complex behaviors, so it is common to use a selected cut-surface to show results. Figure 11.1 shows the position of the selected cut surface and the different views of RV inner surface through the cut surfaces. At some selected time points, velocity and pressure distributions on the cut surface and flow shear stress distributions on RV inner surface were plotted for the selected exhibition patient.

(a) Location of cut surface   (b) RV inner surface view, LV side   (c) RV inner surface view, RV side
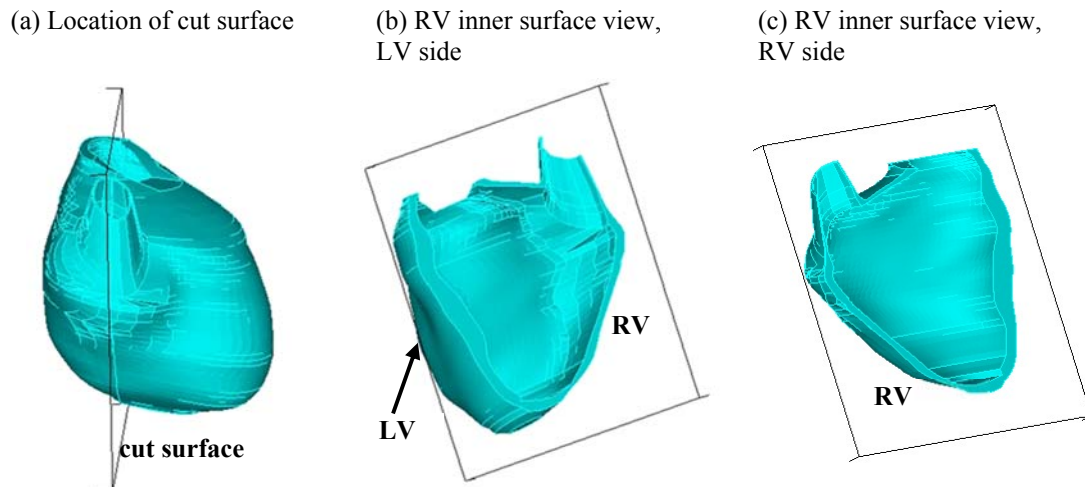
Figure 11.1 Location of cut surface with left-side and right-side views for RV inner surface.

11.2.1 Flow velocity

Figure 11.2 gave the velocity distributions on the selected cut surfaces at some time points covering a whole cardiac cycle. Figure 11.2 (a)-(d) used one uniform scale and showed velocity distributions at different time points in filling phase, while figure 11.2 (e)-(h) used another uniform scale and showed velocity distributions at different time points in ejection phase.

During the filling phase, blood enters the right ventricle through the tricuspid valve, the pulmonary valve is closed, and the right ventricle expands at the same time. Fig. 11.2 (a) showed the velocity distribution at begin of filling. As the pressure at the tricuspid valve increased,

116

magnitude of velocity increased and decreased time to time which depended on the pressure gradient at the inlet. Fig. 11.2 (b) and (c) showed the velocity distributions at two time points during filling phase. Fig. 11.2 (d) gave the velocity distribution at end of filling. During the ejection phase, blood was ejected out of the right ventricle through pulmonary valve due to increased stress in ventricular tissue, the tricuspid valve is closed, and meanwhile the right ventricle shrinks. Fig. 11.2 (e) showed the velocity distribution at begin of ejection. As the pressure at the pulmonary valve decreased, magnitude of velocity increased first and decreased then. Fig. 11.2 (f) and (g) showed the velocity distributions at two time points during ejection phase. Fig. 11.2 (h) gave the velocity distribution at end of ejection. During both filling and ejection phase, one vortex was observed in RV (see figure 11.2).

(a) Begin of filling, t=0.94, Max=122.5 cm/s (b) Filling continues, t=1.00, Max=408.8 cm/s (c) Filling continues, t=1.12, Max=97.42 cm/s (d) End of filling, t=1.30, Max=38.86 cm/s

(e) Begin of ejection, t=1.34, Max=34.03 cm/s (f) Ejection continues, t=1.42, Max=179.5 cm/s (g) Ejection, peak t=1.50, Max=317.2 cm/s (h) End of ejection, t=1.72, Max=64.22 cm/s
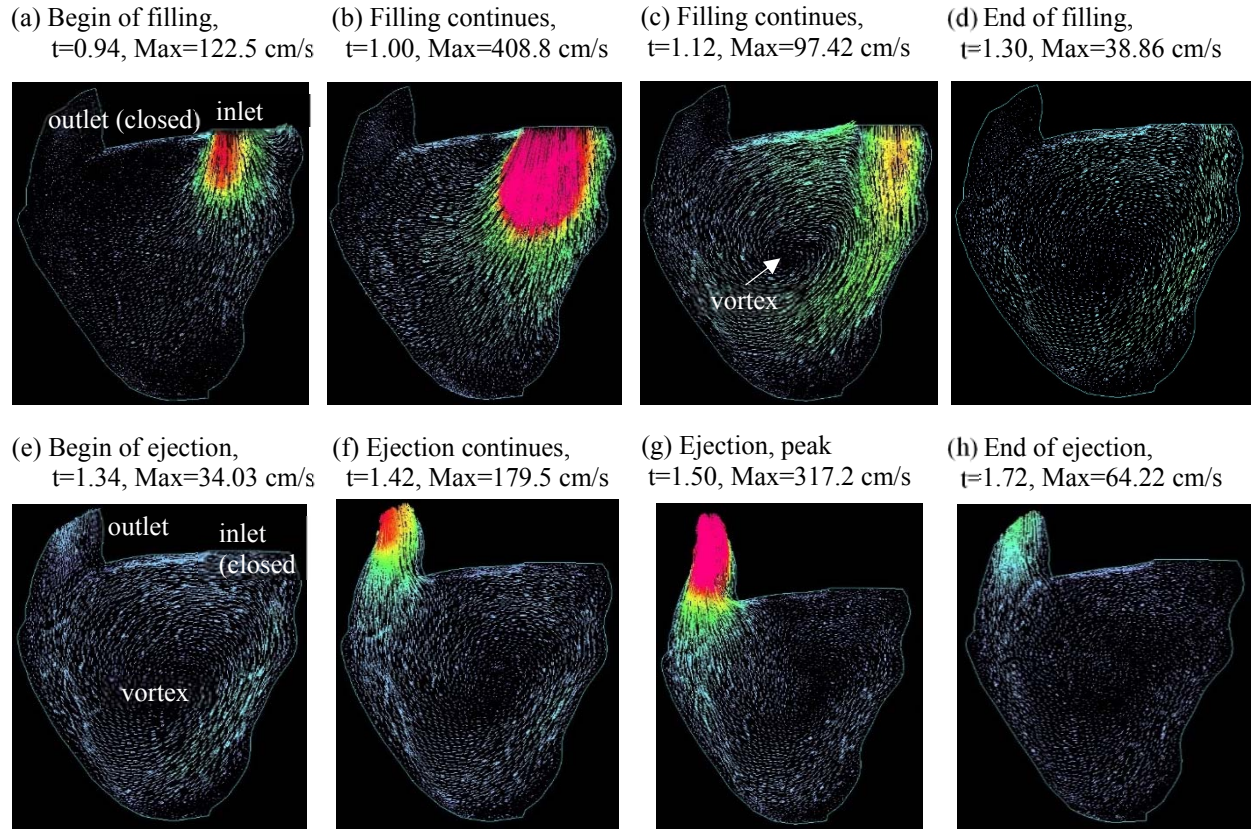
Figure 11.2 Plot of flow velocity patterns in a cardiac cycle from a WPG patient. (a) begin of filling phase, (b-c) two time points during filling, (d) end of filling phase; (e) begin of ejection phase, (f-g) two time points during ejection, (h) end of ejection phase. In (a-d), one uniform scale was used. In (e-h) another uniform scale was used.

11.2.2 Pressure Distribution

Figure 11.3 gave pressure distribution plots on the cut surface corresponding to the velocity plots given by Figure 11.2. Different scales were used for different plots to make the pressure pattern more visible.

For the patient from WPG, at begin of filling, difference of pressure in the whole RV was not very huge (ΔPressure=1.9mmHg), both maximum and minimum pressure were found near the inlet (See Fig. 11.3 (a)). During filling phase, the difference of pressure in RV increased (at t=1.00s,

118

ΔPressure=17mmHg) and then decreased (at t=1.12s, ΔPressure=3.6mmHg), the minimum pressure was always near the inlet, but maximum pressure changed from the inlet location to RV bottom (See Fig. 11.3 (b-c)). At end of filling, the pressure difference in RV became very small which was only 0.7 mmHg, maximum pressure was near the inlet and minimum pressure was near the bottom of RV (See Fig. 11.3 (d)). Then inlet closed, outlet opened and then ejection started. At begin of ejection, maximum pressure appeared near RV bottom, minimum pressure appeared at the outlet, and difference of pressure in RV was not large (ΔPressure=1.0 mmHg, see Fig. 11.3 (e)). As blood ejected from RV, pressure difference increased (at t=1.42s, ΔPressure=14.9mmHg; at t=1.50s, ΔPressure=40.7mmHg), maximum pressure always appeared at bottom of RV and minimum pressure always occurred at the location of inlet (See Fig. 11.3 (f-g)). At the end of ejection, pressure difference went down to a small value (ΔPressure=2.7mmHg, see Fig. 11.3 (h)). It should be noted that near the end of filling (Fig. 11.3 (d)&(e)), there was a lower pressure inside RV which might be caused by the velocity vortex. Maximum and minimum pressure in RV at several selected time points were summarized in Table 11.1 and compared with the pressure condition applied in numerical simulations.
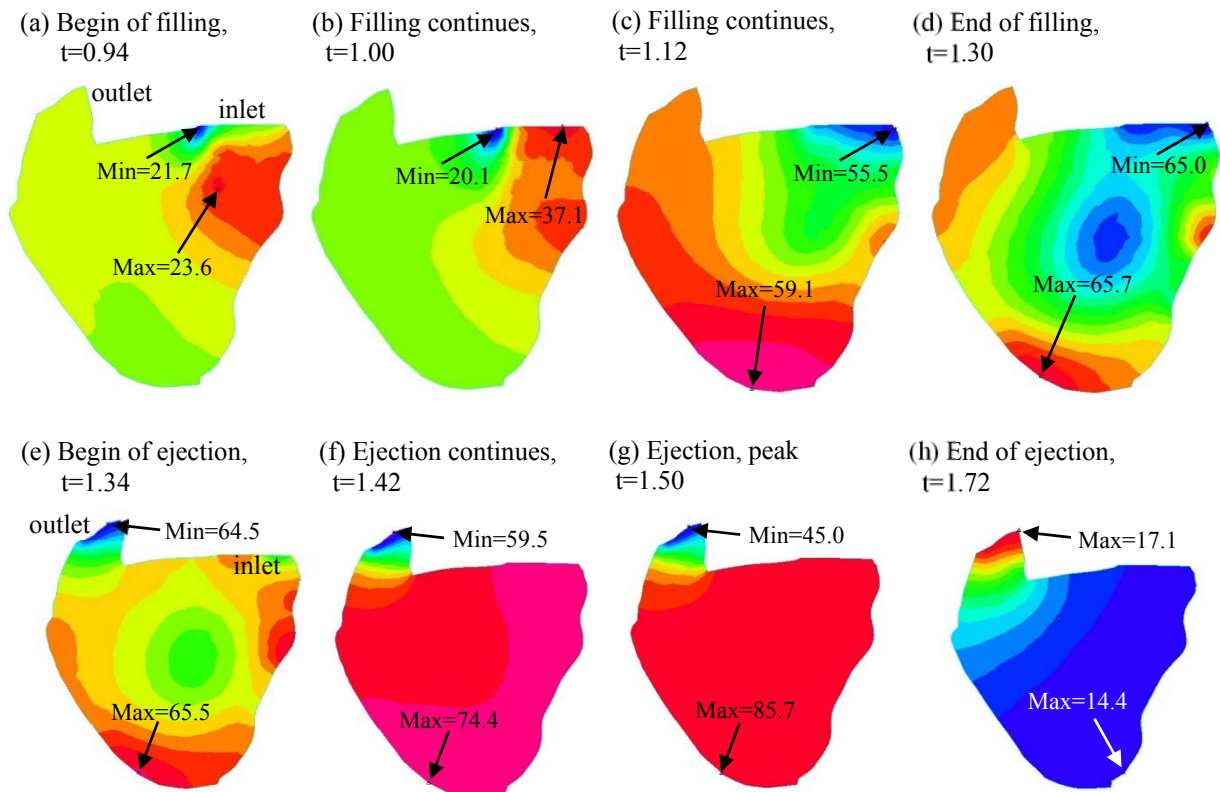
Figure 11.3 Plot of pressure patterns in a cardiac cycle from a WPG patient. (a) begin of filling phase, (b-c) two time points during filling, (d) end of filling phase; (e) begin of ejection phase, (f-g) two time points during ejection, (h) end of ejection phase. Different scales were used for different plots to make pattern visible.

Time (s)	Prescribed Pressure (mmHg)	Numerical Min Pressure (mmHg)	Numerical Max Pressure (mmHg)
0.94	22.8	21.7	23.6
1.00	37.6	20.1	37.1
1.12	55.9	55.5	59.1
1.30	65.0	65.0	65.7
1.34	64.4	64.5	65.5
1.42	58.4	59.5	74.4
1.50	42.0	45.0	85.7
1.72	17.0	14.4	17.1

Table 11.1 Maximum and minimum pressure in RV obtained from the FSI model at selected time points comparing with the pressure condition applied in numerical simulations. Note, we simulated two cardiac periods, and the second period, where numerical results were more stable, were used to exhibit results. Begin of filling: t=0.94s; end of filling: t=1.30s; begin of ejection: t=1.34s; end of ejection: t=1.72s.

11.2.3 Flow Maximum Shear Stress

Shear stress reflects the influence of flow on RV inner surface, which will be useful for tissue engineering when local flow environment is needed, such as patch design and tissue regeneration technique. Figure 11.4 gave the flow maximum shear stress (FMSS) of the WPG patient on RV inner surface at begin of filling and ejection. At each time point, FMSS distribution were given in two different views (RV-side view and LV-side view). At begin of filling, larger FMSS was found on LV-side inner surface and bottom (see Fig. 11.4 (a-b)). At begin of ejection, larger FMSS was found on the area near pulmonary and tricuspid valve (see Fig. 11.4 (c-d)).

(a) Begin of filling, RV-side view   (b) Begin of filling, LV-side view

Max=3.5

Max=17.4

(c) Begin of ejection, RV-side view   (d) Begin of ejection, LV-side view

Max=341.5

Max=462.9
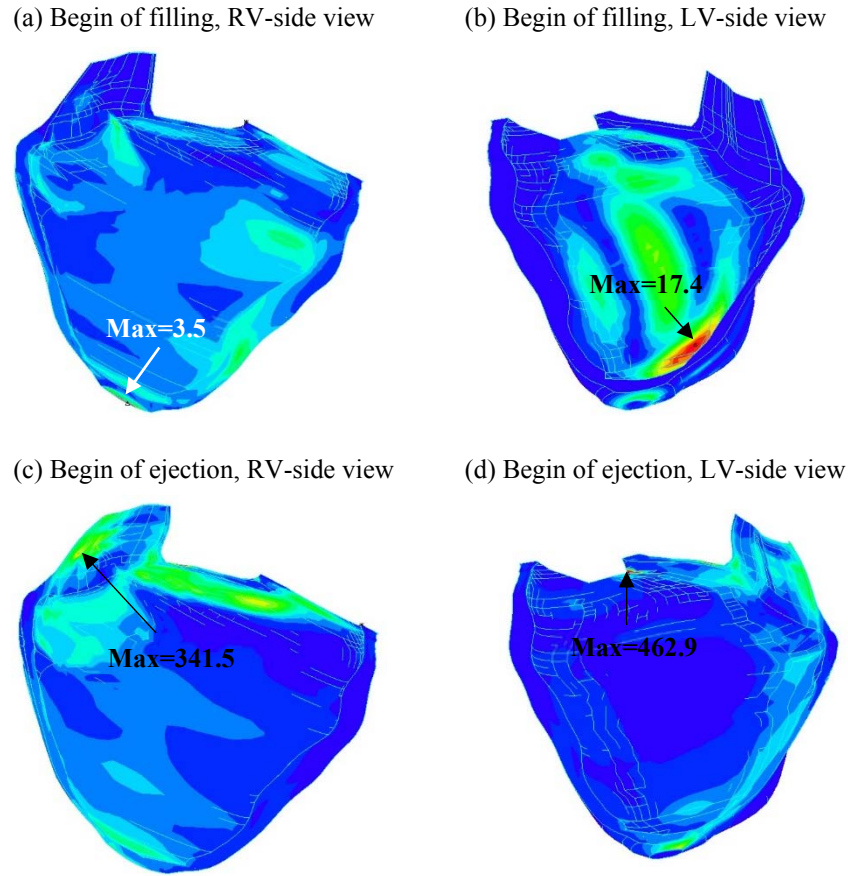
Figure 11.4 Flow maximum shear stress viewed with a cut surface passing through the RV showing overall FMSS distributions on RV inner surfaces, from a WPG patient. (a-b) FMSS distributions at begin of filling from RV-side and LV-side views. (c-d) FMSS distributions at begin of ejection from RV-side and LV-side views.

11.3 Comparison between FSI Models and Structure-only Models

From all the pressure distribution plots, it was easy to find that distribution of pressure in RV wasn't uniform everywhere which was different from the assumption in our structure-only models. In structure-only models, we applied pressure condition on RV inner surface uniformly. So, FSI models don't only provide us with the numerical results about flow part, but they can also provide different and maybe accurate results about the solid part compared to structure-only model.

(a) Begin of ejection, wall-only RV-side view
(b) Begin of ejection, wall-only LV-side view
(c) Begin of filling, wall-only RV-side view
(d) Begin of filling, wall-only LV-side view

Max=560.5 kPa
Max=1968
Max=127.8
Max=84.5

(e) Begin of ejection, FSI RV-side view
(f) Begin of ejection, FSI LV-side view
(g) Begin of filling, FSI RV-side view
(h) Begin of filling, FSI LV-side view

Max=515.2 kPa
Max=624.1
Max= -2.3
Max=27.2

Figure 11.5 Wall stress comparison between FSI models and 1G models, units kPa.

Figure 11.5 gave the stress-P_1 distribution on RV inner surface obtained from FSI model of the WPG patient and compared with the results from its corresponding structure-only model. At each time point, two views were given to show both RV-side and LV-side results. Fig. 11.5(a-d) gave the results at begin of ejection and a uniform scale was used in the four plots. Similar distribution was found at begin of ejection between FSI model and structure-only model, but the stress values of FSI model were smaller than those from structure-only model. Figure 11.5 (e-h) gave the results at begin of filling and a uniform scale was used to compare FSI model with structure-only model.. At the beginning of filling, stress-P_1 distribution of FSI model was completely different from that of structure-only model including pattern and values.

11.4 Comparison between BPG Patient and WPG Patient

Numerical flow results from the BPG patient and the WPG patient were compared to see if any difference existed in flow parameters, furthermore these flow parameters might be used as potential predictors for surgery outcome. Due to hard convergence for FSI models, in this project we only built two FSI models due to time limit. The comparison between BPG and WPG was only a preliminary result that aimed to provide some new sights about outcome prediction.

Figure 11.6 showed the comparison of velocity maps between the BPG patient and the WPG patient at begin/end of filling and ejection phase. Maximal and mean velocity magnitudes were summarized and compared in table 11.2, and the approximate kinetic energy of RV flow were also given in table 11.2. Figure 11.7 showed the comparison of maximal shear stress distribution between the BPG patient and the WPG patient begin/end of filling and ejection phase.

Through these comparisons, the large differences have been observed in velocity and maximal shear stress between the selected BPG and WPG patient. BPG patient has a lower magnitude of velocity and higher maximal shear stress than the WPG patient. However, more patients are needed to verify these findings.

(a) Begin of filling, BPG
Max=124.6 cm/s

(b) End of filling, BPG
Max=28.22 cm/s

(c) Begin of ejection, BPG
Max=13.76 cm/s

(d) End of ejection, BPG
Max=78.13 cm/s

(e) Begin of filling, WPG
Max=122.5 cm/s

(f) End of filling, WPG
Max=38.86 cm/s

(g) Begin of ejection, WPG
Max=34.03 cm/s

(h) End of ejection, WPG
Max=64.22 cm/s
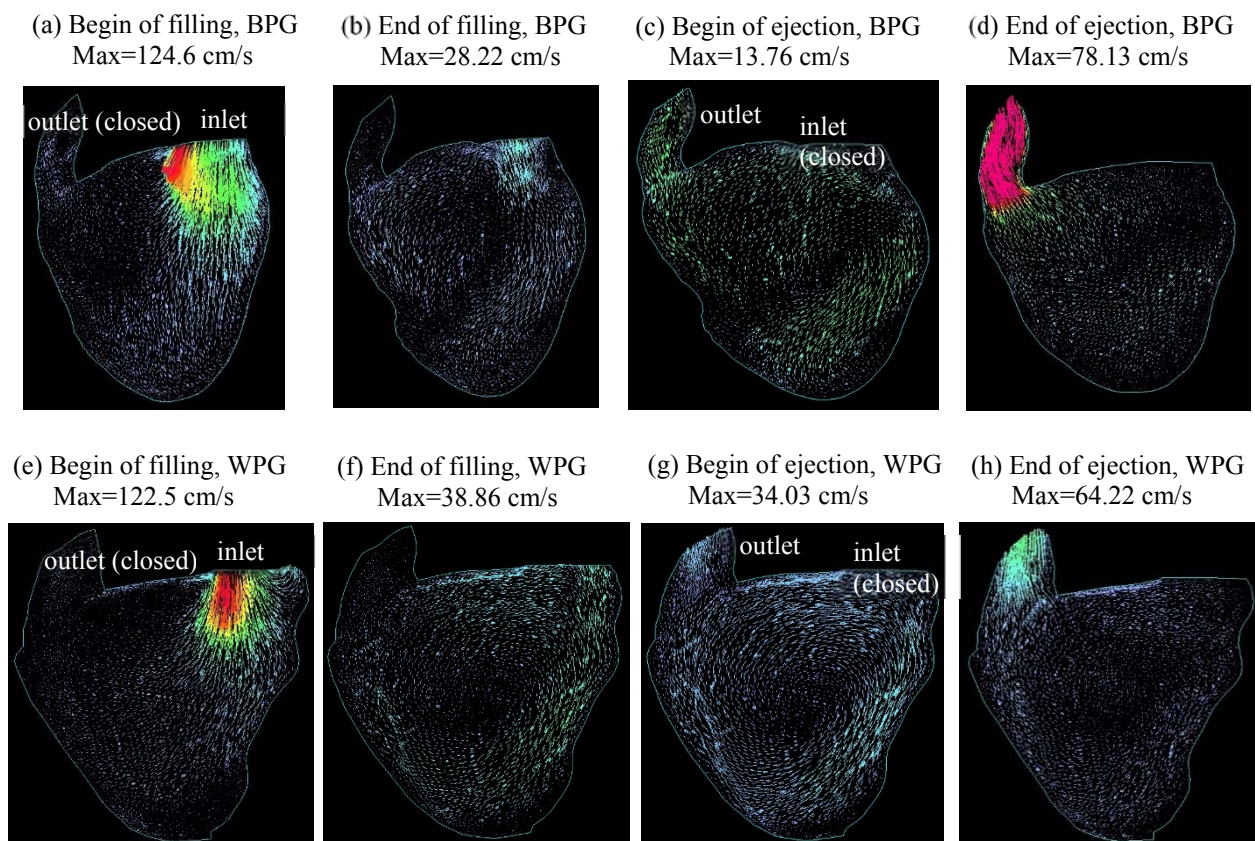
Figure 11.6 Comparison of velocity maps between the BPG patient and the WPG patient at begin/end of filling and ejection phase, (a-d) Velocity maps of BPG patient at begin/end of filling and ejection; (e-h) Velocity maps of WPG patient at begin/end of filling and ejection.

Time	Max velocity magnitude (cm/s)		Mean velocity magnitude (cm/s)		kinetic energy (J)	
	BPG	WPG	BPG	WPG	BPG	WPG
Begin of Filling	26.56	88.72	3.38	9.68	3.82e-4	0.0128
Time of max velocity	163.33	509.21	12.37	34.74	0.0169	0.2707
End of Filling	28.56	41.10	5.95	11.70	0.0019	0.0149
Begin of Ejection	18.96	34.76	5.16	10.95	0.0013	0.0125
Time of max velocity	107.42	337.32	6.00	17.84	0.0028	0.0850
End of Ejection	89.30	135.69	4.81	9.77	0.0026	0.0160

Table 11.2 Comparison of maximal and mean velocity magnitude also with approximate kinetic energy of RV flow between BPG and WPG patients at selected time points.

125
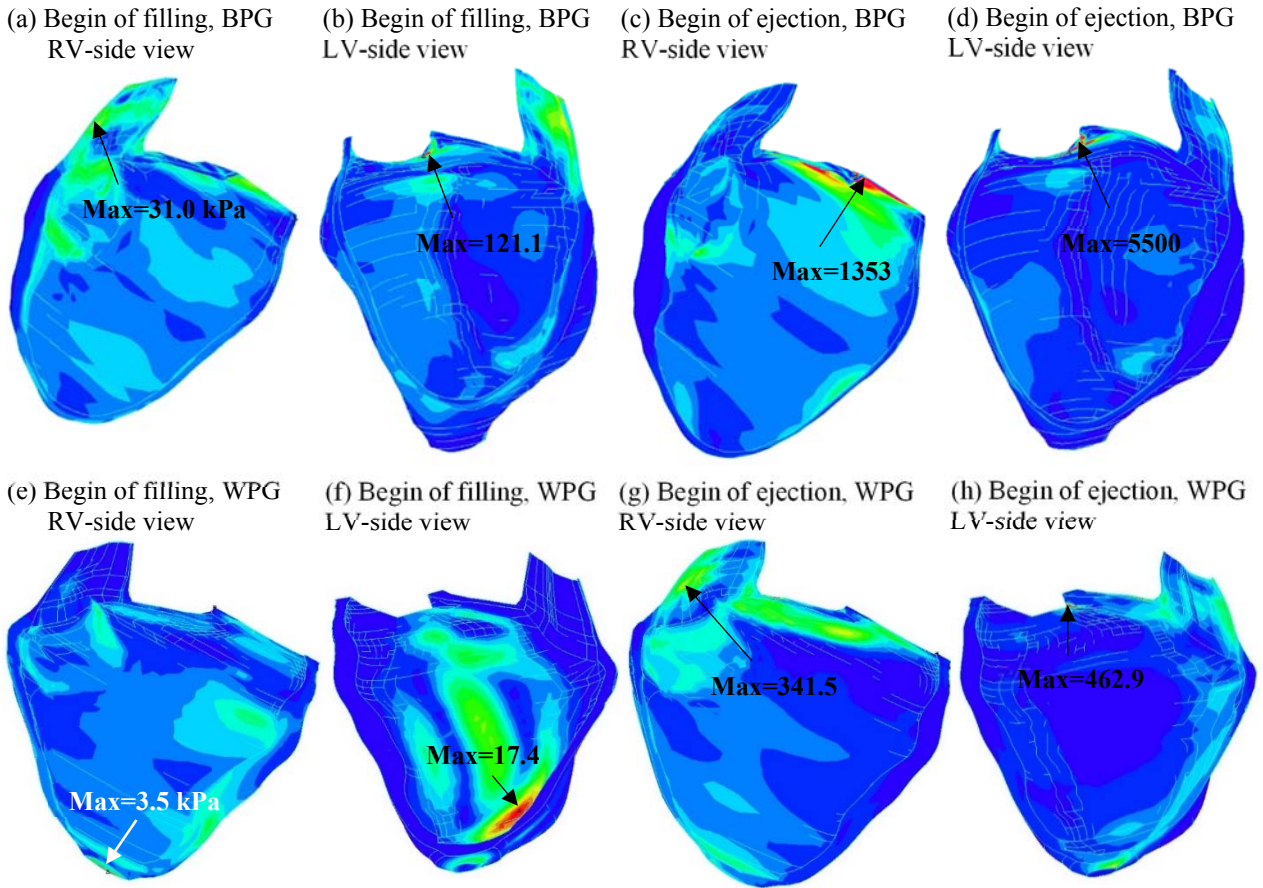
Figure 11.7 Comparison of maximal shear stress (MSS) distribution between the BPG patient and the WPG patient at begin/end of filling and ejection phase, (a-d) MSS distribution of BPG patient at begin/end of filling and ejection; (e-h) MSS distribution of WPG patient at begin/end of filling and ejection.

11.5 Conclusion

Based on 1G models, we constructed 2 FSI models by introducing fluid part and fluid-structure-interaction. First, FSI models can provide flow-related information, such as flow velocity, pressure, and shear stress which lack in structure-only models. Then, comparison between FSI models and structure-only models indicated that mechanical stress had large differences between two different types of models. The differences might be caused by the non-uniform RV pressure distribution in FSI models, while RV pressure was prescribed uniformly on RV inner surface in

structure-only models. Finally, we also compared the flow results between BPG and WPG patients, and the comparative results showed that velocity and maximal shear stress differed a lot from the selected BPG to WPG patient. Due to time limitation, only two FSI models were constructed in this project and a large number of FSI are needed to verify the preliminary results.

12. Discussion

12.1. Significance of the Work and Related Fundamental Issues

In this project, morphological and mechanical analyses were performed on the selected TOF patients and healthy volunteers who previously enrolled in our RV surgical remodeling trials. Different kinds of patient-specific computational models of RV/LV were constructed and solved in ADINA to obtain morphological and mechanical parameter values. Comparisons between TOF patient group and healthy control group shows that TOF patients' ventricles have large differences on both geometry and mechanics, such as RV volume, SA, SVR, WT, C-cur and Stress-P_1, meanwhile RV SA, SVR, L-cur and Stress-P_1 were found have largest differences between BPG and WPG among all the included parameters and may be considered as good indicators for PVR outcome. These complex computational models have been used to evaluate the RV of patients with repaired TOF and provide new insights into RV morphology, geometry and mechanic.

Due to the complicated structure and irregular geometry of human ventricles especially right ventricle, it is very difficult to obtain the convergent solutions of such highly non-linear 3D computational model with or without fluid-structure-interaction. Geometry-fitting technique was applied to generate the proper volumes and meshes for model convergence. 22 structure-only 1G models, 16 structure-only 2G models and two FSI models were solved successfully.

Initial conditions are crucial for numerical simulation. Because the measurement of stress condition is extremely hard or even impossible in experiments, we choose zero-stress status as the initial status for our simulations. In this project, all the geometry information was obtained from *in vivo* MRIs. *In vivo* indicates that all the geometry information is obtained under pressure thus the geometry information is not zero-stress. Pre-modelling shrink is introduced to obtain zero-stress geometry for initial conditions. Correct initial conditions are fundamentally important for

correct stress/strain calculation which play a significant role in many cardiovascular research related with mechanical forces, such as ventricle remodelling, tissue regeneration, cell activities and etc. A new 2G modelling is introduced in this project, which is aiming to set up the right stage for diastole and systole stress/strain calculations using two proper zero-load geometries. Actual ventricle contraction and relaxation are very complex, zero-load sarcomere length is very difficult to be measured directly. Thus, it is hard to have a commonly accepted assumption about zero-load geometries. Our 2G model is one novel improvement over 1G model making our models closer to the real one.

FSI models were also constructed and solved in this project. Different from the immersed boundary method which is the most famous fictitious FSI method where heart wall is simplified as a network of neutrally buoyant fibers, our FSI models adopt realistic FSI method where the structure is assumed as a 3D hyperelastic, anisotropic, nearly-incompressible and homogeneous materials. It is challenging to get 3D realistic FSI models convergent, however the numerical simulations can provide both flow and structure results. Comparison between structure-only models and FSI models shows that Stress-P_1 of structure part in FSI models are different from that of structure-only models especially in the middle of filling and ejection. This difference is caused by the effect of flow in RV on pressure distribution. In wall-only model, we assume that pressure is uniform on RV inner surface. However, FSI simulation shows that pressure in RV distributes non-uniformly and the pressure difference is large in the middle of filling and ejection. It should be noted that the pressure difference at begin of ejection is small in FSI model which leads to that FSI model has a similar Stress-P_1 pattern with structure-only model at begin of ejection. Structure-only model is a simplification of FSI model and easier to get convergent in simulations. The

similarities found between structure-only model and FSI model guarantee that structure-only model is still reliable in some researches where only structure results are focused on.

12.2 Limitation and improvement

In mechanical analysis, small sample size is one limitation. To obtain mechanical results, 3D finite element models for RV/LV are constructed and solved in ADINA. Due to the complexity of model construction and current computer technology, it generally takes around one month to build and solve one structure-only 1G model. Therefore, there are only 16 models for TOF patients and 6 models for healthy volunteers constructed for mechanical analysis which leads to a limited statistical analysis. Improving the model construction process to reduce the time for model building is one important work in the future.

In this project, we chose RVEF change as the only metric for PVR surgical outcome; more clinical metrics should be used for PVR surgical outcome to obtain results that are more reliable.

The patients included in this project are selected from the patients who previously enrolled in RV surgical remodeling trials and underwent PVR surgeries. This selection leads to that our study sample cannot reflect the general population of patients with rTOF very well.

Several improvements can be added to our current models in the future for better accuracy and applicability. 1) Valve mechanics. Valves can be added into our model for better flow control at the inlet and outlet. With valves, pulmonary regurgitation can be assessed which is important to TOF surgical management. 2) Fiber orientation. Inclusion of patient-specific fiber orientation will be very desirable for improved accuracy of our models. 3) Active contraction. Develop the methods for modeling active contraction by adding active stress and the techniques for adjusting zero-stress geometry is important for model improvement. 4) Tissue mechanical properties. Direct

measurement of tissue mechanical properties is a desirable addition to improve accuracy of our models.

13. Conclusion

13.1 Summary

In this dissertation, several 3D patient-specific CMR-based computational methods were introduced to perform morphological and mechanical analysis on RV for the patients with rTOF in order to identify parameters which may be related to PVR outcome. Segmented CMR images provide the geometry information for numerical modelling. Motion equations with non-linear Mooney-Rivlin model and Navier-Stokes equations with ALE formulation are used to describe the structure and flow part respectively. Finite Element Method is used to solve the models numerically. Specific modeling techniques include 3D reconstruction of CMR-based contours, geometry-fitting mesh generation method, pre-shrink process and shrink-stretch process for material properties determination. CMR-based RV volume data are used to validate the numerical results from computational modelling.

Eighty 3D geometry-only models for RV/LV of 56 selected TOF patients and 20 healthy volunteers were reconstructed from segmented CMR contours to investigate the potential relation between pre-PVR RV geometry and PVR outcome. The results indicate that RV SA, SVR and L-cur are good indicators to differentiate better-outcome patients from worse-outcome patients (section 8.5.2). Besides, significant correlations with ∆RVEF are found in RV volume, SA, SVR and L-cur (section 8.6). Through logistic regression analysis with 2-fold cross-validation procedure, some combinations of geometrical parameters are found to be potential indictors to divide two PVR outcome groups, such as SVR + C-cur , C-cur + L-cur +WT and etc (section 8.7).

Twenty-two 3D patient-specific RV/LV structure-only 1G models for 16 TOF patients and 6 healthy volunteers are constructed for mechanical analysis to search for the potential indicators for PVR outcome from mechanical parameters. Sixteen adjusted 2G models for 16 TOF patients

were built based on the corresponding 1G models to improve stress/strain calculations. Two FSI models for 2 TOF patients were constructed by adjusting their corresponding structure-only models to mainly investigate the flow pattern in RV and its effect on RV. The following results were obtained: 1) ΔRVEF has a significant correlation with Stress-P_1 (section 9.2); 2) Stress-P_1 shows great potential to differentiate BPG from WPG with the help of HG (section 9.3.2 & section 9.4 & section 9.5); 3) 2G models have similar results with 1G models at begin of filling and ejection, and significantly different results from 1G models at end of filling and ejection (section 10.2); 4) FSI model shows different RV stress pattern from structure-only model (section 11.3), and FSI model is able to provide flow velocity, pressure and shear stress information (section 11.2); 5) Comparison of flow results between the selected BPG and WPG patient shows large differences exist in flow parameters such as velocity magnitude and maximal shear stress (section 11.4).

Therefore, RV SA, SVR and stress might be critical indicators for PVR outcome predications. 2G model and FSI model are able to give new insight to RV property of patients with rTOF and ready to be used in the relevant investigation.

13.2 Conclusion

In this dissertation, we introduce several different kinds of computational models including geometry-only model, structure-only model and FSI model. The computational modelling shows its power in the study of clinical problems which is greatly potential to make accurate assessment of RV geometry and mechanics and also able to provide new sights to RV cardiac function. Our preliminary results indicate that RV SA, SVR, L-cur and Stress have significant correlation with RVEF change and also differ significantly from patient with better PVR outcome to patient with worse PVR outcome. With sufficient validation, these results may lead to early prediction of PVR

outcome. The MRI-based 3D patient-specific computational models proposed in this dissertation integrate surgical, imaging and modeling components, which could lead to considerable potential gain not only in surgical design and outcome prediction, but also in understanding the mechanisms of RV failure. Furthermore, the modeling process and methods proposed in this dissertation could be applicable to many other similar biological applications.

13.3 Future Work

In this project, computational models have been constructed and shown the power in the research of PVR surgeries for rTOF patients. Future investigations and effort can include the following:

1) To accumulate computational models for large-scale studies. Due to the time limitation, there is only 22 1G models, 16 2G models and 2 FSI models. Some good preliminary results have been found in this project, however large-scale studies are still needed to verify these findings and/or to explore new findings.

2) To improve the accuracy and reliability of the computational models, by including valve mechanics, patient-specific fiber orientation, patient-specific tissue mechanical properties, and active stress, *etc*.

3) To improve the model construction process to reduce the time for model building, such as introducing automation into construction process to accelerate model building. Acceleration of model building is also critically important for models accumulation.

With future improvements and validations from large-scale patient studies, the obtained quantitative indicators may be useful in predicting the outcome of PVR surgeries. Besides, these computational models have the potential to be used in clinical decision-making process to replace empirical and often risky clinical experimentation.

References

1. Abd El Rahman MY, Abdul-Khaliq H, Vogel M, Alexi-Meskishvili V, Gutberlet M, Lange PE. Relation between right ventricular enlargement, QRS duration, and right ventricular function in patients with tetralogy of Fallot and pulmonary regurgitation after surgical repair. Heart. 2000;84:416-420.

2. Anderson RH, Smerup M, Sanchez-Quintana D, Loukas M, Lunkenheimer PP. The three-dimensional arrangement of the myocytes in the ventricular walls. Clin Anat. 2009;22:64-76.

3. Appleton B, Wei Q, Liu N, Xia L, Crozier S, Liu F, et al. An electrical heart model incorporating real geometry and motion. In: 27th Annu Int Conf Eng Med Biol Soc (IEEE-EMBS 2005). Shanghai, China: IEEE; 2006. p. 345-8.

4. Arts T, Veenstra PC, Renehan RC. Epicardial deformation and left ventricular wall mechanisms during ejection in the dog. Amer J Physiol. 1982;243:379-390.

5. Aslanidi OV, Nikolaidou T, Zhao J, Smaill BH, Gilbert SH, Holden AV, et al. Application of micro-computed tomography with iodine staining to cardiac imaging, segmentation, and computational model development. IEEE Trans Med Imaging. 2013;32:8-17.

6. Axel L. Biomechanical dynamics of the heart with MRI. Annu Rev Biomed Eng. 2002;4:321-347.

7. Bacha EA, Scheule AM, Zurakowski D, Erickson LC, Hung J, Lang P, Mayer JE, Jr., del Nido PJ, Jonas RA. Long-term results after early primary repair of tetralogy of Fallot. J Thorac Cardiovasc Surg. 2001;122:154-161.

8. Bayer JD, Blake RC, Plank G, Trayanova NA. A novel rule-based algorithm for assigning myocardial fiber orientation to computational heart models. Ann Biomed Eng. 2012;40:2243-54.

9. Bathe KJ, Theory and Modeling Guide, Vol I: ADINA; Vol II: ADINA-F, ADINA R&D, Inc., Watertown, MA, P309-310, 2002.

10. Bathe KJ. Finite Element Procedures. Prentice Hall, Inc; New Jersey: 1996.

11. Bathe KJ, Wilson EL, Numerical methods in finite element analysis. Prentice-Hall Inc., Englewood Cliffs, N.J., 1976.

12. Bathe KJ, ZHANG H, Wang MH. Finite element analysis of incompressible and compressible fluid flows with free surfaces and structural interactions. Comput Struct. 1995; 56(2-3):193-213.

13. Billiar KL, Sacks MS. Biaxial mechanical properties of the natural and glutaraldehyde treated aortic valve cusp--Part I: Experimental results. J Biomech Eng. 2000;122(1):23-30.

14. Bishop MJ, Hales P, Plank G, Gavaghan DJ, Scheider J, Grau V. Comparison of rule-based and DTMRI-derived fibre architecture in a whole rat ventricular computational model. In: Funct Imaging Model Heart 2009, LNCS 5528. Berlin Heidelberg: Springer-Verlag; 2009. p. 87-96.

15. Bricker JT. Sudden death and tetralogy of Fallot. Risks, markers, and causes. Circulation. 1995; 92:158-159.

16. Brown DW, Powell AJ, Geva T. Imaging complex congenital heart disease - functional single ventricle, the Glenn circulation and the Fontan circulation: A multimodality approach. Progress in Pediatric Cardiology 2010; 28: 45-58.

17. Centers for Disease Control and Prevention, (CDC) (6 January 2006). "Improved national prevalence estimates for 18 selected major birth defects--United States, 1999-2001.". MMWR. Morbidity and mortality weekly report 54 (51): 1301-5.

18. Clerc L. Directional differences of impulse spread in trabecular muscle from mammalian heart. J Physiol. 1976; 255:335-46.

19. Chadwick RS. Mechanics of the left ventricle. Biophys J. 1982; 39:279-288.

20. Chahboune B, Crolet JM. Numerical simulation of the blood-wall interaction in the human left ventricle. Eur Phys J - Appl Phys. 1998; 2:291-297.

21. Cheng Y, Oertel H, Schenkel T. Fluid–structure coupled CFD simulation of the left ventricular flow during filling phase. Ann Biomed Eng. 2005; 33:567-576.

22. Choe YH, Kang IS, Park SW, Lee HJ. MR imaging of congenital heart diseases in adolescents and adults. Korean J Radiol. 2001;2:121-131.

23. Colli Franzone P, Guerri L, Pennacchio M, Taccardi B. Spread of excitation in 3-D models of the anisotropic cardiac tissue. II. Effects of fiber architecture and ventricular geometry. Math Biosci. 1998;147:131-71.

24. Davlouros PA, Kilner PJ, Hornung TS, Li W, Francis JM, Moon JC, Smith GC, Tat T, Pennell DJ, Gatzoulis MA. Right ventricular function in adults with repaired tetralogy of Fallot assessed with cardiovascular magnetic resonance imaging: detrimental role of right ventricular outflow aneurysms or akinesia and adverse right-to-left ventricular interaction. J Am Coll Cardiol. 2002;40:2044-2052.

25. Demer LL, Yin FCP. Passive biaxial mechanical properties of isolated canine myocardium. J Physiol London. 1983; 339:615-30.

26. Discigil B, Dearani JA, Puga FJ, et al. Late pulmonary valve replacement after repair of tetralogy of Fallot. J Thorac Cardiovasc Surg. 2001;121:344-51.

27. d'Udekem Y, Rubay J, Shango-Lody P, Ovaert C, Vliers A, Caliteaux M, Sluysmans T. Late homograft valve insertion after transannular patch repair of tetralogy of Fallot. J Heart Valve Dis. 1998; 7:450-454.

28. Emery JL, Omens JH. Mechanical regulation of myocardial growth during volume-overload hypertrophy in the rat. Am J Physiol Heart Circ Physiol. 1997; 273: 1198-204.

29. Emery J, Omens J, McCulloch A. Biaxial mechanics of passively overstretched left ventricle. Am J Physiol Heart Circ Physiol. 1997; 272:H2299-305

30. Eyskens B, Reybrouck T, Bogaert J, Dymarkowsky S, Daenen W, Dumoulin M, Gewillig M. Homograft insertion for pulmonary regurgitation after repair of tetralogy of fallot improves cardiorespiratory exercise performance. Am J Cardiol. 2000;85:221-225.

31. Galecki A, Burzykowski T. Linear Mixed-effects Models Using R. Springer Science+Business Media New York: 2013.

32. Gatzoulis MA, Elliott JT, Guru V, Siu SC, Warsi MA, Webb GD, Williams WG, Liu P, McLaughlin PR. Right and left ventricular systolic function late after repair of tetralogy of Fallot. Am J Cardiol. 2000;86:1352-1357.

33. Geva T, Greil GF, Marshall AC, Landzberg M, Powell AJ. Gadolinium-enhanced 3-dimensional magnetic resonance angiography of pulmonary blood supply in patients with complex pulmonary stenosis or atresia: comparison with x-ray angiography. Circulation. 2002;106:473-478.

34. Geva T, Sandweiss BM, Gauvreau K, Lock JE, Powell AJ. Factors associated with impaired clinical status in long-term survivors of tetralogy of Fallot repair evaluated by magnetic resonance imaging. J Am Coll Cardiol. 2004;43:1068-1074.

35. Graham TP, Jr. Management of pulmonary regurgitation after tetralogy of fallot repair. Curr Cardiol Rep. 2002;4:63-67.

36. Guccione JM, McCulloch AD. 1991. Finite element modeling of ventricular mechanics. See Ref. 189, pp.121–44

37. Guccione JM, McCulloch AD, Waldman LK. Passive material properties of intact ventricular myocardium determined from a cylindrical model. J Biomech Eng. 1991;113(1):42-55.

38. Guccione JM, McCulloch AD, Waldman LK. Passive material properties of intact ventricle determined from a cylindrical model. ASME J. Biomech. Eng. 1991;113:42-55

39. Guccione JM, McCulloch AD. Mechanics of active contraction in cardiac muscle: Part I--Constitutive relations for fiber stress that describe deactivation. J Biomech Eng. 1993;115(1):72-81.

40. Guccione JM, Waldman LK, McCulloch AD. Mechanics of active contraction in cardiac muscle: Part II--Cylindrical models of the systolic left ventricle. J Biomech Eng. 1993;115(1):82-90.

41. Guccione JM, Costa KD, McCulloch AD. Finite element stress analysis of left ventricular mechanics in the beating dog heart. J Biomech. 1995;28(10):1167-77.

42. Guccione JM, Le Prell GS, de Tombe PP, Hunter WC. Measurements of active myocardial tension under a wide range of physiological loading conditions. J Biomech. 1997;30(2):189-92.

43. Gurev V, Constantino J, Rice JJ, Trayanova NA. Distribution of electromechanical delay in the heart: insights from a three-dimensional electromechanical model. Biophys J. 2010;99, 745-754.

44. Gurev V, Lee T, Constantino J, Arevalo H, Trayanova NA. Models of cardiac electromechanics based on individual hearts imaging data: Image-based electromechanical models of the heart. Biomech Model Mechanobiol. 2011;10:295-306.

45. Haddad R, Clarysse P, Orkisz M, Croisille P, Revel D, Magnin IE. A realistic anthropomorphic numerical model of the beating heart. In: Funct Imaging Model Heart 2005, LNCS 3504. Berlin Heidelberg: Springer–Verlag; 2005. p. 384-93.

46. Helbing WA, de Roos A. Clinical applications of cardiac magnetic resonance imaging after repair of tetralogy of Fallot. Pediatr Cardiol. 2000;21:70-79.

47. Helbing WA, de Roos A. Optimal imaging in assessment of right ventricular function in tetralogy of Fallot with pulmonary regurgitation. Am J Cardiol. 1998;82:1561-1562.

48. Helbing WA, Niezen RA, Le Cessie S, van der Geest RJ, Ottenkamp J, de Roos A. Right ventricular diastolic function in children with pulmonary regurgitation after repair of tetralogy of Fallot: volumetric evaluation by magnetic resonance velocity mapping. J Am Coll Cardiol. 1996;28:1827-1835.

49. Humphrey JD, Strumpf RK, Yin FCP. Determination of a constitutive relation for passive myocardium. II. Parameter estimation. ASME J Biomech Eng. 1990b; 112:340-46.

50. Humphrey JD, Cardiovascular Solid Mechanics, Springer-Verlag, New York, 2002.

51. Hunter PJ, Smaill BH. The analysis of cardiac function: a continuum approach. Prog Biophys Molec Biol. 1989; 52:101-64.

52. Hunter PJ, McCulloch AD, ter Keurs HEDJ. Modeling the mechanical properties of cardiac muscle. Prog Biophys Molec Biol. 1998;69:289-331.

53. Hunter PJ, Pullan AJ, Smaill BH. Modeling total heart function. Annu Rev Biomed Eng. 2003;5:147-77.

54. Huxley AF. Muscle structure and theories of contraction. Prog Biophys Chem. 1957; 7:255-318.

55. Jie X, Gurev V, Trayanova N. Mechanisms of mechanically induced spontaneous arrhythmias in acute regional ischemia. Circ Res. 2010; 106:185-192.

56. Just H, Holubarsch C, Friedburg H. Estimation of left ventricular volume and mass by magnetic resonance imaging: comparison with quantitative biplane angiocardiography. Cardiovasc Intervent Radiol. 1987;10:1-4.

57. Kerckhoffs RCP, Bovendeerd PHM, Kotte JCS, Prinzen FW, Smits K, Arts T. Homogeneity of cardiac contraction despite physiological asynchrony of depolarization: a model study. Ann Biomed Eng. 2003;31:536–47.

58. Kerckhoffs RC, Omens JH, Mcculloch AD, Mulligan LJ. Ventricular dilation and electrical dyssynchrony synergistically increase regional mechanical nonuniformity but not mechanical dyssynchrony: a computational model. Circ Heart Fail. 2010; 3:528-536.

59. Kondo C, Caputo GR, Semelka R, Foster E, Shimakawa A, Higgins CB. Right and left ventricular stroke volume measurements with velocity-encoded cine MR imaging: in vitro and in vivo validation. AJR Am J Roentgenol. 1991;157:9-16.

60. Lamata P, Niederer S, Nordsletten D, Barber DC, Roy I, Hose DR, et al. An accurate, fast and robust method to generate patient-specific cubic Hermite meshes. Med Image Anal. 2011;15:801–13.

61. Landesberg A, Sideman S. Mechanical regulation of cardiac-muscle by coupling calcium kinetics with cross-bridge cycling—A dynamic-model. Amer J Physiol. 1994; 267:H779–H795.

62. Landesberg A, Livshitz L, Keurs H ter. The effect of sarcomere shortening velocity on force generation, analysis, and verification of models for crossbridge dynamics. Ann Biomed Eng. 2000 28:968–978.

63. Lassila T, Malossi ACI, Stevanella M, Votta E, Redaelli A, Deparis S. Multiscale fluid–structure interaction simulation of patient-specific left ventricle fluid dynamics with fictitious elastic structure regularization. Int J Numer Methods Biomed Eng. 2012; 00:1–23.

64. Latson LA, Powell KA, Sturm B, Schvartzman PR, White RD. Clinical validation of an automated boundary tracking algorithm on cardiac MR images. Int J Cardiovasc Imaging. 2001;17:279-286.

65. Lee D, Fuisz AR, Fan PH, Hsu TL, Liu CP, Chiang HT. Real-time 3-dimensional echocardiographic evaluation of left ventricular volume: correlation with magnetic resonance imaging--a validation study. J Am Soc Echocardiogr. 2001;14:1001-1009.

66. Lee J, Niederer S, Nordsletten D, Grice IL, Smail B, Kay D, Smith N (2009) Coupling contraction, excitation, ventricular and coronary blood flow across scale and physics in the heart. Philos Trans R Soc A. 1986; 367:2311-2331.

67. LeGrice I, Smaill B, Chai L, Edgar S, Gavin J, Hunter P. Laminar structure of the heart: ventricular myocyte arrangement and connective tissue architecture in the dog. Am J Physiol Heart Circ Physiol. 1995;269:H571-82.

68. Lemmon JD, Yoganathan AP. Computational modeling of left heart diastolic function: examination of ventricular dysfunction. J Biomech Eng. 2000; 122(4):297-303.

69. Li W, Kohl P, Trayanova N. Induction of ventricular arrhythmias following mechanical impact: a simulation study in 3D. J Mol Histol. 2004; 35, 679-686.

70. Li W, Kohl P, Trayanova N. Myocardial ischemia lowers precordial thump efficacy: an inquiry into mechanisms using three-dimensional simulations. Heart Rhythm 2006; 3:179-186.

71. Lorenz CH, Walker ES, Morgan VL, Klein SS, Graham TP, Jr. Normal human right and left ventricular mass, systolic function, and gender differences by cine magnetic resonance imaging. J Cardiovasc Magn Reson. 1999;1:7-21.

72. Mahle WT, Parks WJ, Fyfe DA, et al. Tricuspid regurgitation in patients with repaired tetralogy of Fallot and its relation to right ventricular dilatation. Am J Cardiol. 2003;92:643-645.

73. McCulloch AM, Waldman L, Rogers J, Guccione J. Large-scale finite element analysis of the beating heart, Critical Rev. in Biomedical Engineering, 1992;20(5,6): 427-449.

74. McCulloch AM, et al. Continuity 6 (a package distributed free by the National Biomedical Computation Resource), www.continuity.ucsd.edu. 2007.

75. McQueen DM, Peskin CS. A three-dimensional computer model of the human heart for studying cardiac fluid dynamics. ACM SIGGRAPH Comput Graph 2000; 34(1):56–60.

76. Nash MP, Hunter PJ. Computational Mechanics of the Heart, From Tissue Structure to Ventricular Function. Journal of Elasticity. 2000;61:113–141.

77. Nevo E, Structural finite deformation model of the left ventricle during diastole and systole. J Biomech Eng. 1989; 111:342-349.

78. Nichols K, Saouaf R, Ababneh AA, Barst RJ, Rosenbaum MS, Groch MW, Shoyeb AH, Bergmann SR. Validation of SPECT equilibrium radionuclide angiographic right ventricular parameters by cardiac magnetic resonance imaging. J Nucl Cardiol. 2002;9:153-160.

79. Niederer S, Rhode K, Razavi R, Smith N. The importance of model parameters and boundary conditions in whole organ models of cardiac contraction. In: Funct Imaging Model Heart 2009, LNCS 5528. Berlin Heidelberg: Springer–Verlag; 2009. p. 348–56.

80. Niederer SA, Plank G, Chinchapatnam P, Ginks M, Lamata P, Rhode KS, Rinaldi CA, Razavi R, Smith NP. Length-dependent tension in the failing heart and the efficacy of cardiac resynchronization therapy. Cardiovasc Res. 2011; 89:336-343.

81. Nielsen PMF, LeGrice IJ, Smaill BH, Hunter PJ. Mathematical model of geometry and fibrous structure of the heart. Am J Physiol Heart Circ Physiol. 1991;260:H1365–78.

82. Niezen RA, Helbing WA, van der Wall EE, van der Geest RJ, Rebergen SA, de Roos A. Biventricular systolic function and mass studied with MR imaging in children with pulmonary regurgitation after repair for tetralogy of Fallot. Radiology. 1996;201:135-140.

83. Niezen RA, Helbing WA, van Der Wall EE, van Der Geest RJ, Vliegen HW, de Roos A. Left ventricular function in adults with mild pulmonary insufficiency late after Fallot repair. Heart. 1999;82:697-703.

84. Nollert G, Fischlein T, Bouterwek S, Bohmer C, Klinner W, Reichart B. Long-term survival in patients with repair of tetralogy of Fallot: 36-year follow-up of 490 survivors of the first year after surgical repair. J Am Coll Cardiol. 1997;30:1374-1383.

85. Novak VP, Yin FCP, Humphrey JD. Regional mechanical properties of passive myocardium. J. Biomech. 1994; 27:403-12.

86. Omens JH, MacKenna DA, McCulloch AD. Measurement of strain and analysis of stress in resting rat left ventricular myocardium. J Biomech. 1991; 26:665-76.

87. Owen AR, Gatzoulis MA. Tetralogy of Fallot: Late outcome after repair and surgical implications. Semin Thorac Cardiovasc Surg Pediatr Card Surg Annu. 2000;3:216-226.

88. Ordas S, Oubel E, Sebastian R, Frangi AF. Computational anatomy atlas of the heart. In: 5th Int Symp Image Signal Process Anal (ISPA 2007). Istanbul, Turkey: IEEE; 2007. p. 338–42.

89. Panerai RB. A model of cardiac muscle mechanics and energetics. J Biomech. 1980; 13: 929 -940.

90. Panfilov AV, Keldermann RH, Nash MP. Drift and breakup of spiral waves in reaction-diffusion-mechanics systems. Proc Natl Acad Sci. U.S.A. 2007; 104:7922-7926.

91. Peterson JN, Hunter WC, Berman MR. Estimated time course of Ca-2+ bound to troponin C during relaxation in isolated cardiac-muscle. Amer J Physiol. 1991; 260:H1013-H1024.

92. Pini R, Giannazzo G, Di Bari M, Innocenti F, Rega L, Casolo G, Devereux RB. Transthoracic three-dimensional echocardiographic reconstruction of left and right ventricles: in vitro validation and comparison with magnetic resonance imaging. Am Heart J. 1997;133:221-229.

93. Powell AJ, Chung T, Landzberg MJ, Geva T. Accuracy of MRI evaluation of pulmonary blood supply in patients with complex pulmonary stenosis or atresia. Int J Card Imaging. 2000;16:169-174.

94. Razumova MV, Bukatina AE, Campbell KB. Stiffness-distortion sarcomere model for muscle simulation. J Appl Physiol. 1999; 87:1861-1876.

95. Rebergen SA, Chin JG, Ottenkamp J, van der Wall EE, de Roos A. Pulmonary regurgitation in the late postoperative follow-up of tetralogy of Fallot. Volumetric quantitation by nuclear magnetic resonance velocity mapping. Circulation. 1993;88:2257-2266.

96. Rebergen SA, de Roos A. Congenital heart disease. Evaluation of anatomy and function by MRI. Herz. 2000;25:365-383.

97. Regnier M, Morris C, Homsher E. Regulation of the crossbridge transition from a weakly to strongly bound state in skinned rabbit muscle fibers. Amer J Physiol, Cell Physiol. 1995; 269: C1532–C1539.

98. Rice JJ, Winslow RL, Hunter WC. Comparison of putative cooperative mechanisms in cardiac muscle: Length dependence and dynamic responses. Amer J Physiol Heart Circulat Physiol. 1999; 276: H1734–H1754.

99. Roest AA, Helbing WA, Kunz P, van den Aardweg JG, Lamb HJ, Vliegen HW, van der Wall EE, de Roos A. Exercise MR imaging in the assessment of pulmonary regurgitation and biventricular function in patients after tetralogy of fallot repair. Radiology. 2002;223:204-211.

100. Romero D, Sebastian R, Bijnens BH, Zimmerman V, Boyle PM, Vigmond EJ, et al. Effects of the purkinje system and cardiac geometry on biventricular pacing: a model study. Ann Biomed Eng. 2010;38:1388-98.

101. Sachse FB, Seemann G, Chaisaowong K, Weiss D. Quantitative reconstruction of cardiac electromechanics in human myocardium: Assembly of electrophysiologic and tension generation models. J Cardiovasc Electrophysiol. 2003; 14:S210–S218.

102. Sacks MS, Chuong CJ. Biaxial mechanical properties of passive right ventricular free wall myocardium. J Biomech Eng. 1993;115:202-205.

103. Sermesant M, Moireau P, Camara O, Sainte-Marie J, Andriantsimiavona R, Cimrman R, et al. Cardiac function estimation from MRI using a heart model and data assimilation: advances and difficulties. Med Image Anal. 2006;10:642-56.

104. Singh GK, Greenberg SB, Yap YS, Delany DP, Keeton BR, Monro JL. Right ventricular function and exercise performance late after primary repair of tetralogy of Fallot with the transannular patch in infancy. Am J Cardiol. 1998;81:1378-1382.

105. Smaill B, Hunter P. Structure and function of the diastolic heart: material properties of passive myocardium. 1991; 189: 1-29.

106. Stauffer NR, Greenberg SB, Marks LA, Singh GK, Siderio DL. Validation of right ventricular volume measurements by magnetic resonance imaging in small hearts using a fetal lamb model. Invest Radiol. 1995;30:87-89.

107. Stevens C, Hunter PJ. Sarcomere length changes in a 3D mathematical model of the pig ventricles. Progress in Biophysics & Molecular Biology. 2003;82:229-241.

108. Stevens C, Remme E, LeGrice I, Hunter P. Ventricular mechanics in diastole: material parameter sensitivity. J Biomech. 2003;36(5):737-48.

109. Streeter DDJ, Bassett DL. An engineering analysis of myocardial fiber orientation in pig's left ventricle in systole. Anat Rec. 1966;155:503-11.

110. Taber LA, Yang M, Podszus WW. Mechanics of ventricular torsion. J Biomech. 1996; 29: 745-752.

111. Tang D, Yang C, Zheng J, Woodard PK, Sicard GA, Saffitz JE, and Yuan C. 3D MRI-Based Multi-Component FSI Models for Atherosclerotic Plaques a 3-D FSI model. Annals of Biomedical Engineering. 2004;32(7):947-960.

112. Tang D, Yang C, Zheng J, Woodard PK, Saffitz JE, Petruccelli JD, Sicard GA, Yuan C. Local Maximal Stress Hypothesis and Computational Plaque Vulnerability Index for Atherosclerotic Plaque Assessment, Annals of Biomedical Engineering. 2005;33(12):1789-1801.

113. Tang D, Yang C, Geva T, del Nido PJ. Patient-Specific MRI-Based 3D FSI RV/LV/Patch Models for Pulmonary Valve Replacement Surgery and Patch Optimization. J of Biomech Engineering. 2008;130(4):041010.

114. Tang D, Yang C, Geva T, del Nido PJ. Image-Based Patient-Specific Ventricle Models with Fluid-Structure Interaction for Cardiac Function Assessment and Surgical Design Optimization. Progress in Pediatric Cardiology. 2010; 30:51-62.

115. Tang D, Yang C, Geva T. A Multiphysics Modeling Approach to Develop Right Ventricle Pulmonary Valve Replacement Surgical Procedures with a Contracting Band to Improve Ventricle Ejection Fraction. Comput Struct. 2013; 122: 78-87.

116. Taylor TW, Okino H, Yamaguchi T. Three-dimensional analysis of left ventricular ejection using computational fluid dynamics. J Biomech Eng. 1994;116(1):127-130.

117. Trayanova NA, Gurev V, Constantino J, Hu Y. Mathematical models of ventricular mechano-electric coupling and arrhythmia. In Cardiac Mechano-Electric Feedback and Arrhythmias, eds P. Kohl, F. Sachs, and M. R. Franz (Oxford, UK: Oxford University Press). 2011 b; 258-266.

118. Usyk TP, Mazhari R, McCulloch AD. Effect of laminar orthotropic myofiber architecture on regional stress and strain in the canine left ventricle. J Elast. 2000; 61:143-64.

119. Usyk TP, McCulloch AD. Relationship between regional shortening and asynchronous electrical activation in a three-dimensional model of ventricular electromechanics. J Cardiovasc Electrophysiol. 2003;14:S196-S202.

120. Vetter FJ, McCulloch AD. Three-dimensional analysis of regional cardiac function: a model of rabbit ventricular anatomy. Prog Biophys Mol Biol. 1998;69:157-83.

121. Vendelin M, Bovendeerd PHM, Arts T, Engelbrecht J, DH van Campen. Cardiac mechanoenergetics replicated by cross-bridge model. Ann Biomed Eng. 2000; 28: 629-640.

122. Vierendeels JA, Riemslagh K, Dick E, Verdonck P. Computer simulation of left ventricular filling flow: impact study on echocardiograms. Comput Cardiol. 1999(1999):177-180.

123. Vierendeels JA, Riemslagh K, Dick E. Computer simulation of intraventricular flow and pressure gradients during diastole. J Biomech Eng. 2000;122:667-674.

124. Vliegen HW, Van Straten A, De Roos A, Roest AA, Schoof PH, Zwinderman AH, Ottenkamp J, Van Der Wall EE, Hazekamp MG. Magnetic resonance imaging to assess the hemodynamic effects of pulmonary valve replacement in adults late after repair of tetralogy of fallot. Circulation. 2002;106:1703-1707.

125. Watanabe HT, Hisada S, Sugiura J, Okada, Fukunari H. Computer simulation of blood flow, left ventricular wall motion and their interrelationship by fluid-structure interaction finite element method. JSME Int J Ser C - Mech Syst Mach Elem Manufact. 2002; 45(4):1003-1012.

126. Yang C, Tang D, Haber I, Geva T, del Nido PJ. In Vivo MRI-Based 3D FSI RV/LV Models for Human Right Ventricle and Patch Design for Potential Computer-Aided Surgery Optimization. Comput Struct. 2007;85:988-997.

127. Yang C, Tang D, Geva T,Using Contracting Band to Improve Right Ventricle Ejection Fraction for Patients with Repaired Tetralogy of Fallot, a Modeling Study Using Patient-Specific CMR-Based Two-Layer Anisotropic Models of Human Right and Left Ventricles. J Thorac Cardiovasc Surg. 2013;145(1): 285-293.

128. Yang G, Toumoulin C, Coatrieux JL, Shu H, Luo L, Boulmier D. A 3D static heart model from a MSCT data set. In: 27th Annu Int Conf IEEE Eng Med Biol Soc (IEEE-EMBS 2005). Shangai, China: IEEE; 2006. p. 5499–502.

129. Yin FCP, Strumpf RK, Chew PH, Zeger SL. Quantification of the mechanical properties of noncontracting canine myocardium under simultaneous biaxial loading. J Biomech. 1987; 20:577-89.